

APPLICATION OF SPALLOGENIC NOBLE GASES  
INDUCED BY ENERGETIC PROTON IRRADIATION TO  
PROBLEMS IN GEOCHEMISTRY AND  
THERMOCHRONOMETRY

Thesis by

David Lawrence Shuster

In Partial Fulfillment of the Requirements

for the Degree of

Doctor of Philosophy



CALIFORNIA INSTITUTE OF TECHNOLOGY

Pasadena, California

2005

(Defended May 12, 2005)

© 2005

David Lawrence Shuster

All Rights Reserved

## ACKNOWLEDGEMENTS

I thank Prof. Ken Farley for the scientific opportunities, intellectual stimulation, encouragement, and friendship he provided me as my thesis advisor. I also thank Prof. Don Burnett for the countless times I dropped into his office with “quick” questions on nuclear physics and for his invaluable input to my work. I am grateful to Prof. Jess Adkins, who acted as my academic advisor and personal confidant throughout my five years at Caltech, and to Prof. John Eiler for numerous discussions and for serving on my thesis committee. I thank Prof. Tapio Schneider for his help with the inversion mathematics presented in *Chapter I*. I also benefited from insightful discussions with Prof. Jerry Wasserburg, who gave me a taste of the “old school,” grilling me with difficult questions about my work while at the white board in his office.

I am grateful for the efforts and input of my collaborators Dr. Janet Sisterson (Northeast Proton Therapy Center), Prof. Paulo Vasconcelos (University of Queensland, Brisbane), and Mr. Jonathan Heim (University of Queensland, Brisbane) whose work is presented in this dissertation. I am also grateful for the collaborative relationships I have developed with (former) fellow Caltech grad students Prof. Ben Weiss (MIT), Prof. Sujoy Mukhopadhyay (Harvard), and Prof. Sarah Stewart-Mukhopadhyay (Harvard). These three, in particular, have taught me much about doing science and set a high bar for me.

I will forever be indebted to my officemates and dear friends (future Drs.) Julie O’Leary, Juliane Fry, and John Crouse for countless discussions on all matters imaginable. It has been a remarkable experience to share workspace with such a diverse group of creative young scientists.

I am happy to give special acknowledgement to Ms. Lindsey Hedges, who worked many hours helping to prepare my samples both before and after proton

irradiations. Without her expertise and patience much of the work presented here would not have been completed (at least in a timely fashion).

I also thank Dr. Mack Kennedy (Lawrence Berkeley National Laboratory), Prof. Don DePaolo (UC Berkeley), and Prof. Martha House (Pasadena City College). Each of these people played an important role in my decision to become a Ph.D. student at Caltech. I was introduced to and learned how to do noble gas geochemistry in Mack's lab, an experience that has been invaluable to me as a grad student. I was encouraged to go to Caltech by Don, and Martha's work sufficiently inspired me to seal the deal.

I acknowledge the financial support of the Caltech Special Institute Fellowship program and the National Science Foundation Graduate Research Fellowship program, both of which provided me a little more intellectual freedom than I may have otherwise had.

Lastly, I thank my family, my mother, my sisters, and Rick and Aldeana Saber. They have always supported me emotionally and have been patient when I haven't always been available to them during these last five years. I dedicate this dissertation to my grandfather, David W. Anderson (BS '32), who initially put the Caltech bug in my head when I was a high school student and whose influence has caused a high priority to be placed on intellectual pursuit within my family. Although he did not live to read this work, I know that he would be very proud.

## ABSTRACT

Synthetic components of  $^3\text{He}$ ,  $^4\text{He}$ , and  $^{21}\text{Ne}$  were generated within natural minerals via irradiation with 150 and 220 MeV proton beams. Fluences of  $\sim 10^{14}$  and  $\sim 10^{16}$  protons/cm<sup>2</sup> induced  $^3\text{He}$  concentrations of  $\sim 10^8$  and  $\sim 10^9$  atoms/mg, respectively. Controlled degassing experiments on irradiated samples of terrestrial apatite ( $\text{Ca}_5(\text{PO}_4)_3\text{F}$ ), titanite ( $\text{Ca}(\text{TiO})(\text{SiO}_4)$ ), olivine ( $(\text{Mg,Fe})_2\text{SiO}_4$ ), goethite ( $\text{FeOOH}$ ), and quartz ( $\text{SiO}_2$ ) demonstrate that the proton-induced nuclides are spatially uniform across samples  $\leq 1$  mm in diameter and sequential degassing quantifies solid-state diffusion kinetics of helium and neon. Diffusion kinetics of proton-induced  $^3\text{He}$  in Durango apatite ( $E_a = 147.9 \pm 1.3$  kJ/mol;  $\ln(D_o/a^2) = 16.0 \pm 0.3 \ln(\text{s}^{-1})$ ) and Fish Canyon tuff titanite ( $E_a = 183.7 \pm 2.7$  kJ/mol;  $\ln(D_o/a^2) = 13.3 \pm 0.5 \ln(\text{s}^{-1})$ ), are indistinguishable from those determined for natural radiogenic  $^4\text{He}$  in the same samples. Experiments indicate that lattice damage potentially introduced via proton irradiation did not significantly modify the natural  $^4\text{He}$  diffusion kinetics in the two samples, and that the proton-induced  $^4\text{He}$  component is relatively negligible in abundance. Therefore, sequentially measured  $^4\text{He}/^3\text{He}$  ratios reflect the natural spatial distribution of radiogenic  $^4\text{He}$ . Combined with a (U-Th)/He age and helium diffusion kinetics, the distribution limits the time-temperature ( $t$ - $T$ ) path a mineral experienced through geologic time. This is the basis for a new methodology called  $^4\text{He}/^3\text{He}$  *thermochronometry*, which for apatite constrains continuous  $t$ - $T$  paths between 80 °C and 20 °C. Proton-induced  $^3\text{He}$  diffusion parameters in olivine are:  $E_a = 153.8 \pm 1.1$  kJ/mol and  $\ln(D_o/a^2) = 3.0 \pm 0.2 \ln(\text{s}^{-1})$ . At 25 °C, the helium diffusion kinetics in a goethite sample ( $E_a = 163 \pm 2.4$  kJ/mol;  $\ln(D_o/a^2) = 26.0 \pm 0.6 \ln(\text{s}^{-1})$ ) predict 90%  $^4\text{He}$  retention over 11.8 Ma, consistent with the observed deficit gas fraction and (U-Th)/He age of 10.7 Ma. This indicates that goethite (U-Th)/He dating is a viable weathering geochronometer. In quartz, the

diffusion kinetics for proton-induced  $^{21}\text{Ne}$  and  $^3\text{He}$  ( $E_a = 153.7 \pm 1.5$  (kJ/mol);  $\ln(D_0/a^2) = 15.9 \pm 0.3$  ( $\ln(\text{s}^{-1})$ ) and  $E_a = 84.5 \pm 1.2$  (kJ/mol);  $\ln(D_0/a^2) = 11.1 \pm 0.3$  ( $\ln(\text{s}^{-1})$ , respectively), indicate that cosmogenic neon will be quantitatively retained in inclusion-free quartz at Earth surface temperatures whereas cosmogenic helium will not.

## TABLE OF CONTENTS

Acknowledgements.....	iii
Abstract.....	v
Table of Contents.....	vii
List of Tables.....	x
List of Figures .....	xi
Introduction .....	1
Chapter I: $^4\text{He}/^3\text{He}$ thermochronometry .....	8
Introduction .....	10
Theory .....	13
Uniform $^3\text{He}$ distribution.....	13
Constraining an initial profile with a stepwise degassing experiment... 14	
Forward model matching and inversion.....	17
Chronometric implications of the initial profile .....	20
Methods - simulations.....	21
Results .....	25
Forward models.....	25
Isothermal profiles .....	25
Monotonic cooling.....	28
Monotonic cooling followed by 5 Myr at 25 °C.....	29
Distinct thermal histories for samples with a common He age. 31	
Inversions.....	32
Discussion .....	35
Forward model matching.....	37
Inversion accuracy and resolution.....	38
Plotting space .....	40
Correcting (U-Th)/He ages.....	44
Constraining thermal histories .....	44
Conclusion.....	46
Acknowledgements.....	46
Chapter II: Quantifying the diffusion kinetics and spatial distributions of radiogenic $^4\text{He}$ in minerals containing proton-induced $^3\text{He}$ .....	48
Introduction .....	49
Methods .....	52
Proton irradiation .....	52
Diffusion experiments .....	56

Samples .....	57
Results .....	58
Proton-induced $^3\text{He}$ production .....	58
Diffusion experiments .....	61
Discussion .....	68
$^3\text{He}$ profile uniformity.....	68
Do $^3\text{He}$ and $^4\text{He}$ diffuse at the same rate? .....	69
Effects of proton irradiation on He diffusivity.....	71
Identifying multiple diffusion domains .....	72
$^4\text{He}$ profile inversion .....	75
The spherical model.....	78
Original domain surfaces .....	80
Future directions .....	80
Conclusion.....	81
Acknowledgements.....	81
Chapter III: Weathering geochronology by (U-Th)/He dating of goethite.....	83
Introduction .....	85
Samples .....	90
Methods .....	93
He dating.....	93
Step-heating diffusion experiments.....	94
Helium dating - Results.....	97
Comparing He ages with Ar ages .....	99
Helium dating - Discussion.....	101
Stepwise degassing experiments - Results .....	106
Proton-induced $^3\text{He}$ diffusion parameters .....	108
Radiogenic $^4\text{He}$ diffusion coefficients.....	111
Ratio evolution diagrams.....	113
Helium retentivity .....	115
Stepwise degassing experiments - Discussion .....	118
Two-domain model.....	120
Quantifying deficit gas fractions .....	122
He age corrections.....	124
Internal consistency and mean temperature.....	126
Physical significance of diffusion domains .....	127
General extrapolation of goethite diffusion parameters .....	128
Conclusions .....	129
Acknowledgements.....	130
Chapter IV: Diffusion kinetics of proton-induced $^{21}\text{Ne}$ , $^3\text{He}$ and $^4\text{He}$ in quartz	131
Introduction .....	132

Sample description and methods .....	135
Results .....	137
Discussion .....	144
Diffusion kinetics of proton-induced nuclides .....	144
Proton-induced nuclides as cosmogenic analogs .....	145
Does proton irradiation affect noble gas diffusion kinetics in quartz? .....	148
Diffusion results in context of previous studies .....	153
Implications for cosmogenic nuclide retentivity .....	157
Physical implications .....	160
Conclusion .....	163
Acknowledgements .....	164
Bibliography .....	165

## LIST OF TABLES

## Chapter II:

<i>Number</i>	<i>Page</i>
1. Dose/yield summary .....	60
2. Diffusion coefficient summary.....	64

## Chapter III:

<i>Number</i>	
1. Replicate goethite He ages .....	98
2. Comparison between He and Ar ages, stratigraphic relationships .....	101
3. Stepwise degassing results .....	107
4. Two-domain model diffusion parameters.....	122

## Chapter IV:

<i>Number</i>	
1. Dose/yield summary for quartz.....	138
2. Stepped heating results (Experiment 1).....	140
3. Stepped heating results (Experiment 2, lower proton dose) .....	150
4. Diffusion coefficient summary (Experiment 1).....	154

## LIST OF FIGURES

## Chapter I:

<i>Number</i>	<i>Page</i>
1. Step-heating simulation of isothermally evolved profiles.....	26
2. Step-heating simulations of profiles resulting from monotonic cooling..	30
3. Simulations of profiles obtained from distinct thermal histories yielding an apatite (U-Th)/He age of 10 Ma .....	33
4. Effects of a 1% error in measured He data on the profile obtained using the inversion method.....	36
5. Limits for the spatially uniform $^4\text{He}$ production-diffusion model .....	42

## Chapter II:

<i>Number</i>	<i>Page</i>
1. Schematic showing the irradiation setup .....	53
2. Arrhenius plots for (a) Durango apatite, (b) FCT titanite, and (c) Guadalupe olivine.....	62
3. Durango apatite ratio evolution diagram.....	65
4. Radial concentration profiles .....	74

## Chapter III:

<i>Number</i>	<i>Page</i>
1. Microscopy.....	92
2. $^3\text{He}$ Arrhenius plots for (a) BAH-F124-114 and (b) BAH-F124-111.2..	109
3. $^4\text{He}$ Arrhenius plots for (a) BAH-F124-114 and (b) BAH-F124-111.2..	112
4. Goethite $^4\text{He}/^3\text{He}$ vs. $\Sigma F^3\text{He}$ ratio evolution diagrams for (a) BAH-F124-114 and (b) BAH-F124-111.2.....	114

5. $^4\text{He}$ retention curves.....	116
--	-----

Chapter IV:

*Number*

1. Arrhenius plot for proton-induced nuclides (Experiment 1) .....	141
2. Ratio evolution diagram (Experiment 1) .....	143
3. Arrhenius plot for proton-induced nuclides (Experiment 2, lower proton dose) .....	151
4. Neon retentivity in quartz .....	159

## *Introduction*

A wealth of information about low-temperature and near-surface planetary processes can be derived from measured abundances and spatial distributions of radiogenic and cosmogenic noble gas nuclides in terrestrial and extraterrestrial materials. Due to their relatively simple physical behavior, observations of naturally occurring noble gases can constrain timescales, rates, and temperatures associated with orogenic processes, chemical weathering, cosmogenic exposure, as well as many other naturally occurring phenomena [1]. This information can then be related to the greater planetary physical environment in search of causality and pattern. However, pursuing this end requires developing a detailed understanding of the fundamental physics that relates geological or planetary conditions to the chemical observations that can be made on a natural material today.

Time and temperature are two of the most fundamental variables in problems of Earth and planetary sciences. The ability to quantify thermal variations recorded in the geological record has been critical for evaluating natural processes that involve heat flow perturbations. *Thermochronometry* is a family of methodologies that utilize chemical observations made of a natural material today to constraint that material's *thermal* history through geologic *time*. The most successful of these methodologies involve the thermally activated diffusion of a radiogenic nuclide.

Thermochronometry often involves the determination of a cooling age from parent and daughter abundances within an entire crystal or population of crystals [2]. However, complementary information exists in the spatial concentration distribution of the daughter,  $C(x,y,z)$ , within a single crystal. By combining a bulk cooling age with  $C(x,y,z)$  on the same sample, it is possible to place tight limits on the sample's continuous time-temperature ( $t$ - $T$ ) path through geologic time.

During the last four decades, techniques for this kind of analysis have been developed for several different parent/daughter systems including U-Th-Pb and K-Ar [3]. In the first two chapters of this dissertation, I describe how this approach is applied to the (U-Th)/He system, by introducing a synthetic component of  $^3\text{He}$  via proton irradiation. The particular attraction of the (U-Th)/He method is its sensitivity to uniquely low temperatures. For example, the nominal  $^4\text{He}$  closure temperatures (at  $10^\circ\text{C}/\text{Myr}$ ) for apatite, zircon, and titanite are  $70^\circ\text{C}$ ,  $180^\circ\text{C}$ , and  $200^\circ\text{C}$ , respectively [4-8]. In the case of apatite, I show that significant diffusive mobility of  $^4\text{He}$  occurs at temperatures just slightly higher than those of Earth's surface.

In *Chapter I*, I develop the theoretical framework for  $^4\text{He}/^3\text{He}$  thermochronometry in which the natural spatial distribution of  $^4\text{He}$  is constrained by stepwise degassing  $^4\text{He}/^3\text{He}$  analysis of a sample containing synthetic, proton-induced  $^3\text{He}$ . In *Chapter II*, I present practical aspects of proton irradiation and stepwise  $^4\text{He}/^3\text{He}$  analyses in addition to experiments that evaluate several of the

assumptions presented in *Chapter I*. In particular, these two chapters illustrate how the  $^4\text{He}/^3\text{He}$  technique can be used to determine the helium diffusion kinetics *and* constrain the natural  $^4\text{He}$  distribution within an individual crystal or a small population of crystals, and how this information can be used to constrain the sample's  $t$ - $T$  path. I also discuss some of the complications that have arisen and summarize the current state of research on this new thermochronometer.

In *Chapter III*, I describe how this same approach can be applied toward a different objective. Chemical weathering products, such as supergene Fe-oxides, precipitate at relatively low temperatures and in most cases reside at nearly constant temperatures; they are expected, *a priori*, to have experienced isothermal histories. The spatial distribution of  $^4\text{He}$  within these minerals therefore quantifies the amount of diffusive  $^4\text{He}$  loss experienced by the sample and permits a correction to be applied to the sample's absolute (U-Th)/He age. The corrected age represents the time since the weathering product precipitated and places the environmental conditions required for the weathering reaction(s) within a temporal context. For instance, the recent discovery of goethite ( $\text{FeOOH}$ ) in Gusev crater on Mars by the Spirit rover has been interpreted to prove the existence of liquid water at the surface of Mars [9], apparently requiring temperatures  $> 0^\circ\text{C}$  whenever these minerals precipitated. Similar arguments can be made about goethite preserved in weathering profiles on Earth [10]. However, the timing of the presence of liquid water in these cases can only be constrained if the goethite precipitation age is determinable.

I show that the spatial distribution of  $^4\text{He}$  can be constrained within terrestrial polycrystalline supergene goethite ( $\text{FeOOH}$ ) using the proton irradiation and stepwise  $^4\text{He}/^3\text{He}$  analysis described in *Chapter II*. In conjunction with a conventional (U-Th)/He age, I show how this information can be used to constrain the accurate precipitation age of supergene goethite by correcting for partial  $^4\text{He}$  retention.

In *Chapter IV*, I demonstrate that proton irradiation can be used to introduce synthetic  $^3\text{He}$ ,  $^4\text{He}$ , and  $^{21}\text{Ne}$  into quartz. This chapter illustrates how the proton irradiation technique can be used for basic geochemical and material properties investigations. Since the three proton-induced nuclides are good analogs for naturally occurring cosmogenic nuclides, their diffusion kinetics have implications for the interpretation of cosmogenic nuclide observations in terrestrial and extraterrestrial samples. I present two experiments that simultaneously quantify the diffusion kinetics of all three nuclides and investigate the influence that radiation damage may have upon the kinetics.

### **Fundamental considerations**

The basic principles and assumptions of (U-Th)/He dating have been described in detail elsewhere [11]. In the first three chapters, I concentrate only on aspects particular to the  $^4\text{He}/^3\text{He}$  variant of the method. Like other radio-thermochronometry, (U-Th)/He dating involves two physical processes: radiogenic ingrowth of a daughter product ( $^4\text{He}$ ) and thermally activated volume

diffusion of the daughter. However, a difference between the (U-Th)/He system and other chronometers is that multiple parent nuclides produce a common daughter through  $\alpha$  decay. Although  $\alpha$  decay of  $^{147}\text{Sm}$  also produces  $^4\text{He}$ , the vast majority of radiogenic  $^4\text{He}$  in minerals is produced via actinide decay. Once in a state of secular equilibrium, the actinide decay series emit 8, 7, and 6  $\alpha$ -particles for a single decay of  $^{238}\text{U}$ ,  $^{235}\text{U}$ , and  $^{232}\text{Th}$ , respectively. The  $^4\text{He}$  ingrowth equation can therefore be written:

$$^4\text{He} = 8 \cdot ^{238}\text{U} \cdot (e^{\lambda_{238}t} - 1) + 7 \cdot \left( \frac{^{238}\text{U}}{137.88} \right) \cdot (e^{\lambda_{235}t} - 1) + 6 \cdot ^{232}\text{Th} \cdot (e^{\lambda_{232}t} - 1),$$

where  $^4\text{He}$ ,  $^{238}\text{U}$ , and  $^{232}\text{Th}$  indicate present-day abundances,  $t$  is the accumulation time or He age,  $\lambda$  is a radioactive decay constant ( $\lambda_{238} = 1.511 \times 10^{-10} \text{ yr}^{-1}$ ,  $\lambda_{235} = 9.849 \times 10^{-10} \text{ yr}^{-1}$ ,  $\lambda_{232} = 4.948 \times 10^{-11} \text{ yr}^{-1}$ ), and  $(1/137.88)$  is the present day  $^{235}\text{U}/^{238}\text{U}$  ratio.

### The $^4\text{He}$ spatial distribution

The basis for  $^4\text{He}/^3\text{He}$  thermochronometry is that the spatial distribution of radiogenic  $^4\text{He}$  within a U and Th bearing crystal is an evolving function of the sample's  $t$ - $T$  path. This can be summarized by the following schematic equation, which applies to an individual crystal:

$$\int_{t_0}^{\text{today}} [\text{Production}(x, y, z, t) - \text{Removal}(x, y, z, T, t)] dt = \text{Distribution}(x, y, z, \text{today}),$$

where *Production* is the time-dependent radiogenic production function of  ${}^4\text{He}$ , *Removal* is the time- and temperature-dependent diffusive loss function, *Distribution* is the spatial concentration function of  ${}^4\text{He}$  within the sample today, and  $t_0$  is the time when  ${}^4\text{He}$  accumulation initiates. With knowledge of these functions, the above expression provides a relationship between measurable quantities and the desired  $t$ - $T$  path of the sample. Since the physics that describes and relates these functions is well-established, the challenge is to quantify the functional form of each.  ${}^4\text{He}/{}^3\text{He}$  thermochronometry provides an analytical technique to constrain (i) the *Distribution* function in a sample today and (ii) the *Removal* function (i.e., via the helium diffusion kinetics). For a sample with uniformly distributed parent nuclides, the standard assumptions of (U-Th)/He dating provides (iii) the *Production* function through knowledge of the bulk U and Th concentrations in the sample today. Although nonuniform parent distributions could easily be incorporated into the theory, for simplicity I initially consider only the uniform case.

Classical diffusion theory provides the necessary relationships between time, temperature, and the spatial distribution of a radiogenic noble gas within a solid matrix [12, 13]. Using numerical methods, the classical theory can be

extended to any arbitrary geometry. However, specific analytic solutions to the production-diffusion equation exist. The spherical solution is the most useful, and one that provides the clearest way to illustrate and conceptualize the relationship between  $t$ ,  $T$ , and  $C(x,y,z)$  within a crystal. Throughout this dissertation, I focus on the spherical solution, and discuss below why the spherical model is useful for many geological applications.

*Chapter 1* $^4\text{He}/^3\text{He}$  THERMOCHRONOMETRY

D. L. Shuster

K. A. Farley

(This chapter was reprinted from *Earth and Planetary Science Letters* (2004), 217, 1-17)

**Abstract** - Using classical diffusion theory, we present a mathematical technique for the determination of  $^4\text{He}$  concentration profiles in minerals. This approach should prove useful for constraining the low-temperature cooling histories of individual samples and for correcting (U-Th)/He ages for partial diffusive loss. The calculation assumes that the mineral of interest contains an artificially produced and uniform distribution of  $^3\text{He}$  obtained by proton irradiation [14]. In minerals devoid of natural helium, this isotope allows measurement of He diffusion coefficients; in minerals with measurable radiogenic He, it permits determination of  $^4\text{He}$  profiles arising during ingrowth and diffusion in nature. The  $^4\text{He}$  profile can be extracted from stepwise degassing experiments in which the  $^4\text{He}/^3\text{He}$  ratio is measured. The evolution of the  $^4\text{He}/^3\text{He}$  ratio as a function

of cumulative  $^3\text{He}$  released can be compared with forward models to constrain the shape of the profile. Alternatively, we present a linear inversion that can be used to directly solve for the unknown  $^4\text{He}$  distribution. The inversion incorporates a standard regularization technique to filter the influence of random measurement errors on the solution. Using either approach we show that stepwise degassing data can yield robust and high-resolution information on the  $^4\text{He}$  profile.

Profiles of radiogenic He are a sensitive function of the time-temperature ( $t$ - $T$ ) path that a cooling sample experienced. Thus, by step-heating a proton-irradiated sample it is possible to restrict the sample's acceptable  $t$ - $T$  paths. The sensitivity of this approach was explored by forward-modeling  $^4\text{He}$  profiles resulting from a range of realistic time-temperature paths, using apatite as an example. Results indicate that  $^4\text{He}$  profiles provide rich information on  $t$ - $T$  paths, especially when the profiles are coupled with (U-Th)/He cooling ages on the same sample.

Samples that experienced only moderate diffusive loss have  $^4\text{He}$  concentration profiles that are rounded at the edge but uniform in the core of the diffusion domain. Such profiles can be identified by nearly invariant  $^4\text{He}/^3\text{He}$  ratios after the first few to few-tens of percent of  $^3\text{He}$  have been extracted by step heating. We show how such data can be used to correct (U-Th)/He ages for partial diffusive loss.

## 1. Introduction

Helium isotopes are used extensively as chronometers in terrestrial and extraterrestrial materials.  $^4\text{He}$  produced from radioactive decay of U and Th series nuclides and  $^{147}\text{Sm}$  forms the basis of (U-Th)/He chronometry, e.g., [11, 15-17], while  $^3\text{He}$  produced by cosmic ray spallation is used to estimate surface exposure ages and erosion rates [18, 19]. The main attraction of He for these applications is that its production rates are high compared to other isotope systems, coupled with the fact that high precision, high sensitivity He analyses are comparatively easy. A critical consideration for these uses is that He diffusion in most minerals occurs at moderate temperatures (250 °C to 20 °C) [11]; failure to consider diffusive loss can lead to erroneously young He-based age constraints. Indeed, this is the primary reason that (U-Th)/He and terrestrial cosmogenic  $^3\text{He}$  dating have seen only limited application over the last several decades [20] despite considerable analytical advancement [11]. However, if properly characterized, diffusive loss can be used to study low-temperature geologic processes through (U-Th)/He thermochronometry.

Knowledge of He diffusion kinetics is therefore critical for materials in which He measurements are made, particularly for chronometry. Although other methods are sometimes used [21, 22], stepwise vacuum outgassing is the most common technique for determining the apparent He diffusivity,  $D/a^2$  ( $D$  is the diffusion coefficient,  $a$  is the characteristic length scale of the diffusion domain). By measuring the temperature dependence of diffusivity, it is possible to

determine the two parameters (activation energy,  $E_a$  and frequency factor,  $D_0/a^2$ ) that define the Arrhenius function  $D(T)/a^2 = D_0/a^2 \exp(-E_a/RT)$  required to extrapolate He diffusion coefficients to low temperatures and long timescales over which direct laboratory measurements are impossible.

Vacuum diffusion experiments have several limitations. First, they require sufficient  $^4\text{He}$  or  $^3\text{He}$  ( $\geq 10^{10}$  and  $\geq 10^6$  atoms, respectively) for accurate detection, and so are presently limited either to U-rich phases, old samples, samples that experienced appreciable surface exposure [23], or samples in which He has been introduced by sorption [22]. Current detection limits usually require either large or multiple grains to be analyzed simultaneously, whereas for many applications single-crystal experiments are preferable. A more subtle problem is caused by the initial He distribution within a sample. The rate of diffusive He loss depends on both the diffusivity and the concentration gradient, so converting stepwise release data to diffusivity requires specification of the concentration distribution,  $C_0(x,y,z)$ , where  $x$ ,  $y$ , and  $z$  are spatial coordinates [24]. An initially uniform concentration across a spherical diffusion domain,  $C_0(r) = \text{constant}$ , is typically assumed, where  $r$  is the radius. This assumption is violated for samples that have experienced He loss either by diffusion or by ejection of alpha particles from mineral surfaces following decay. Failure to incorporate such profile rounding in the computation will yield diffusivities that underestimate the true values, potentially by many orders of magnitude. In some cases, an

unrecognized rounded profile can yield a remarkably linear Arrhenius array that implies incorrect  $E_a$  and  $D_0/a^2$ , particularly in the earliest steps.

The goal of previous He diffusion experiments has been to verify He retention in a given material under given conditions (e.g., is cosmogenic  $^3\text{He}$  quantitatively retained in quartz at 20 °C? [23]), or to determine the temperature dependence of diffusivity ( $D(T)/a^2$ ) for thermochronological interpretation [4, 5]. As demonstrated by  $^{40}\text{Ar}/^{39}\text{Ar}$  dating [25], the spatial distribution of a uniformly produced radiogenic noble gas reflects a sample's thermal history. If known, the distribution (i) permits correction of ages for diffusive loss (i.e., identification of a  $^{40}\text{Ar}/^{39}\text{Ar}$  age plateau) and (ii) with knowledge of  $D(T)$  and the parent nuclide distribution, constrains the thermal history (geologic  $t$ - $T$  path) of a sample. Quantitative use of the (U-Th)/He system for these purposes should also be possible. If we determine the *shape* of a  $^4\text{He}$  concentration profile, the function  $D(T)/a^2$  and the U and Th distribution within a sample, we can constrain its  $t$ - $T$  path. If we determine the *quantity* of “missing” He, we can in some cases correct a He age for diffusive  $^4\text{He}$  loss and/or  $\alpha$ -ejection.

Direct measurement of a He distribution is not usually possible. Nuclear reaction analysis and secondary ionization and laser microprobe mass spectrometry lack sufficient sensitivity and/or spatial resolution to measure He concentrations at levels found in most minerals. While ultraviolet laser extraction can be used to measure  $^{40}\text{Ar}/^{39}\text{Ar}$  profiles [26], high He diffusivities in most minerals make He susceptible to even a small thermal aureole around the ablation

pit. Currently the only way to assess the shape of a He concentration profile  $C_o(r)$  is to use the indirect approach of stepwise degassing. To determine  $C_o(r)$  from stepwise release fractions requires either independent knowledge of  $D(T)/a^2$  or a second, uniformly distributed isotope from which  $D(T)/a^2$  can be determined [27].

Here we describe how a laboratory-induced, uniform  $^3\text{He}$  distribution coupled with an isotope ratio step-heating experiment can be used to determine He diffusivities in *any* mineral and to constrain an unknown natural  $^4\text{He}$  distribution using either forward or inverse models. We also examine how thermal histories are recorded in a concentration profile using apatite as an example. In a companion paper we demonstrate applications of this approach following uniform production of  $^3\text{He}$  (and negligible  $^4\text{He}$ ) from all major target elements in minerals via bombardment with a 150 MeV proton beam [14].

## 2. Theory

### 2.1 Uniform $^3\text{He}$ distribution

A uniform  $^3\text{He}$  distribution is useful because (i) it satisfies the initial condition from which diffusion coefficients are easily calculated [24]; (ii) it allows determination of He diffusivities in minerals that do not contain sufficient natural He for accurate measurement [14], and (iii) it permits a step-heating experiment in which the  $^4\text{He}$  release is normalized to the  $^3\text{He}$  released in the same step. Such a *ratio evolution experiment* constrains the initial  $^4\text{He}$  distribution.

Unlike  $^{39}\text{Ar}$  in the  $^{40}\text{Ar}/^{39}\text{Ar}$  method, laboratory-induced  $^3\text{He}$  is not uniquely produced from the parent isotopes of  $^4\text{He}$  [14], so He isotope release data do not define a radiometric age for each step. Instead, such data constrain only the  $^4\text{He}$  distribution. With independent knowledge of parent distributions the  $^4\text{He}$  profile can be used to correct a He age for diffusive loss, or place  $t$ - $T$  constraints on the sample. Because He has only two isotopes, a “trapped” He component cannot be identified as it sometimes can in the Ar system [25]. Therefore, this approach is most effectively applied to samples free of excess He in the matrix or inclusions.

## 2.2 Constraining an initial profile with a stepwise degassing experiment

For reasons discussed below and in [14], it is usually sufficient and simpler to represent a natural  $^4\text{He}$  distribution,  $C_o(x,y,z)$ , by a model radial distribution,  $C_o(r)$ , within a spherical diffusion domain of equivalent surface area to volume ratio. For a diffusing substance having an initial radial concentration  $C_o(r)$  within a spherical diffusion domain ( $0 < r < a$ ), the concentration at a later time is

$$C(r, \tau) = \frac{2}{ar} \sum_{k=1}^{\infty} e^{-k^2\pi^2\tau} \sin\left(\frac{k\pi r}{a}\right) \int_0^a r' C_o(r') \sin\left(\frac{k\pi r'}{a}\right) dr', \quad (1)$$

[12] if its mobility follows thermally activated volume diffusion and  $C_o(a) = 0$  for all  $t$ . We use the non-dimensional diffusion time

$$\tau(T, t) = \int_0^t \frac{D(T, t')}{a^2} \cdot dt'. \quad (2)$$

Given knowledge of  $D(T, t)/a^2$ , equation (1) describes the distribution  $C_i(r)$  after each step  $i = \{1, \dots, n\}$  of a stepwise degassing experiment (either simulated or actual). Considering  $\tau_i$  to be a piecewise linear, cumulative quantity over the course of an experiment

$$\tau_i = \sum_i \tau(T_i, t_i), \quad (3)$$

the radial distribution after each step of duration  $t_i$  is given by

$$C_i(r) = C(r, \tau_i). \quad (4)$$

By integrating over the spherical domain, the total amount of diffusant (e.g.,  $^4\text{He}$ ) within the domain after each step  $i$  is given by

$$N_i = \int_0^a 4\pi r^2 C_i(r) dr. \quad (5)$$

After each step, the remaining fraction ( $f$ ) of the original amount of gas is defined as

$$f_i = \frac{N_o - N_i}{N_o}, \quad (6)$$

where  $N_o$  is the original amount. Using the non-dimensional spatial coordinate  $x \equiv r/a$ , the remaining fraction can also be approximated for value of  $\tau < 0.05$  by

$$f(\tau) = \int_0^1 K(x, \tau) b(x) dx + \varepsilon, \quad (7)$$

where, after Albarède [28],

$$K(x, \tau) = 3x - 3 \left( \operatorname{erf} \frac{1+x}{2\sqrt{\tau}} - \operatorname{erf} \frac{1-x}{2\sqrt{\tau}} \right), \quad (8)$$

and

$$b(x) = xC_o(x)$$

and  $\varepsilon$  is the analytical error. Taking equation (7) as piecewise continuous in  $\tau$  such that  $f_i = f(\tau_i)$ , there exists a direct relation between the sought-after initial profile  $C_o(x)$  and the sets of  $\tau_i$  and  $f_i$  in the degassing experiment.

### 2.2.1 Forward model matching and inversion

If  $D(T)/a^2$  is known, these relationships allow us to calculate a set of simulated He remaining fractions,  $f_i$ , for any arbitrary initial profile,  $C_o(r)$ , and heating schedule,  $\tau_i$ . If the two He isotopes have known relative diffusivity (see below), equation (6) can be used to calculate isotope ratios for the concurrent release of a uniformly distributed isotope ( $^3\text{He}$ ) and an isotope with an arbitrary natural distribution ( $^4\text{He}$ ). This simulates a ratio evolution experiment.

By matching a simulated ratio evolution to experimental observations, forward calculations can be used to constrain  $C_o(x)$ . In the remaining text, we will refer to this approach as *forward model matching*. In the absence of a uniform  $^3\text{He}$  distribution, forward model matching to the set of  $f_i$  can be used to constrain the shape of a  $^4\text{He}$  profile, although independent knowledge of  $D(T)/a^2$  is required.

As shown by Albarède (1978), the above relationships also permit us to directly invert a set of  $f_i$  and an independently determined set of  $\tau_i$  to solve for  $C_o(x)$ . With a uniform  $^3\text{He}$  distribution, and if  $^3\text{He}$  and  $^4\text{He}$  have identical diffusivities (or diffusivities that can be quantitatively related to each other), the set of  $\tau_i$  can be calculated from the  $^3\text{He}$  release fractions of a step-heating experiment according to [24] and equation (3). The set of  $f_i$  given by the concurrently determined  $^4\text{He}$  release fractions can then be used to invert equation (7) for  $C_o(x)$  as follows.

Equation (7) is a Fredholm integral equation of the first kind; obtaining the solution  $b(x)$  from (7) is an ill-posed problem [29]. The integral expression can be made arbitrarily discrete in  $x$ , thereby defining an  $n \times m$  design matrix  $\mathbf{K}$  and a  $m \times 1$  concentration vector  $\mathbf{b}$  ( $\mathbf{b} = x_j C_{o_j}$ ), where  $i = \{1, \dots, n\}$ ,  $j = \{1, \dots, m\}$  and typically,  $n < m$ . In matrix notation, equation (7) can be expressed as

$$\mathbf{f} = \mathbf{K}\mathbf{b} + \boldsymbol{\varepsilon}, \quad (9)$$

where  $\mathbf{f}$  is a column vector of  $f_i$ . The model vector  $\mathbf{b}$  is a solution of a linear system of equations. The inversion is a discrete ill-posed problem, and may require regularization. Using singular value decomposition to replace  $\mathbf{K}$  by  $\mathbf{U}\boldsymbol{\Sigma}\mathbf{V}^T$  [29], the minimum-norm solution  $\mathbf{b}$  (or  $\hat{\mathbf{b}}$ ) of the least squares problem can be calculated by

$$\hat{\mathbf{b}} = \sum_{i=1}^r \frac{u_i^T \mathbf{f}}{\sigma_i} v_i, \quad (10)$$

where for  $n < m$ ,  $\mathbf{U} = (u_1, \dots, u_n) \in \mathfrak{R}^{n \times n}$ ,  $\mathbf{V} = (v_1, \dots, v_m) \in \mathfrak{R}^{m \times m}$ , and the first  $r$  diagonal elements ( $i=j$ ) of the matrix  $\boldsymbol{\Sigma} \in \mathfrak{R}^{n \times m}$  are the non-zero singular values ( $\sigma_i$ ) of  $\mathbf{K}$  such that  $\sigma_1 \geq \sigma_2 \geq \dots \geq 0$ , and  $r \leq n$ . Note that the columns  $j > n$  of  $\mathbf{V}$  and  $\boldsymbol{\Sigma}$  will be padded with zeros and will not contribute to the estimate  $\hat{\mathbf{b}}$ .

When working with laboratory data the values  $f_i$  will contain analytical errors ( $\varepsilon_i$ ) that limit the information about  $\mathbf{b}$  that is invertible from equation (9). A threshold index,  $i_h$ , can usually be identified as a break in slope if the coefficients  $\log(|u_i^T \mathbf{f}|)$  are plotted vs. index  $i$ , where for  $i > i_h$  the coefficients  $|u_i^T \mathbf{f}|$  will be dominated by  $|u_i^T \boldsymbol{\varepsilon}|$ . These components will dominate  $\hat{\mathbf{b}}$ , leading to a minimum-norm solution with very large variance [29] and rendering the inversion useless. To avoid this situation, an additional constraint of smoothness can be used; although this contributes bias to  $\hat{\mathbf{b}}$ , it will greatly improve the stability of the solution.

In this paper, we use a practical regularization technique called the ridge regression [30, 31] (or Tikhonov regularization). The ridge regression uses the filter

$$w_i = \frac{\sigma_i^2}{\sigma_i^2 + h^2}, \quad (11)$$

where the value of  $h$  (roughly corresponding to the value of  $\sigma_i$  for  $i = i_h$ ) defines the threshold below which singular values will then insignificantly contribute to the estimate  $\hat{\mathbf{b}}$ . Under most experimental conditions, the value of  $h$  will be determined by analytical uncertainty in  $f_i$ . Given the set of  $w_i$ , the ridge regression estimate is regularized by

$$\hat{\mathbf{b}} = \sum_{i=1}^n w_i \frac{u_i^T \mathbf{f}}{\sigma_i} v_i. \quad (12)$$

Therefore, within analytical uncertainty a stable solution  $\hat{\mathbf{b}}$  can be calculated from a combined  $^3\text{He}$  and  $^4\text{He}$  diffusion experiment. The  $^3\text{He}$  results yield  $D(T)/d^2$  (i.e., define the set of  $\tau_i$ ) and the measured  $f_i$  are determined from  $^4\text{He}$  release. The profile  $C_o(x)$  can then be calculated from  $\hat{\mathbf{b}}$ . A consequence of regularization is degradation of the resolution kernels, which ultimately limits the amount of information that can be retrieved by the inverse calculation [29].

### 2.3 Chronometric implications of the initial profile

We now consider two potential uses of a natural  $^4\text{He}$  profile revealed by the techniques described above: (i) to quantify and correct for the fraction of He removed by diffusion and  $\alpha$ -ejection, and (ii) to constrain sample  $t$ - $T$  paths. Our goal is to evaluate the sensitivity of the  $^4\text{He}$  profile for each of these applications.

It is useful to compare the total amount of diffusant in a rounded profile ( $N_o$ , equation (5)) with the amount in a uniform profile ( $N_{uniform}$ ) with concentration equivalent to that of a quantitatively retentive material. We define the *deficit gas fraction* as  $(N_{uniform} - N_o)/N_{uniform}$ . In certain instances, this quantity can be used to correct an absolute He age for diffusive and  $\alpha$ -ejection loss. An important caveat to this correction is that diffusion and  $\alpha$ -ejection have not

removed helium from the center of the domain, when  $N_{uniform} = 4/3\pi a^3 C_o(r = 0)$ . This case will generally be met for deficit gas fractions  $< 50\%$  and might apply, e.g., to volcanic phenocrysts and low-temperature precipitates that partially retain He under Earth surface conditions.

With knowledge of  $D(T)/a^2$  for a sample, model  $^4\text{He}$  profiles can be calculated according to radiogenic ingrowth, diffusion, and  $\alpha$ -ejection on specific  $t$ - $T$  paths. A finite set of  $t$ - $T$  paths will be consistent with the sample's  $^4\text{He}$  distribution and He age. Running Monte Carlo simulations or using the constrained random search method [32] can identify a family of  $t$ - $T$  solutions that are consistent with the  $^4\text{He}$  profile. This approach is similar to that used with single-sample  $^{40}\text{Ar}/^{39}\text{Ar}$  thermochronometry [33, 34] and fission track length modeling [35].

### 3. Methods - Simulations

To demonstrate the capabilities and limitations of this method, we simulated several step-heating experiments using equation (6). This complements a companion paper in which we apply the method to natural minerals [14]. For each step, we calculated remaining gas fractions  $f_i$  expected for various input concentration profiles  $C_o(x)$  obtained from specified  $t$ - $T$  paths. We explored the method's sensitivity to both the *shape* of an input concentration profile and also to the deficit gas fraction.

We used two approaches. The first was to input a known diffusivity function  $D(T)/a^2$  and an arbitrary concentration profile  $C_o(x)$ , with which we calculated remaining fractions for each step of a simulated heating schedule. Using the set  $f_b$  we simulated the fraction of gas released at each step:

$$F_i = f_{i-1} - f_i, \text{ where } f_o \equiv 1. \quad (13)$$

Using step-release fractions,  $F_b$ , we calculated a set of  $\ln(D/a^2)_{\text{calculated}}$  values using [24] by *inappropriately* assuming an initially uniform concentration profile. We plotted these values against cumulative He release fraction ( $\Sigma F$ ) to graphically represent characteristic  $\ln(D/a^2)_{\text{calculated}}$  patterns.

The second approach was to simulate a ratio evolution experiment. We assumed a function  $D(T)/a^2$  and two concentration profiles; one uniform (i.e.,  $^3\text{He}$ ), the other arbitrarily round (i.e.,  $^4\text{He}$ ). We calculated isotope ratios for each step from the release fractions (i.e.,  $F_i^{4\text{He}} / F_i^{3\text{He}} = R_{\text{step}}$ ) and then normalized these ratios to the bulk ratio,  $R_{\text{bulk}}$ , calculated by integrating the initial profiles. The output is a plot of normalized  $^4\text{He}/^3\text{He}$  vs. cumulative  $^3\text{He}$  release fraction ( $\Sigma F^3\text{He}$ ), or a *ratio evolution diagram*.

In both approaches, the release patterns ( $\ln(D/a^2)_{\text{calculated}}$  vs.  $\Sigma F_i$  and  $R_{\text{step}}/R_{\text{bulk}}$  vs.  $\Sigma F^3\text{He}$ ) reflect the input concentration profiles. The sensitivity that

these output patterns have to the exact *shape* of the input profiles determines our ability to constrain actual concentration profiles by forward model matching.

In all calculations, we assumed  $^3\text{He}$  and  $^4\text{He}$  diffusivities to be identical. Some authors have suggested that the diffusion of a noble gas through a mineral may be governed by the kinetic theory of non-uniform gases resulting in mass-dependent diffusivities, (e.g.,  $D_4/D_3 = \sqrt{m_3/m_4} = 0.868$ ; [36, 37]). While an effect of this magnitude has never been observed in minerals, other mass-dependent relationships may exist [38-40]. Because the thermally activated mobilization of a radiogenic noble gas through a solid is significantly different than most diffusive processes, it is not clear what mass dependence, if any, should relate diffusivities of the He isotopes. In a companion paper [14] we show that in apatite and titanite, diffusivities of spallation  $^3\text{He}$  and radiogenic  $^4\text{He}$  are equivalent within error, justifying our assumption. Nevertheless the above methods can easily be adjusted to accommodate a bias between  $^3\text{He}$  and  $^4\text{He}$  diffusivities if one is demonstrated for a given mineral.

Ejection of  $\alpha$  particles from the outer  $\sim 20$  microns of a mineral causes a predictable shape to the radiogenic He profile independent of diffusion [41]. We initially ignored this effect, and then included it by assuming that the grain itself is the diffusion domain. Using a modified code of [42] we calculated  $^4\text{He}$  profiles by ingrowing radiogenic  $^4\text{He}$  along a prescribed  $t$ - $T$  path for a given diffusivity parameter set, with or without alpha ejection. We simulated relatively simple but

distinct  $t$ - $T$  paths to assess how the resulting  $^4\text{He}$  profiles and release patterns differ.

In the ingrowth calculations, we assumed a uniform parent distribution across the diffusion domain and a zero concentration boundary for all time  $t$ . For illustration, we used the best-fit diffusion parameters of Durango apatite for all simulations [4]. However, the ability to reconstruct concentration profiles is insensitive to the exact diffusion parameters used. For all calculations, we assumed spherical geometry and thermally activated volume diffusion from a single domain. Diffusion experiments have shown that individual grains of apatite, titanite, and zircon can be well-represented as single diffusion domains [4, 5, 43]. These simulations assume no measurement error.

While we have modeled He diffusion from minerals assuming spherical geometry, in reality the diffusion domain is unlikely to be a sphere. An important question is whether we can accurately capture diffusion behavior and resulting concentration profiles from a more realistic geometry (e.g., a cylinder [4, 44]) using our model. In [14] we show that provided the diffusivities (from  $^3\text{He}$ ), the  $^4\text{He}$  release fractions, and the thermal ( $t$ - $T$ ) modeling are determined on the same sample with the same geometric assumption, the problem can be accurately represented by the spherical model without knowledge of  $a$ . Using stepwise release data for a uniformly distributed gas ( $^3\text{He}$ ), the formulation of [24] produces diffusivities corresponding to a model spherical domain (of radius  $a$ ) with a surface area to volume ratio approximating that of the actual domain.

Regardless of geometry we must also assume that diffusivity is crystallographically isotropic, which appears to be the case at least for apatite [4].

## 4. Results

### 4.1 Forward models

In this section, we show that specific  $t$ - $T$  paths result in specific  ${}^4\text{He}$  concentration profiles. The absolute He concentration depends on the U and Th concentrations, but the *shape* of the  ${}^4\text{He}$  profile depends only on thermal history and  $\alpha$ -ejection. When run through simulated stepwise degassing experiments, the profiles yield distinct  ${}^4\text{He}$  release patterns (Figs. 1-3). We present the results in order of increasing concentration profile complexity, i.e., in order of increasing radial structure.

#### 4.1.1 Isothermal profiles

In Fig. 1, we present stepwise degassing simulations for six concentration profiles calculated according to ingrowth and diffusion under isothermal conditions, but excluding the effect of  $\alpha$ -ejection. These represent relatively simple profiles expected in nature (e.g., for a surface-exposed sample, a low-temperature precipitate such as a weathering product [45] or biogenic fossil [46], or certain meteoritic samples [47, 48]). These profiles might represent  ${}^4\text{He}$

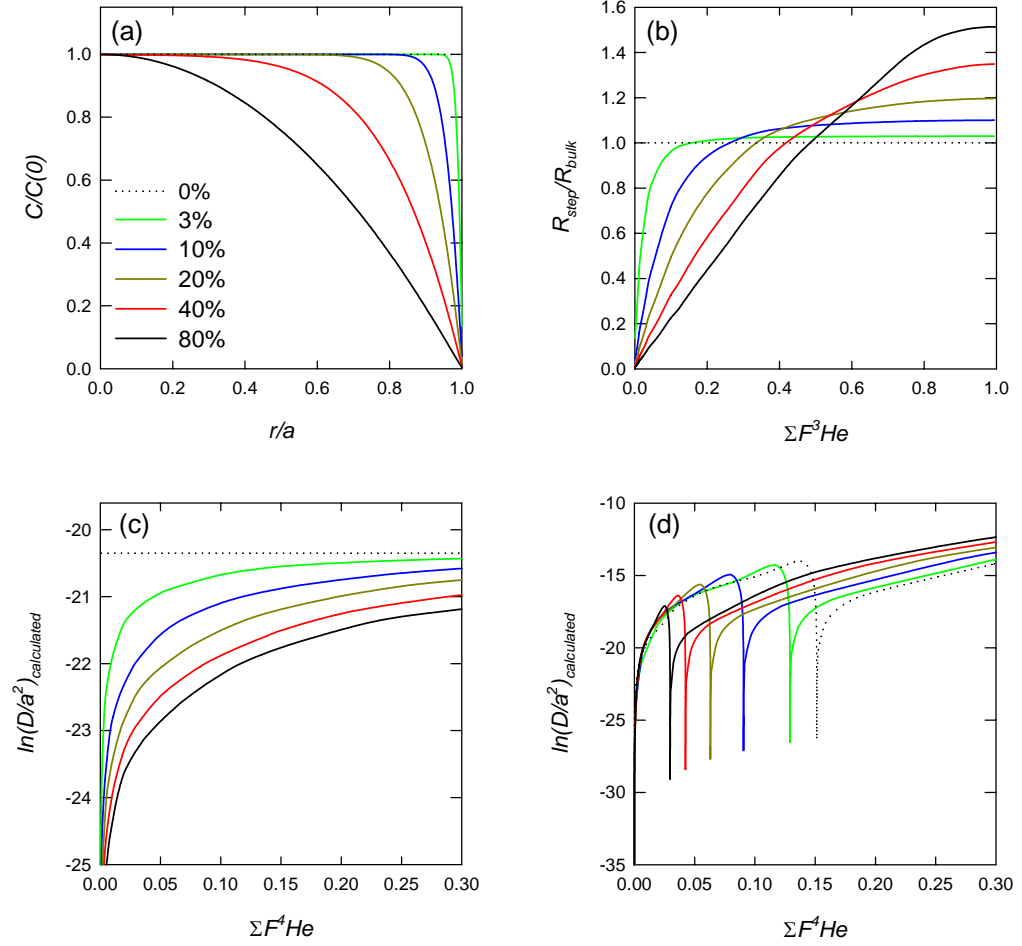


Figure 1. Stepwise outgassing simulation of isothermally evolved profiles. (a) initial  ${}^4\text{He}$  concentration,  $C$  (normalized to the concentration at the center of the domain,  $C(0)$ ) at the radial position  $r$  (normalized to domain radius,  $a$ ) within the spherical domain. The six concentration profiles shown in (a) were calculated according to isothermal accumulation and diffusion, excluding  $\alpha$ -ejection. The color of each profile corresponds to a deficit gas fraction; labels in % indicate the deficit gas fraction of each curve. (b) Step-heating simulations plotted as a ratio evolution diagram. The simulations are shown as continuous functions, although calculated at discrete heating steps. (c) and (d)  $\ln(D/a^2)_{\text{calculated}}$  values (according to Fechtig and Kalbitzer [24] assuming an initially uniform distribution) plotted vs. cumulative  ${}^4\text{He}$  release fraction,  $\Sigma F^4\text{He}$ . Simulations in

(c) were calculated using an isothermal heating schedule, those in (d) using a heating schedule with a single thermal cycle (up-down-up).

distributions in six different minerals that are variably He retentive or in one mineral calculated at six different constant temperatures; each curve reflects a unique  $(D/a^2)t$  product. We simulated release patterns for each profile using an isothermal heating schedule (Fig. 1c) and a “cycled” schedule (Fig 1d) that includes steps of both increasing and decreasing (retrograde) temperature.

Each of these profiles produces a unique curve in the three output diagrams. Release fractions and isotope ratios for each step and for the bulk material are the observed quantities in the ratio evolution experiment and permit construction of the ratio evolution diagram (Fig 1b). Although the values of discrete points along the curves in Fig. 1b depend on the function  $D(T)/a^2$ , the overall shape of a set of values reflects the concentration profile independent of diffusivity and heating schedule. Figs. 1c and 1d illustrate an alternative presentation of the same results. If a uniformly distributed isotope is not available, release fractions of only a diffusively rounded isotope distribution are measurable. If diffusion coefficients are calculated from a rounded profile (assuming an initially uniform profile), the calculated values,  $\ln(D/a^2)_{\text{calculated}}$  will underestimate the true values according to the shape of the profile. This is an artifact of the invalidly assumed initial condition. If the actual  $D(T)/a^2$  is known, this artifact can be used to constrain the shape of the profile by forward model

matching in  $\ln(D/\alpha^2)_{\text{calculated}}$  vs.  $\Sigma F_i$  plotting space. Figures 1c and 1d show that the calculation is highly sensitive to the heating schedule. Retrograde temperature steps result in a particularly distinct pattern with which to match a model.

#### 4.1.2 Monotonic cooling

In Figs. 2d-2e, we present step-heating simulations for a diffusion domain with  $a = 65 \mu\text{m}$ . Each simulation corresponds to a concentration profile calculated according to a constant cooling rate (0.1, 1, 10, and 100 °C/Myr) from 125 °C to 25 °C. These represent concentration profiles that might be expected, e.g., in an exhuming mountain range. The profiles were calculated either excluding (Fig. 2a) or including (Fig. 2b)  $\alpha$ -ejection. Each step-heating simulation used the isothermal heating schedule in Section 4.1.1.

In Fig. 2d, each of the profiles produces a distinct ratio evolution curve: faster cooling rates produce less rounded profiles (more He near the grain edge) and steeper trajectories on the ratio evolution diagram. The effects are most pronounced in the first ~10-20% of gas released. Maximum differences between the curves occur at steps when  $\Sigma F^3\text{He} \sim 10\%$ .

In the absence of diffusion, alpha ejection causes the He concentration profile to decline from unity to ~0.4 (in  $C/C(0)$  units) over the outermost ~20  $\mu\text{m}$  of the grain (e.g., see Fig 3b). This pattern is distinct from all diffusive profiles in that it is non-zero at the grain edge. The ratio evolution for this profile

(Fig. 3c) shows elevated ratios (compared to diffusion profiles) that increase nearly linearly up to  $\Sigma F^3He \sim 30\%$ . The effect of alpha ejection combined with monotonic cooling is shown in Figures 2b and 2e. The net effect of alpha ejection is to induce a distinctive linearity to the first  $\sim 30\%$  of the ratio evolution plot. Although the profiles resulting from the different  $t$ - $T$  paths are less distinct from each other, alpha ejection does not eliminate the differences between them. As with the previous models, the maximum differences between the curves occurs when  $\Sigma F^3He \sim 10\%$ . Because  $\alpha$ -ejection is temperature independent, it can dominate the shape of a profile under fast cooling conditions (where diffusive rounding is small), but becomes less significant under slow cooling (where diffusive rounding is high). The effect of  $\alpha$  ejection becomes increasingly large as domain size decreases toward the alpha stopping range of  $\sim 20 \mu\text{m}$ . This implies that alpha ejection may limit the recovery of  $t$ - $T$  information from smaller grains.

#### 4.1.3 *Monotonic cooling followed by 5 Myr at 25 °C*

In many geologic situations, a sample will have experienced long-term cooling followed by a near-surface, quasi-isothermal period. One example is a rock exhumed on a normal fault that has become inactive. In Fig. 2c, concentration profiles were calculated according to a constant cooling rate (0.1, 1,

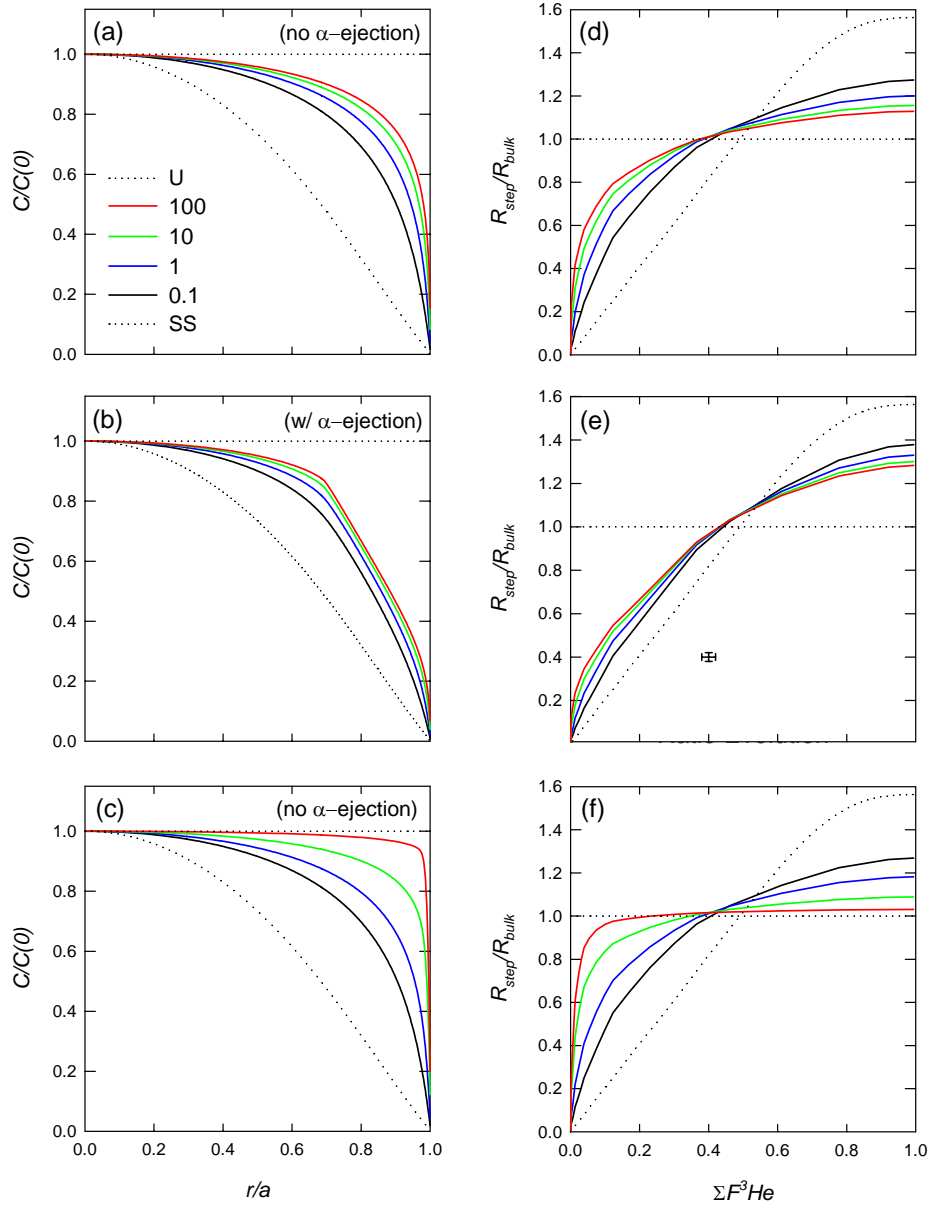


Figure 2. Step-heating simulations of profiles resulting from monotonic cooling. Concentration profiles are shown in panels a-c and the corresponding step-heating simulations shown as ratio evolution diagrams in panels d-f, respectively. The color of each curve corresponds to a particular cooling rate from 125 °C to 25°C; labels are in

units of °C/Myr. The  $t$ - $T$  simulations used to calculate the profiles in panels a and b ended when the temperature reached 25°C and in panel c was followed by isothermal accumulation at 25 °C for 5 Myrs. Shown for reference are the quantitative retention uniform distribution (U) and steady state (SS) profile simulations (black dotted curves). The simulations presented in a and c were calculated excluding the effect of  $\alpha$ -ejection.

10, and 100 °C/Ma) from 125°C to 25°C followed by 5 Myrs of isothermal holding at 25°C.

The simulations in Fig. 2f are again distinct, with maximum differences at steps when  $\Sigma F^3He \sim 10\%$ . Comparing Figs. 2a and 2c illustrates that low-temperature isothermal holding causes a profile to become more “square” and leads to greater retention of gas toward the domain edge. This is reflected in Fig. 2f as rapid ratio evolution in the initial steps of the ratio evolution diagram. The effect is greatest when a significant fraction of the gas is accumulated at temperatures where diffusion is negligible.

#### 4.1.4 *Distinct thermal histories for samples with a common He age*

In Fig. 3, we present simulations of a diffusion domain with  $a = 65 \mu\text{m}$  that experienced four very different thermal histories (Fig 3a) that would each result in a 10 Ma He age. The resulting concentration profiles in Fig. 3b yield very distinct ratio evolution diagrams (Fig. 3c). For instance, although the profiles calculated according to linear cooling from 88°C to 25°C over 15 Myrs (green curve) and isothermal holding at 64 °C from 15 Ma to 5 Ma followed by

instantaneous quenching to and quantitative retention at  $< 20^{\circ}\text{C}$  at 5 Ma (black curve) are similar, the ratios differ greatly when  $\Sigma F^3He < 10\%$

In an actual experiment, the bulk He age provides an important additional constraint on a sample's thermal history. In particular, when forward calculating model He profiles, the He age constrains the integrated  $^4\text{He}$  abundance that is permitted within the domain for each potential geologic  $t$ - $T$  path.

#### 4.2 *Inversions*

In the absence of simulated analytical error, all of the ratio evolution diagrams in Section 4.1 could be inverted to recover the concentration profiles to within round-off error (not shown). However, once errors are included the inversion becomes unstable; the ridge regression is designed to filter the influence of these errors. The extent to which random errors affect the inversion depends on the complexity of the profile and the number and distribution (in  $\Sigma F^3He$ ) of steps in the heating schedule. The inversion of more complicated release patterns tolerates less error than do simple profiles.

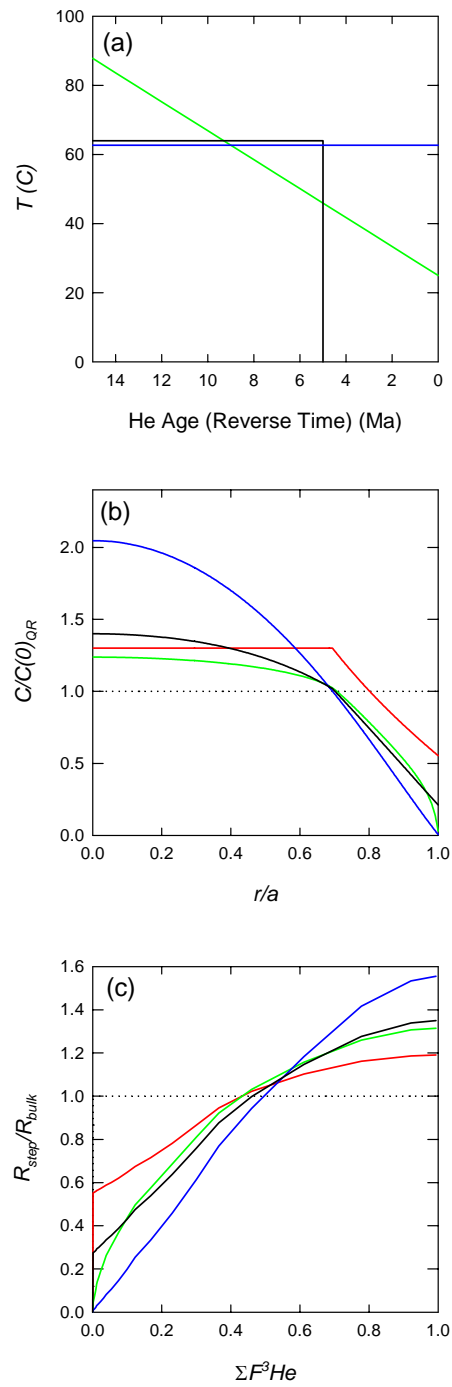


Figure 3. Simulations of profiles obtained from distinct thermal histories yielding an apatite (U-Th)/He age of 10 Ma. The color of each curve corresponds to a specific

accumulation model. The thermal histories are presented in panel a: instantaneous quenching at 10 Ma followed by quantitative retention at very low temperatures ( $< 20$  °C) for 10 Myrs (with and without  $\alpha$ -ejection; dotted black and red curves, respectively), isothermal holding at  $\sim 63$  °C for 100 Myrs resulting in a steady state  $^4\text{He}$  distribution (blue curve), constant cooling from 88°C to 25°C over 15 Myrs ( $dC/dt = 4.2$  °C/Myr; green curve), and isothermal holding at 64 °C from 15 Ma to 5 Ma followed by instantaneous quenching to  $< 20$ °C at 5 Ma followed by quantitative retention for 5 Myrs (solid black curve). The profiles, normalized as  $C/C(0)_{QR}$  (where  $C(0)_{QR}$  is the concentration at the center of the quantitative retention profile) are shown in panel b, and their corresponding ratio evolution diagrams are shown in panel c.

To illustrate the effect of error, we added a normally distributed, random 1% error to 21 simulated  $^4\text{He}$  and  $^3\text{He}$  release fractions for the relatively simple 10% deficit profile calculated by isothermal ingrowth (Fig. 1a). We added errors to each release step, and then renormalized them according to their new sum. The results of this simulation and inversion are presented in Fig. 4. The solid gray curve in Fig. 4b was calculated with a regularization parameter  $b = 0$ , equivalent to inverting equation (9) *without* regularization (see [28]). The solution  $\hat{\mathbf{b}}$  is clearly incorrect and illustrates that even a small amount of error can dramatically degrade the inverse solution.

The singular value decomposition spectrum for this example is shown in Fig. 4c. For  $i > 7$ , the  $\log(|\boldsymbol{\mu}_i^T \mathbf{f}|)$  spectrum is approximately flat, indicating that these components and therefore the linear solution is dominated by high frequency terms, which we assume are attributable to the added errors. By using

a value  $\log(b) = -3.18$  (corresponding to  $i < 7$ , dotted line in Fig 4c) in equation (11), the error-dominated components are filtered from the linear combination according to equation (10). After regularization, the inverted profile is nearly equivalent to the input profile (Fig 4b). The 1% errors used in this simulation are smaller than those anticipated in most stepwise experiments and hardly recognizable in the ratio evolution diagram (Fig. 4a). The difference between the solid gray and the dashed black curves clearly illustrates the importance of the ridge regression for inverting actual step-release data. In our companion paper, we show that data containing more significant errors can also be successfully inverted [14].

## 5. Discussion

The modeling results shown above demonstrate that significant information can be obtained from step heating of a sample with a natural  ${}^4\text{He}$  distribution and an artificial, homogeneous  ${}^3\text{He}$  distribution. How well can the distribution be obtained, and how can we quantify the confidence of a constrained profile? Ultimately, the number of heating steps and their distribution (in  $\Sigma F^3 H\theta$ ), and the precision and accuracy of the data, determine what resolution a given experiment has for constraining a He distribution. This is easily recognized for forward model matching, although less obvious for the inversion technique. We discuss each separately below.

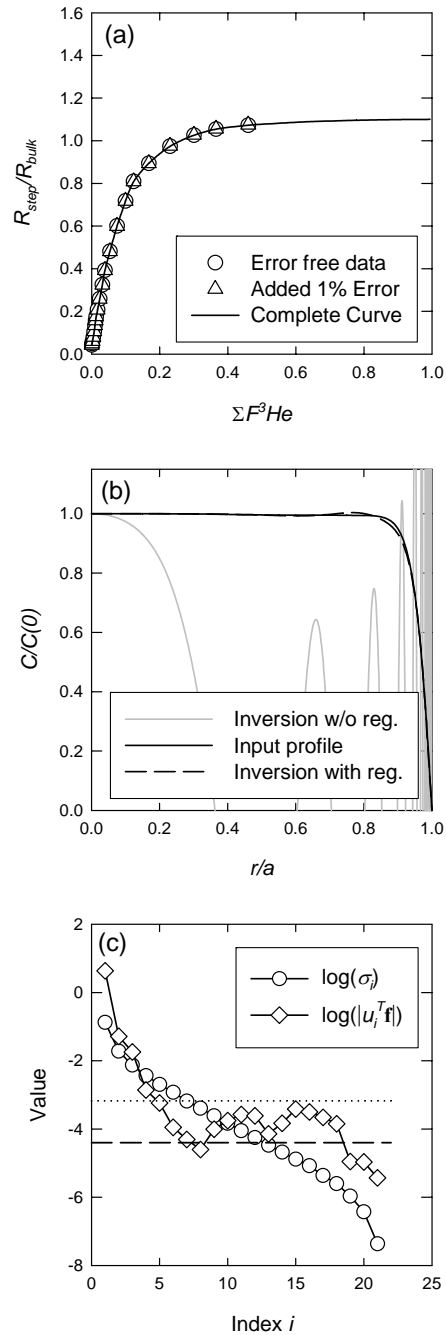


Figure 4. Effects of a 1% error in measured He data on the profile obtained using the inversion method. (a) Ratio evolution plot of the simulated error free data (circles) and

with added errors (triangles). (b) Input profile (solid black), the inverse solution of the error containing data calculated without regularization (solid gray) and the solution calculated with regularization (dashed black). (c) Singular value spectrum for the error containing data set is shown. Shown are the logarithms of the singular values ( $\log(\sigma)$ ; circles) and the absolute values of  $\left| \mathbf{u}_i^T \mathbf{f} \right|$  (see text;  $\log\left( \left| \mathbf{u}_i^T \mathbf{f} \right| \right)$ ; diamonds) each plotted vs. index number  $i$ . We minimized the influence of higher order, error-dominated terms by using a threshold  $i_p = 7$ , which roughly corresponds to the regularization parameters  $\log(h) = -3.18$  used in the inversion, shown as a dotted line.

### 5.1 Forward model matching

The forward models presented in Section 4.1 most clearly illustrate the potential utility and limitations of using a ratio evolution experiment to constrain a natural  $^4\text{He}$  distribution. The importance of measurement precision is clear in Figs. 1-3; e.g., typical differences are tens of percent in the  $^4\text{He}/^3\text{He}$  ratio. Because the above calculations use release *fractions*, precision and response linearity are more important than the accuracy of a set of measurements.

Helium isotope ratios and  $^3\text{He}$  relative abundances (i.e.  $\Sigma F^3\text{He}$ ) can routinely be measured to better than 1% relative standard error on samples of interest for this work [14], so the curves in Fig. 1b, 2d,f, and 3c should be easily resolvable from one another. A ratio evolution diagram provides a useful plotting space for forward model matching, and a set of measured values constrain a sample's unknown  $^4\text{He}$  profile to within the analytical uncertainty of the set of measurements.

For increasingly large deficit gas fractions, the concentration profiles in Fig. 1 become less distinct. For instance, there is approximately equivalent difference in  ${}^4\text{He}/{}^3\text{He}$  at a given  $\Sigma F^3\text{He}$  between the 10% and 20% deficit curves as there is between the 20% and 40% curves (Fig. 1b). The limiting case is the steady-state distribution in which radiogenic production and diffusive loss are balanced [42] shown in Fig. 5a. As this case is approached, differences become irresolvable, e.g., there is no obvious difference between 90% and 99% deficit curves. As a quantitative technique, stepwise degassing experiments have the greatest sensitivity for constraining profiles with small deficit gas fractions ( $< 40\%$ ). In all of the simulations, we find significant differences between values of  $R_{\text{step}}/R_{\text{bulk}}$  when  $0\% < \Sigma F^3\text{He} < 20\%$ . With knowledge of  $D(T)a^2$ , a heating schedule could be designed to maximize the number of steps in this range.

## 5.2 Inversion accuracy and resolution

The concentration profile obtained by inversion in Fig. 4b agrees well with the input profile, but not perfectly. Unfortunately, it is difficult to reliably estimate a confidence interval for the inverted profile due to the inability to accurately assign uncertainty to the regularization parameter,  $b$ . High frequency oscillation with respect to  $r$ , and zero crossings, would clearly indicate an unstable result. Given sufficient  ${}^3\text{He}$  and  ${}^4\text{He}$  abundances, the number of heating steps can be arbitrarily large, and the heating schedule could be designed for optimum

inversion conditions. Therefore, measurement precision primarily limits the accuracy of an inverted concentration profile.

Because the confidence level of a He profile will ultimately determine the confidence in an inferred thermal history, it may be beneficial to consider both the shape of an inverted profile and the associated ratio evolution diagram (alternatively  $\ln(D/a^2)_{\text{calculated}}$  vs.  $\Sigma F_i$ ) to check for consistency. In some instances, it may be possible to better constrain a profile by comparing forward model calculations with the observed ratio evolution diagram without relying on the inversion.

The resolution kernels (rows of the resolution matrix; not shown) for the inverse calculation reveal important limitations to this approach [29]. As expected, the resolution kernels indicate maximum resolving power toward the outer edge of the diffusion domain. The inversion of stepwise out-gassing data has greatest ability to “observe” the concentration profile towards the edge of the diffusion domain, and least resolving power towards the domain’s interior. Indeed, this is also found in our forward simulations.

The approximation used in the remaining gas fraction expression (equation (8)) limits the maximum value of  $\tau$  that can be inverted. This is problematic when inverting profiles with large deficit gas fractions because these more rounded profiles require larger values of  $\tau$  at each step to evolve measurable quantities of  $^4\text{He}$ . Because the approximation (equation (8)) is only

valid for  $\tau_i < 0.05$ , many data determined at the end of an experiment may not be useable in the inversion, although they would be observable in a ratio evolution diagram. To avoid this problem, an exact expression could be numerically integrated as an alternative to equation (8) (see [12, 28]). Because the exact expression contains an infinite series, an acceptable numerical evaluation could require significantly more computation time.

Another interesting limitation to the inverse calculation would result from a discontinuous concentration profile at the domain boundary. Inverting release fractions for a sample containing a discontinuity at  $r/a = 1$ , such as a uniform distribution, would result in a solution that contains high frequency oscillations near  $r/a = 1$  and an “overshoot” analogous to the Gibbs phenomenon.

### 5.3 Plotting space

In Figs. 1 and 4b we show three ways to represent experimental results: (i) the ratio evolution diagram ( $R_{step}/R_{bulk}$  vs.  $\Sigma F^3He$ ), (ii) a plot of  $\ln(D/a^2)_{calculated}$  vs.  $\Sigma F_b$  and (iii) the concentration profile obtained from inversion of the isotope data. There are advantages and disadvantages associated with each presentation.

The ratio evolution diagram most directly represents the measured quantities of an experiment. The diagram does not incorporate any artifacts associated with assumed initial conditions. The values are model independent and the shape of a plot lacks  $D/a^2$  dependence. For these reasons, the curves

presented in Fig. 1b are independent of the heating schedule and are generally applicable for model matching. For instance, the ratio evolution diagram for a 10% deficit gas fraction profile calculated by isothermal accumulation will be the same for any mineral.

The ratio evolution diagram can also be used to test for validity of assumptions of the method. There are the two limiting case  $^4\text{He}$  profiles for uniform production and diffusion: a uniform profile (quantitative retention) and a steady-state distribution (Fig 5a). Every other profile must plot between these two limits (Fig. 5b) and not in the “forbidden zones.” This is also true if  $\alpha$ -particles have been ejected from the domain. The ratio evolution diagram can thus be used to test for spatial heterogeneity of He production. If values plot within either of the “forbidden zones,” the  $^4\text{He}$  distribution does not smoothly decrease outward toward the domain’s edge as is required by diffusion and  $\alpha$ -ejection alone. For values  $\Sigma F^3\text{He} < 0.5$ , points plotting in the upper forbidden zone indicate  $^4\text{He}$  excess toward the domain’s edge, while those in the lower forbidden zone indicate  $^4\text{He}$  excess toward the domain’s interior. The converse statements are generally true for  $\Sigma F^3\text{He} > 0.5$ . Since a strongly heterogeneous  $^4\text{He}$  distribution likely reflects the parent nuclide distribution, the plot may identify non-uniform U and/or Th distributions, mineral inclusions or  $\alpha$ -implantation at the edge of the domain. Values plotting in a forbidden zone are a sufficient but not necessary condition for identification of these effects.

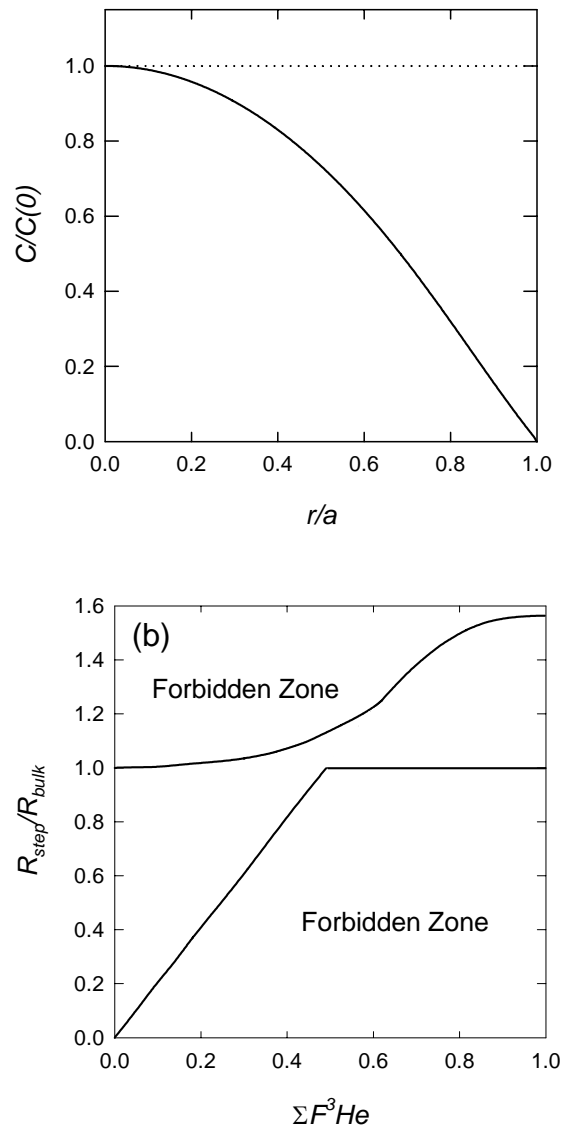


Figure 5. Limits for the spatially uniform  $^4\text{He}$  production-diffusion model. (a) The two limiting case concentration profiles: quantitative retention and steady state. (b) Ratio evolution diagram indicating allowed region for samples obeying uniform production-diffusion.

A plot of  $\ln(D/a^2)_{\text{calculated}}$  vs.  $\Sigma F_i$  can alternatively be used if a uniformly-distributed isotope is not available. The values in this plot are model dependent

and the shape depends strongly on the function  $D(T)/a^2$  and the heating schedule. If calculated for a non-uniform initial profile, the diffusion coefficients will be incorrect. However, the plot provides a high resolution plotting space for forward model matching. In some cases, it may be possible to constrain the function  $D(T)/a^2$  and the shape of a profile from a single analysis. For instance, as a rounded profile evolves throughout an experiment, the  $\ln(D/a^2)_{\text{calculated}}$  values approach the true values at a given temperature (Fig. 1c). For samples with relatively small deficit gas fractions ( $< 20\%$ ), the true  $\ln(D/a^2)$  values are reasonably approximated when  $\Sigma F \sim 0.75$ . For the 3%, 10%, and 20% deficit curves in Fig. 1c the ratio of  $(D/a^2)_{\text{calculated}}$  to  $(D/a^2)_{\text{true}}$  is 0.99, 0.97, and 0.95, respectively when  $\Sigma F = 0.75$ .

The inverted spherical profile plot (i.e., Fig. 4b) is the most readily interpretable presentation for describing a He distribution. However, as discussed above, it is susceptible to slight measurement inaccuracies and filtering bias.

Throughout this paper, we have focused on constraining the shape of a  $^4\text{He}$  profile. With the exception of the ratio evolution experiment, the methods above are also suitable for determining the shape of a natural  $^3\text{He}$  profile. A two aliquot experiment could potentially constrain a rounded cosmogenic  $^3\text{He}$  profile: one irradiated aliquot for determining  $D(T)/a^2$ ; the other for the profile. The irradiated aliquot would have to have sufficient  $^3\text{He}$  added to make the initial abundance negligibly small. Forward production/diffusion calculations assuming

a uniform cosmogenic  $^3\text{He}$  production rate could be used to generate model  $^3\text{He}$  profiles for comparison.

#### *5.4 Correcting (U-Th)/He ages*

Samples that have experienced only modest diffusive loss since He retention began have concentration profiles that include a nearly invariant segment in the core of the domain. This is revealed on the ratio evolution diagram by invariance in the  $^4\text{He}/^3\text{He}$  ratio at high cumulative  $^3\text{He}$  yields (e.g., the 3% and 10% deficit fraction curves in Figure 1b), much like the plateau in a  $^{40}\text{Ar}/^{39}\text{Ar}$  analysis. Under these conditions the deficit gas fraction can be used to correct the (U-Th)/He age for diffusive loss: corrected He content = measured content  $\div$  (1 - deficit gas fraction). This procedure inherently includes alpha ejection losses, so eliminates the need to make a geometry-based ejection correction. The plateau approach makes most sense for partially retentive samples that have experienced isothermal conditions since formation, e.g., volcanic phenocrysts and chemical precipitates, and for those samples with ambiguous alpha ejection correction (see [20] for an example of ambiguity).

#### *5.5 Constraining thermal histories*

The simulations shown in Figs. 2 and 3 indicate that ratio evolution experiments could constrain thermal histories from the analysis of just one crystal or a population of size-sorted crystals. This capability holds great potential for

thermochronometry, where constraining cooling rates currently requires model-dependent interpretation of a number of He ages from a given area, e.g., in a vertical sampling traverse. With the profiling method it would be possible to ascertain the same information from just one sample, and by analyzing several samples of different He age, it would be possible to obtain greater temporal resolution on the cooling rate. With additional chronological or geologic evidence, a  $^4\text{He}$  concentration profile could be used to more narrowly constrain a sample's thermal history. The most basic additional constraint is the (U-Th)/He age.

It is critically important that the forward thermal models use the function  $D(T)/a^2$  that is specific to the sample. The experimentally determined diffusivity,  $D$ , and the characteristic length scale,  $a$ , specify the sample. By transforming a problem of profile-model-matching to the spherical domain, the two parameters are inextricably linked. Modeled profiles, determined through forward calculation, must contain each. Application of a specific experimentally determined function  $D(T)/a^2$  (e.g., for Durango apatite) to an unstudied specimen possibly of a different grain size must be done with caution.

It is also important to recognize that the technique we describe in this paper constrains the shape of a He profile, and not a thermal history. Once a profile is determined it can then be used to constrain the possible  $t$ - $T$  paths that are consistent with its shape. Although the simulations presented in Section 4.1 uniquely resolved the concentration profiles corresponding to each  $t$ - $T$  path, they

did not *uniquely* constrain the cooling rates and thermal histories. For instance, the profiles and release patterns in Figs. 2c,f have similar shapes as those in Figs. 1a,b, despite having different  $t$ - $T$  paths. As thermal histories become increasingly complex, their resulting concentration profiles less uniquely reflect the corresponding  $t$ - $T$  paths. There will always be multiple thermal histories consistent with a given profile.

## 6. Conclusion

The ability to generate a uniform  $^3\text{He}$  distribution within minerals [14] permits a variety of new applications for He isotope geochemistry. Most simply, it permits He diffusivity measurements of samples that have insufficient natural He for such measurement, or of samples in which the natural concentration distribution is non-uniform. For samples with a measurable amount of natural  $^4\text{He}$ , variations in the  $^4\text{He}/^3\text{He}$  ratio over the course of a stepwise heating experiment reflect the initial  $^4\text{He}$  distribution within the sample. Both forward and inverse modeling can be used to constrain these profiles, which can in turn be used to (i) correct He ages for diffusion and alpha ejection losses in some circumstances, and (ii) constrain the  $t$ - $T$  path of the sample.

**Acknowledgement.** We thank D. Burnett, T. Schneider, B. Weiss, and F. Albarède for helpful discussions, and B. Watson and S. Kelley for reviews of the manuscript. We are grateful to T. Schneider for help with the inversion

mathematics. This work was supported by the National Science Foundation.

D.L.S. was supported by an N.S.F. Graduate Research Fellowship.

*Chapter 2*QUANTIFYING THE DIFFUSION KINETICS AND SPATIAL  
DISTRIBUTION OF RADIOGENIC  $^4\text{He}$  IN MINERALS CONTAINING  
PROTON-INDUCED  $^3\text{He}$ 

D. L. Shuster

K. A. Farley

Janet M. Sistierson

Donald S. Burnett

(This chapter was reprinted from *Earth and Planetary Science Letters* (2004), 217, 19-32)

**Abstract** - Apatite, titanite, and olivine samples were bombarded with a  $\sim 150$  MeV proton beam to produce  $\sim 10^8$  atoms/mg of spallation  $^3\text{He}$ . High precision stepped-heating experiments were then performed in which the artificial  $^3\text{He}$  and, for apatite and titanite, the natural radiogenic  $^4\text{He}$  were measured to characterize the diffusive behavior of each isotope. Helium-3 diffusion coefficients are in excellent agreement with concurrently and/or previously determined He diffusion coefficients for each mineral. Our results indicate that proton-induced

$^3\text{He}$  is uniformly distributed and that radiation damage associated with a proton fluence of  $\sim 5 \times 10^{14}$  protons/cm<sup>2</sup> does not cause noticeable changes in  $^4\text{He}$  diffusion behavior in at least apatite and titanite. Proton-induced  $^3\text{He}$  can therefore be used to establish He diffusion coefficients in minerals with insufficient natural helium for analysis or those in which the natural  $^4\text{He}$  distribution is inhomogeneous. In addition, step-heating  $^4\text{He}/^3\text{He}$  analysis of a mineral with a uniform synthetic  $^3\text{He}$  concentration provides a means by which a natural  $^4\text{He}$  distribution can be determined.

## 1. Introduction

Helium isotopes produced by radioactive decay of U and Th and by cosmic ray irradiation are useful for establishing cooling rates and exposure histories of minerals [11, 18, 19]. In a companion paper [49], we demonstrated that important information for interpretation of such data can be obtained by stepwise heating of samples in which a uniformly distributed isotope is available. In particular, a uniform, synthetic  $^3\text{He}$  distribution within minerals would be useful for (i) studying He diffusivity in phases that do not contain sufficient natural helium for accurate measurement, and (ii) for constraining the  $^4\text{He}$  concentration distribution of those that do [49]. A  $^4\text{He}$  concentration distribution can be used to correct (U-Th)/He ages for diffusive helium loss in some cases, and more generally places limits on the time-temperature path experienced by a sample. Here we demonstrate that a uniform  $^3\text{He}$  distribution can be generated

within minerals by bombarding them with a  $\sim 150$  MeV proton beam. Through stepwise heating  $^4\text{He}/^3\text{He}$  analysis of these samples we demonstrate that accurate diffusivities and  $^4\text{He}$  concentration profiles can be established using the synthetic  $^3\text{He}$ .

Moderate and high-energy proton bombardment produces spallation  $^3\text{He}$  from almost all target nuclei, in exactly the same way that cosmogenic  $^3\text{He}$  is produced in meteorites in space [19, 50]. Spallation reactions proceed through two stages [51]. In the “cascade” or fast stage, nucleon-nucleon scattering reactions knock out a few nucleons, leaving a residual nucleus with sufficient excitation energy to produce additional particle emission by an “evaporation” process. As the probability of a preformed mass 3 particle in the nucleus to be scattered in the cascade stage will be small, it is likely that the dominant  $^3\text{He}$  production mechanism is by evaporation. There are a large number of specific paths for the emission of  $^3\text{He}$ ; a probable one would be  $^{40}\text{Ca}(\text{p}, \text{pn})^{39}\text{Ca}^* \rightarrow ^{36}\text{Ar} + ^3\text{He}$ . Here pn refers to the cascade particles, the proton being the incident particle. The  $^{39}\text{Ca}^*$  is the excited residual that evaporates a  $^3\text{He}$ . In the center of mass system of the residual nucleus, an isotropic  $^3\text{He}$  distribution is generated within the solid. Most of the forward momentum of the incident proton is carried off by the cascade particles; however, there will be some forward velocity of the residual nucleus in the laboratory system, which in turn, produces a slight forward peaking in the  $^3\text{He}$  spatial distribution. The most probable energy of spallation  $^3\text{He}$  nuclei produced by this process is  $\sim 1\text{-}10$  MeV [51], which

translates to  $\sim 1$  to  $\sim 50$   $\mu\text{m}$  stopping distances in minerals [41, 51]. U series and Th series  $\alpha$  particles have similar energies. Thus, except for the forward peaking discussed above, we expect that spallogenic  $^3\text{He}$  and radiogenic  $^4\text{He}$  atoms will share a common distribution of sites within the mineral, at least to the extent that U and Th are uniformly distributed. As discussed below the potential complications from the forward peaking appear to be small. For similar reasons synthetic  $^3\text{He}$  should also be sited similarly to natural cosmogenic  $^3\text{He}$ . Note that proton-induced  $^3\text{He}$  significantly differs from neutron-activated  $^{39}\text{Ar}$  from  $^{39}\text{K}$ ; while  $^{39}\text{Ar}$  is derived from a specific parent isotope and resides very nearly in the original K site,  $^3\text{He}$  is produced from essentially all targets and its lattice siting is not closely tied to either its parent or to that of  $^4\text{He}$  [49].

Proton irradiation should produce  $^3\text{H}$  in subequal proportions to  $^3\text{He}$  [52], and this isotope decays to  $^3\text{He}$  with a half-life of 12.3 years. Although unlikely, it cannot be ruled out at present that  $^3\text{H}$  might migrate and site itself differently from helium, thus complicating the use of  $^3\text{He}$  as a proxy for radiogenic  $^4\text{He}$ . However, because all of our experiments were performed on samples less than a few months after irradiation, the tritiogenic component can be ignored.

Spallation  $^4\text{He}$  is also produced through high-energy proton bombardment, with a  $^4\text{He}/^3\text{He}$  ratio of order 10 [50]. In most minerals of interest for (U-Th)/He chronometry, the abundance of radiogenic  $^4\text{He}$  will overwhelmingly dominate, such that spallation  $^4\text{He}$  contributes negligibly to the

$^4\text{He}$  distribution. In addition, since natural  $^3\text{He}$  abundances are very low in these minerals [53], the synthetic  $^3\text{He}$  is the dominant source of this isotope. Thus in a practical sense the proton technique produces essentially pure  $^3\text{He}$  in minerals naturally carrying essentially pure  $^4\text{He}$ .

In this work we illustrate the production of spallation  $^3\text{He}$  from proton irradiation of minerals, and then demonstrate how it can be used as a proxy for natural radiogenic and cosmogenic helium in step-heating diffusion experiments. Our work shows that (i) proton irradiation does not significantly modify He diffusivities, e.g., through radiation damage; (ii) the synthetic  $^3\text{He}$  distribution is sufficiently uniform for our applications; and (iii) accurate He diffusivities and concentration profiles can be obtained using proton-induced  $^3\text{He}$  and the mathematical formulations presented elsewhere [24, 49].

## 2. Methods

### 2.1 Proton irradiation

Our samples were bombarded with a  $\sim 4.0$  nA, 147 MeV proton beam generated by a synchrocyclotron at Harvard Cyclotron Laboratory (HCL) over a  $\sim 10$  hour period in April 2002. The irradiation setup is shown in Fig. 1. The irradiations took place in air. A 12.5 mm brass aperture placed upstream of the 15 mm diameter target stack defined the diameter of the proton beam. The proton fluence was measured directly during irradiation by a thin foil

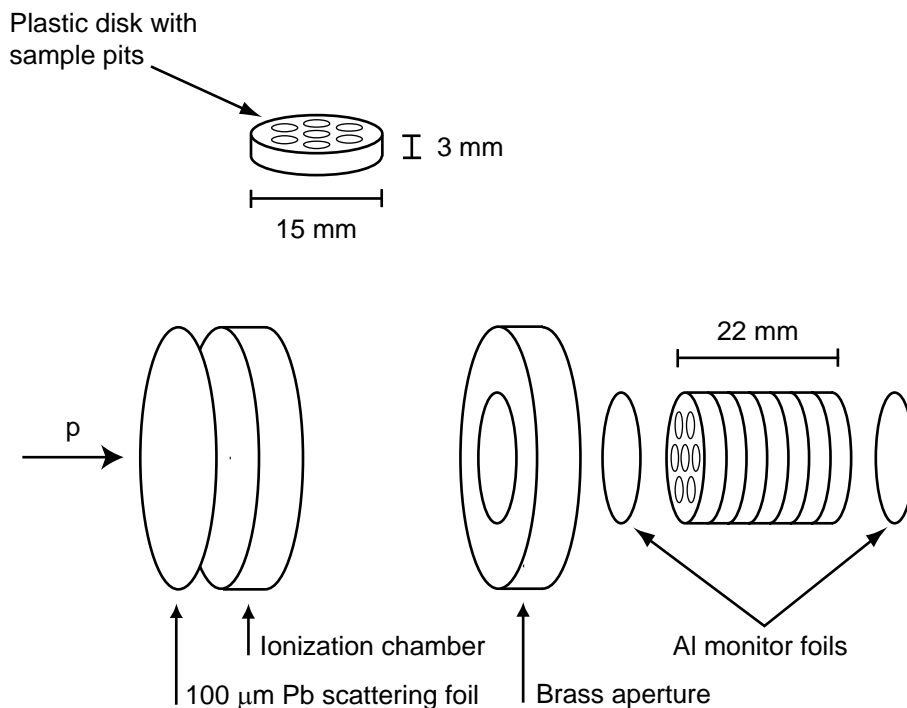


Figure 1. Schematic showing the irradiation setup. Samples were loaded into plastic target disks containing four or seven sample pits. Seven target disks were irradiated at once. Aluminum monitor foils were placed at the leading and leeward sides of the target stack. Note: not to scale.

transmission ionization chamber placed before the aperture. This chamber was calibrated using a Faraday cup prior to sample irradiation. The measured total fluence was  $3.3 \times 10^{14}$  p/cm<sup>2</sup>; this fluence was verified by measuring the production of <sup>22</sup>Na in Al monitor foils at the front and back of the target stack. To maximize the uniformity in <sup>3</sup>He production across individual samples, a 100 μm lead scattering foil was placed upstream of the target stack to generate a broad proton beam. In this configuration the beam intensity was approximately

Gaussian in shape and we estimated the beam intensity as a function of radial distance from the center of the target by measuring the proton transmission through apertures of different sizes.

Approximately 30 different samples ranging from ~1 to 50 mg each were loaded into Lucite disks; we irradiated seven disks at once (Fig. 1). Ultimately, the range of protons through the stack and the energy required for  $^3\text{He}$  production limits the number of disks and thus samples that can be irradiated at once. The range of 150 MeV protons through Lucite (the bulk of our target material) is approximately ~13 cm, however spallation  $^3\text{He}$  production drops off sharply below ~30 MeV [50]. This implies that  $^3\text{He}$  could be induced throughout a ~12 cm stack.

We *a priori* expected potential complications for generating a uniform  $^3\text{He}$  distribution. First, as discussed above, forward momentum may be transferred to the excited nucleus; a slight anisotropy in the  $^3\text{He}$  ejection trajectory across a grain is expected. However this effect appears insignificant (see discussion). More importantly, spallogenic  $^3\text{He}$  nuclei will be “ejected” from the surfaces of the irradiated mineral just like radiogenic  $^4\text{He}$  is ejected following U and Th decay [41]. Because the target minerals were loaded into Lucite disks that also produced spallogenic  $^3\text{He}$ , “ejected”  $^3\text{He}$  should be approximately balanced by “implanted”  $^3\text{He}$  from neighboring target atoms. For the fine-grained samples (< 200  $\mu\text{m}$ ; apatite and titanite), > 90% of the grains were adjacent to other grains of exactly the same chemical composition, therefore in those cases  $^3\text{He}$  ejection and

implantation would be in balance. Independent experiments have confirmed this “approximate balance” condition for other product/target combinations [54].

A final potential complication is heating of the sample during proton irradiation. Because He diffuses at moderate temperatures from many minerals, heating may cause both the natural and synthetic helium distributions to become rounded, compromising the experiment. We estimate that the proton beam energy exiting the target stack was  $\sim 115$  MeV, depositing  $\sim 35$  MeV within the stack. We can constrain the maximum temperature by assuming that the  $\sim 35$  MeV is deposited within the target as kinetic energy appearing as heat. At 4.0 nA, this energy deposition translates to  $\sim 0.15$  W, from which we estimate a maximum temperature during irradiation of  $\sim 1$ - $2$  °C above ambient, or  $< 30$  °C. The maximum time and temperature that can be tolerated depends on the He diffusion characteristics of the mineral being investigated but, as we show below, for apatite, titanite, and olivine there is no indication of diffusive rounding.

In addition to  $^3\text{He}$ , proton bombardment also produces many short-lived radionuclides that could present a radiation exposure risk. Following irradiation and five days of decay, the samples in the target holder had an in-contact activity of  $\sim 30$   $\mu\text{Sv/hr}$  (3 mrem/hr), and after 10 days,  $\sim 15$   $\mu\text{Sv/hr}$ . After 17 days radioactivity levels were considered sufficiently low to permit safe handling and shipment back to Caltech.

## 2.2 Diffusion experiments

The design of our diffusion experiments drew upon previous work in  $^{40}\text{Ar}/^{39}\text{Ar}$  [25, 55] and (U-Th)/He dating [53]. The sample was held at a known temperature ( $T_i$ ) for a known time ( $t_i$ ) in a volume of  $\sim 300\text{ cm}^3$  under static vacuum [56]. Following each heating step  $i$ , we measured released helium on a MAP 215-50 sector field mass spectrometer calibrated by external standardization. At the end of an experiment, samples were fused at  $\sim 1500\text{ }^\circ\text{C}$  in a resistance furnace. Details of the analytical techniques are described elsewhere [11, 56, 57], but were modified such that both helium isotopes were detected on a pulse counting electron multiplier. Heating steps typically yielded 1-500 cps and  $10^4$  to  $10^6$  cps for  $^3\text{He}$  and  $^4\text{He}$ , respectively. From reproducibility of standards in this response range, we estimate our measurement precision to be  $\sim 5\%$  to  $0.5\%$  relative standard error for  $^3\text{He}$  (low to high count rate, respectively) and generally much better than  $\sim 0.5\%$  for  $^4\text{He}$ .

We monitored and corrected for possible long-term (days) drift in sensitivity and characterized blanks by interspersing blank and standard analyses throughout an experiment. We routinely maintained diffusion cell  $^3\text{He}$  blanks  $< 0.2$  cps ( $\sim 2 \times 10^4$  atoms) and  $^4\text{He}$  blanks  $< 1500$  cps ( $\sim 2 \times 10^8$  atoms) during our experiments, and performed blank corrections on each measurement.

We converted measured  $^3\text{He}$  step-release fractions ( $F_i^{^3\text{He}}$ ) to diffusion coefficients using [24]. From this calculation, and the temperature of each step,

we generated Arrhenius plots to determine the activation energy,  $E_a$ , and frequency factor,  $D_0/a^2$  by linear regression to define the function  $D(T)/a^2 = D_0/a^2 \exp(-E_a/RT)$  ( $D$  is the diffusion coefficient,  $a$  is the characteristic length scale of the diffusion domain,  $R$  is the gas constant). We assumed spherical geometry and an initially uniform  $^3\text{He}$  concentration profile. To verify the assumed initial condition, we incorporated temperature cycling in our experiments; i.e., we used heating schedules that included steps of both increasing (prograde) and decreasing (retrograde) temperature [49].

### 3. Samples

For this initial study we focused on materials with well-characterized  $^4\text{He}$  diffusion parameters to test the reliability and assumptions of the method, specifically Durango apatite, titanite from the Fish Canyon tuff (FCT), and olivine from Guadalupe Island. The analyzed Durango apatite and FCT titanite were aliquots of the exact samples previously studied for  $^4\text{He}$  diffusion [4, 5].

The Durango apatite sample consists of fragments produced by crushing a slab cut from the interior of a large, gem-quality fluorapatite from Cerro de Mercado, Durango, Mexico [58].  $^4\text{He}$  diffusivity has been extensively studied in Durango apatite [4, 16, 53]. The material analyzed in this study is an aliquot of that previously analyzed by [4, 53]: angular shards sieved to 160-180  $\mu\text{m}$ . Some zonation of U and Th may exist within this sample [59], but its magnitude and length scale are unlikely to have affected the  $^4\text{He}$  profile within individual

fragments. Similarly, because the crystal interior has not experienced diffusive loss or  $\alpha$ -ejection [41], the  $^4\text{He}$  distribution is expected to be very nearly uniform.

Geochronology of the Fish Canyon tuff (FCT) was recently described [60,61]. Because the FCT titanite was collected from the quickly cooled tuff (eruption age =  $28.0 \pm 0.3$  Ma; [60]), this material is not likely to have a diffusively rounded  $^4\text{He}$  distribution. The analyzed aliquot contained grains ranging from 75 to 220  $\mu\text{m}$ , with 70% between 125 and 190  $\mu\text{m}$ . On the average, we expect euhedral grains to have an  $F_T$  value of 0.91, representing 9% of the  $^4\text{He}$  lost by  $\alpha$ -ejection. However, most grains were non-euhedral fragments. Despite the inherent complication of analyzing a distribution of grain sizes, the analyzed material is an aliquot of that studied for  $^4\text{He}$  diffusion [5].

A gem-quality  $\text{Fo}_{75}$  -  $\text{Fo}_{80}$  olivine megacryst from Guadalupe Island [62] was also analyzed. We selected olivine free of fluid inclusions for this study, and analyzed a nearly spherical fragment of radius  $\sim 690$   $\mu\text{m}$ . Our analyses of other olivines from this locality indicate very low concentrations of natural He in this material, presumably located in fluid inclusions.

## 4. Results

### 4.1 *Proton-induced $^3\text{He}$ production*

Estimated proton fluences and measured  $^3\text{He}$  yields are listed in Table 1. In this irradiation configuration, there was a known radial variability in the proton

fluence across the disks, which we measured by determining the transmission through apertures of increasing diameter. For instance, the innermost 3.6 mm received an average fluence of  $\sim 5.2 \times 10^{14}$  p/cm<sup>2</sup>, whereas the outermost 2.8 mm received only  $\sim 2.3 \times 10^{14}$  p/cm<sup>2</sup>. Although a slight energy gradient exists along the beam axis, variability in the along-axis fluence is expected to be negligible. Diffusion experiments were performed on single or multiple ( $\sim 200$ ) grains from individual sample pits. Based on the apparent radial gradient, we conclude that the relative dose across a given sample pit ( $\sim 1$  mm) varied by no more than  $\sim 10\%$ , and we expect that individual apatite or titanite grains ( $\sim 150$   $\mu\text{m}$ ) received a uniform dose to within  $\sim 1.5\%$ . The homogeneity in <sup>3</sup>He production is supported by the <sup>3</sup>He results presented below. Because the single analyzed olivine grain diameter was approximately 1.4 mm, it could potentially have received a dose varying by  $\sim 10\%$  across the grain (perpendicular to the beam direction) and any decrease in production cross section along the beam axis is negligible.

Helium-3 yields are a function of the incident proton energy, total proton fluence and target chemistry specific to a given sample, but averaged  $1.9 \times 10^8$  atoms/mg. The values in Table 1 dictate the sample mass required for accurate <sup>3</sup>He detection in a step heating experiment. For instance, we generated  $\sim 10^6$  atoms of <sup>3</sup>He in a single  $\sim 4$   $\mu\text{g}$  Durango apatite shard. Given our <sup>3</sup>He sensitivity, this translates to a total response of  $\sim 10$  cps/shard. Thus a multistep out-

Table 1: Dose/yield summary

Phase	Fluence ( $\times 10^{14}$ p/cm <sup>2</sup> )	Proton Energy (MeV)	[ <sup>3</sup> He] ( $\times 10^8$ atoms/mg)	[ <sup>4</sup> He] ( $\times 10^{10}$ atoms/mg)
Apatite	5.20	~140	1.97	367
Titanite	3.19	147	1.79	1435
Olivine	3.19	~140	1.82	< 3

The proton fluence of each sample was estimated by its radial position within the target stack as discussed in the text. Uncertainty in these doses is estimated to be on average  $\pm 10\%$  relative error. Analytical techniques for determining <sup>3</sup>He and <sup>4</sup>He concentrations are described in [11, 56, 57]. We estimate the uncertainty to be better than  $\pm 2\%$  for each. Note that <sup>4</sup>He in these minerals is almost exclusively natural and radiogenic rather than synthetic.

gassing experiment requires at least a few tens of grains and the <sup>3</sup>He measurements on apatite and titanite were performed on aggregates of ~200 grains (~1 mg mass). The olivine grain was sufficiently large that a single grain experiment could be performed.

Based on an expected spallation <sup>4</sup>He/<sup>3</sup>He production ratio of ~10 [50], and the observed He concentrations in the apatite [53] and titanite [5], the spallogenic <sup>4</sup>He fraction is negligible:  $\sim 5 \times 10^{-4}$  and  $1 \times 10^{-4}$ , respectively. Spallogenic <sup>4</sup>He more significantly contributes to the <sup>4</sup>He budget of the olivine sample, amounting to perhaps 6% of the total. The natural <sup>3</sup>He abundances of the apatite and titanite samples are negligible compared to the spallation <sup>3</sup>He [5,

53]. Assuming the Guadalupe olivine contains a natural  ${}^4\text{He}/{}^3\text{He}$  ratio of  $1.4 \times 10^5$  [63], and all of the  ${}^4\text{He}$  is natural, the natural  ${}^3\text{He}$  content will at most be  $\sim 1 \times 10^{-3}$  of the total  ${}^3\text{He}$  budget.

#### 4.2 Diffusion experiments

Results of the three diffusion experiments are presented as Arrhenius plots in Figs. 2a-c. The three minerals have independently known helium diffusivity with which we compare our  ${}^3\text{He}$  results. Durango apatite and FCT titanite were previously studied in our lab for radiogenic  ${}^4\text{He}$  diffusion [4, 5, 53], and we compare our olivine results with those determined using natural cosmogenic  ${}^3\text{He}$  in a different sample by Trull et al. [23]. Regression statistics and the  ${}^3\text{He}$  diffusion parameters  $D_0/a^2$  and  $E_a$  are summarized for the three experiments in Table 2. We also present the concurrently determined  ${}^4\text{He}$  results for the irradiated apatite and titanite experiments; the Guadalupe olivine sample contained insufficient  ${}^4\text{He}$  for accurate measurement. To compare the olivine results with previous work, we converted values of  $\ln(D/a^2)$  to  $\ln(D)$  by dividing by the olivine grain radius, assuming that the physical grain equals the diffusion domain.

Figure 2a presents our results for diffusion of spallogenic  ${}^3\text{He}$  and natural  ${}^4\text{He}$  from Durango apatite, along with previous results [4]. Because  ${}^4\text{He}$  diffusion has been well-characterized in this material [4, 53] and it is known to have a uniform  ${}^4\text{He}$  distribution, it is an ideal candidate for verifying several

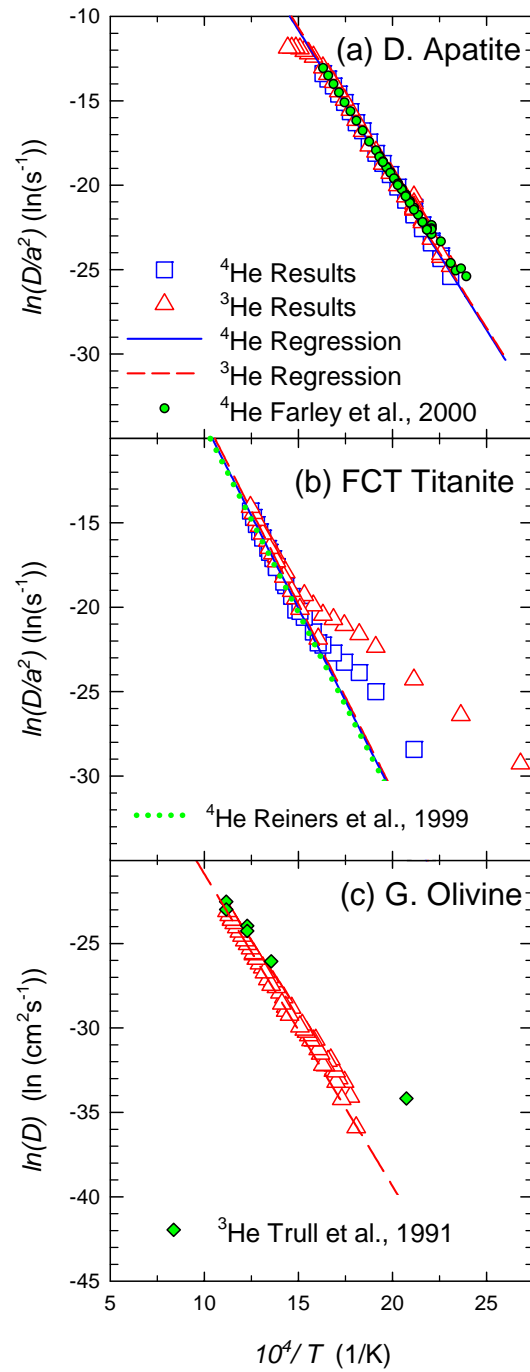


Figure 2. Arrhenius plots for (a) Durango apatite, (b) FCT titanite, and (c) Guadalupe olivine. Open triangles are values calculated from  $^3\text{He}$  and open squares calculated from

$^4\text{He}$  for the irradiated samples. The dashed lines indicate least squares regression through subsets of the  $^3\text{He}$  results and the solid lines the  $^4\text{He}$  results in (a) and (b). Also shown as circles in (a) are  $^4\text{He}$  results from [4], as dotted line in (b) are  $^4\text{He}$  results from [5], and as diamonds in (c) are cosmogenic  $^3\text{He}$  results from [23] for a different olivine sample.

assumptions of our method. The  $^3\text{He}$  Arrhenius plot shows strong linearity between 150 and 350 °C and diffusion coefficients that are in excellent agreement with those previously determined for  $^4\text{He}$ . We find within analytical uncertainty equivalent diffusivity parameters for both isotopes in the irradiated experiments (Table 2).

To quantify the relationship between proton-induced  $^3\text{He}$  and radiogenic  $^4\text{He}$  diffusivity in Durango apatite, we present an additional experiment as a ratio evolution diagram [49] of  $R_{step}/R_{bulk}$  vs.  $\Sigma F_i^{^3\text{He}}$  (where  $R = ^4\text{He}/^3\text{He}$ ,  $R_{step}$  is the measured ratio at each step,  $R_{bulk}$  is the bulk ratio, and  $\Sigma F_i^{^3\text{He}}$  is the cumulative  $^3\text{He}$  release fraction; Fig. 3) in which we see an effectively constant  $^4\text{He}/^3\text{He}$  ratio at each step of the experiment extending out to high gas yield. Deviation from the bulk ratio ( $R_{bulk}$ ) occurs only during the steps at high values of  $\Sigma F_i^{^3\text{He}}$ , which may indicate that  $^4\text{He}$  diffusivity is slightly higher than  $^3\text{He}$  (see discussion below). The results presented in Fig. 3 also indicate a lack of observable difference between the  $^3\text{He}$  and  $^4\text{He}$  spatial distributions.

Table 2. Diffusion coefficient summary

Phase	radius ( $\mu\text{m}$ )	Isotope	$R^2$	d.f.	$\ln(D_0/a^2)$ ( $\ln(\text{s}^{-1})$ )	(+/-)	$E_a$ (kJ/mol)	(+/-)
Apatite	160-180	$^3\text{He}$	0.998	22	16.03	0.32	147.87	1.32
		$^4\text{He}$	0.999	22	15.82	0.20	147.65	0.85
		$^4\text{He}^a$	0.998	49	13.51	0.30	136.72	1.21
Titanite	75-220	$^3\text{He}$	0.998	12	13.34	0.45	183.66	2.71
		$^4\text{He}$	0.997	12	12.87	0.48	182.55	2.93
		$^4\text{He}^b$	n.a.	n.a.	12.30	0.70	182.95	10.00
Olivine	~690	$^3\text{He}$	0.999	23	3.00	0.17	153.78	1.09
		$^3\text{He}$	0.993	54	0.93	0.29	139.60	1.67

Standard errors in the regression statistics are reported at the 95% confidence level. d.f., the number of degrees of freedom in the regression.

<sup>a</sup> From [4]

<sup>b</sup> From [5]

We observe a small  $^3\text{He}$  *excess* ( $\sim 1\%$  of the total  $^3\text{He}$  budget) in the initial steps of both Durango experiments (see Fig. 2a), where we define an excess to be a gas fraction resulting in anomalously high diffusion coefficients with respect to the main array. High diffusivity in the initial and low-temperature steps was also observed in this and previous studies of  $^4\text{He}$  [4]. The excess may be related to small grains adsorbed to the shard surfaces (see discussion below). We therefore excluded these steps from Arrhenius regressions.

The resulting Durango apatite diffusion parameters are  $E_a = 148 \pm 1$  (kJ/mol) and  $\ln(D_0/a^2) = 16.0 \pm 0.3$  ( $\ln(\text{s}^{-1})$ ) (SE;  $n = 23$ ) and  $E_a = 14$

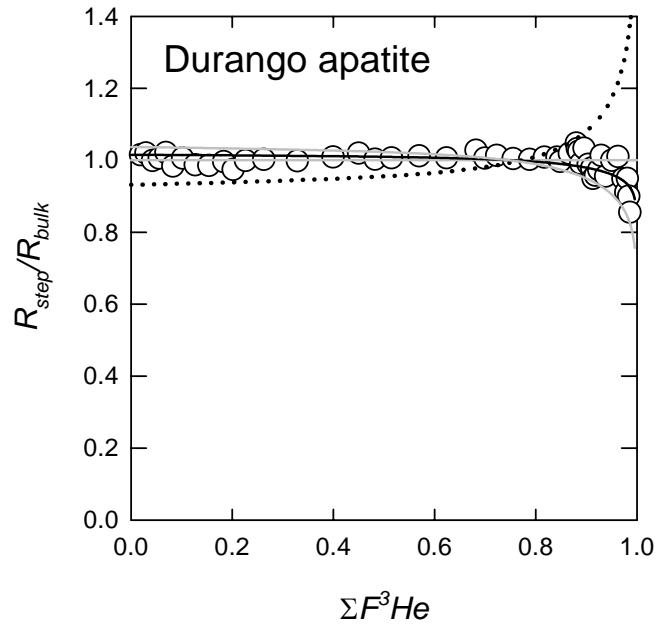


Figure 3. Durango apatite ratio evolution diagram. Shown are measured isotope ratios for each release step,  $R_{step}$  ( $R=^4\text{He}/^3\text{He}$ ), normalized to the bulk ratio  $R_{bulk}$  plotted vs. the cumulative  $^3\text{He}$  release fraction,  $\Sigma F^3\text{He}$ . Four diffusion models are shown. The model that best fits the entire dataset,  $D^4\text{He}/D^3\text{He} = 1.03$ , is shown as a solid black curve with 95% confidence intervals shown as solid gray curves:  $D^4\text{He}/D^3\text{He} = 1.00$  and  $1.07$ , respectively. We also show as a dotted curve the model corresponding to the inverse root mass relationship:  $D^4\text{He}/D^3\text{He} = \sqrt{m_3/m_4} = 0.868$ . The size of the points roughly indicates the average analytical uncertainty throughout the experiment.

(kJ/mol) and  $\ln(D_0/a^2) = 15.8 \pm 0.2$  ( $\ln(\text{s}^{-1})$ ) (SE;  $n = 23$ ) for  $^3\text{He}$  and  $^4\text{He}$ , respectively. The  $^3\text{He}$  and  $^4\text{He}$  results are statistically indistinguishable from each other. The corresponding closure temperatures for each isotope are  $78^\circ\text{C}$  and  $79^\circ\text{C}$ , respectively (assuming  $dT/dt = 10^\circ\text{C}/\text{Myr}$  throughout this paper). These results are in good agreement with earlier studies [4] (see comparison in Fig. 2a).

Helium-3 and  $^4\text{He}$  diffusivities for FCT titanite are shown in Fig. 2b. The most obvious feature in the plot is a break in slope occurring at  $\sim 390^\circ\text{C}$  that separates two distinct linear arrays that are present for both isotopes. A similar pattern was also observed in an un-irradiated aliquot of the same material [5]. The 10 points in the lower temperature array represent  $\sim 1\%$  of the total  $^3\text{He}$  budget; the  $^4\text{He}$  diffusivities are consistently lower than the  $^3\text{He}$  diffusivities within this array (initially by several orders of magnitude), and converge at higher  $^3\text{He}$  yield (see discussion below). Reiners and Farley [5] also observed high  $^4\text{He}$  diffusivity in the initial and low-temperature steps. Once the initial 1% is removed, we find good agreement between  $^3\text{He}$  and  $^4\text{He}$  diffusivities and a strong linear correlation between  $\ln(D/a^2)$  and  $10^4/T$  for steps between  $350^\circ\text{C}$  and  $530^\circ\text{C}$ , including a retrograde temperature cycle.

The regressed FCT titanite diffusion parameters from the higher temperature array are  $E_a = 184 \pm 3$  (kJ/mol) and  $\ln(D_0/a^2) = 13.3 \pm 0.5$  ( $\ln(\text{s}^{-1})$ ) (SE;  $n = 13$ ), and  $E_a = 183 \pm 3$  (kJ/mol) and  $\ln(D_0/a^2) = 12.9 \pm 0.5$  ( $\ln(\text{s}^{-1})$ ) (SE;  $n = 13$ ) for  $^3\text{He}$  and  $^4\text{He}$ , respectively. The difference between  $^3\text{He}$  and  $^4\text{He}$  diffusivity is statistically insignificant. The corresponding closure temperatures for each isotope are  $185^\circ\text{C}$  and  $186^\circ\text{C}$ , respectively. These results are in excellent agreement with earlier work [5] ( $E_a = 176\text{-}190$  (kJ/mol) and  $\ln(D_0/a^2) = 11.6\text{-}13.0$  ( $\ln(\text{s}^{-1})$ );  $T_c = 181\text{-}201^\circ\text{C}$  for the same material. A ratio evolution diagram [49] calculated from the FCT titanite results (not shown) is consistent with a small fraction of  $^4\text{He}$  lost by  $\alpha$ -ejection or diffusion (see discussion below).

Diffusion results from the Guadalupe olivine megacryst are shown in Fig. 2c as  $\ln(D)$  vs.  $10^4/T$  using  $a = 690 \mu\text{m}$ . As with the apatite and titanite analyses, we observe small  $^3\text{He}$  excess in the initial and low-temperature heating steps. The  $^3\text{He}$  released in the initial 30 heating steps, resulting in anomalously high diffusivity, amounts to  $\sim 1.5\%$  of the total  $^3\text{He}$  budget. Once the excess is removed, we find linear correlation between  $\ln(D/a^2)$  and  $10^4/T$  for steps between 280 and 620  $^\circ\text{C}$  and good agreement with  $^3\text{He}$  diffusion coefficients previously determined for another olivine sample [23], particularly at higher temperatures. The results remain linear throughout a retrograde cycle between 510 and 415  $^\circ\text{C}$ .

We present statistics for two regressions in Table 2: one including all the olivine data, the other excluding the initial steps containing excess  $^3\text{He}$ . We find good agreement between the regressions, with a stronger correlation coefficient for the latter ( $r^2 = 0.993$  vs.  $r^2=0.999$ ). The olivine diffusion parameters calculated from the regressions are  $E_a = 140 \pm 2$  (kJ/mol) and  $\ln(D_o/a^2) = 0.93 \pm 0.3$  ( $\ln(\text{s}^{-1})$ ) (SE;  $n = 55$ ), and  $E_a = 154 \pm 1$  (kJ/mol) and  $\ln(D_o/a^2) = 3.0 \pm 0.2$  ( $\ln(\text{s}^{-1})$ ) (SE;  $n = 24$ ), respectively. Although the second regression uses less data, we prefer it because it is based only on steps that remain linear throughout cycled heating steps. The corresponding closure temperatures for each regression are 191  $^\circ\text{C}$  and 210  $^\circ\text{C}$ , respectively.

## 5. Discussion

Our experiments show that a beam of 150 MeV protons produces sufficient spallation  $^3\text{He}$  to measure in a multi-step diffusion experiment. In order to use the synthetic  $^3\text{He}$  as a proxy for the diffusion of natural  $^4\text{He}$  in minerals as we propose elsewhere [49] we must also establish that (i) the  $^3\text{He}$  profile is uniform across the diffusion domain; (ii) heating and/or radiation damage have not modified He release characteristics from the minerals; and (iii)  $^3\text{He}$  diffuses at an equivalent rate as or a rate quantitatively relatable to  $^4\text{He}$ .

### 5.1 $^3\text{He}$ profile uniformity

Two lines of evidence support the conclusion that the  $^3\text{He}$  profile produced within individual grains by proton irradiation is essentially uniform. First, in our step-heating experiments we used a cycled heating schedule including both prograde and retrograde steps. As we [49] and others [24] have discussed, non-uniform diffusant profiles will yield erroneous diffusion coefficients when using the standard formulation of [24], which assumes a uniform initial profile. The magnitude of this error decreases as the experiment proceeds, which causes points to deviate from linearity in an Arrhenius plot, especially when retrograde steps are included [49]. The apatite experiment shown in Fig. 2a most clearly illustrates linearity on the Arrhenius plot, in both prograde and retrograde steps. With the exception of a small initial excess, which we attribute to a different phenomenon, all points lie on a single line arguing in favor of uniformity.

A second line of evidence supporting uniformity in the grains'  $^3\text{He}$  spatial distribution comes from Fig. 3. For independent reasons described above we believe that the  $^4\text{He}$  profile in the apatite fragments is uniform. As shown in the ratio evolution diagram (Fig. 3), the  $^4\text{He}/^3\text{He}$  ratio is essentially invariant. Without special circumstances, this can only mean that  $^3\text{He}$  and  $^4\text{He}$  diffuse at approximately the same rate (see below) and that, like the  $^4\text{He}$  profile, the  $^3\text{He}$  profile within the individual grains is uniform. This conclusion is insensitive to any slight variability in the  $^3\text{He}$  production rate that may have existed between grains (for instance grains separated by  $\sim 1$  mm during the irradiation but analyzed together). Note that these combined observations also preclude the possibility that heating during irradiation has caused diffusive rounding of the profile of either isotope. Lastly, we conclude that the slight anisotropy in  $^3\text{He}$  production that we expected due to preferential forward momentum transfer to the target nucleus does not significantly bias our diffusivity results.

While the titanite and olivine both have modest deviation from both of these behaviors, it is difficult to imagine that the  $^3\text{He}$  distribution is uniform in some samples but not others located just a few millimeters away.

### *5.2 Do $^3\text{He}$ and $^4\text{He}$ diffuse at the same rate?*

The ratio evolution diagram [49] is highly sensitive to differences between  $^3\text{He}$  and  $^4\text{He}$  diffusivity if each isotope has an initially uniform distribution. If  $^3\text{He}$  diffusivity is higher than that of  $^4\text{He}$ , we expect the measured  $^4\text{He}/^3\text{He}$  ratios

( $R_{step}$ ) to be initially lower than the bulk ratio and progressively increase to values higher than the bulk ratio as  $\Sigma F^3He$  approaches unity. Especially in the steps at high  $\Sigma F^3He$  this distillation effect can be very pronounced, yet this is not seen in the apatite data. Using a similar diagram, Trull and Kurz (1993 and 1999) found natural  $^3He$  diffusivities to be 1.09, 1.04, and 1.08 times faster than  $^4He$  diffusivities in olivine, clinopyroxene, and basaltic glass, respectively [39, 40]. Each of these relationships between  $D^3He$  and  $D^4He$  deviate from the simple kinetic theory of gases, which predicts  $D^3He/D^4He = 1.15$ .

From the constancy in  $^4He/^3He$  ratio over the course of the Durango apatite experiment (Fig. 3) we conclude that proton-induced  $^3He$  and radiogenic  $^4He$  have nearly equivalent diffusivity in that material, with  $^4He$  potentially diffusing slightly faster than  $^3He$ . By calculating the residual sum of squares between our observations and various models, we find that the data are most consistent with a  $D^4He/D^3He$  ratio of 1.03 ( $^{+0.04}/_{-0.03}$  at 95% confidence). If we exclude the last five data points (for  $\Sigma F^3He > 0.96$ ), the data are more consistent with a  $D^4He/D^3He$  ratio of 1.00; we find a residual sum of squares that is approximately half that of the  $D^4He/D^3He = 1.03$  model.

The kinetic theory of gases and most solid-state diffusion theories suggest a mass-dependent relationship between isotopic mass and diffusivity, but the magnitude and sign of the effect is uncertain [40] and a departure from the simple “inverse root mass” relationship is clearly evidenced by previous

work [39, 40]. That we observe effectively no mass dependence of He diffusivity, or perhaps slightly higher  $^4\text{He}$  diffusivity, indicates that most diffusion theories may not appropriately describe the He outgassing process in detail. For example, the process of He diffusion might be controlled by the thermally activated diffusion of lattice defects, which would have no dependence on the mass of the diffusant.

At present the conclusion that proton-induced  $^3\text{He}$  and radiogenic  $^4\text{He}$  diffuse at approximately the same rate has only been quantitatively established for Durango apatite. Further experiments are required to establish the generality of this conclusion and should enable a more detailed understanding of solid state He diffusion to be developed. It is important to recognize that the method for determining  $^4\text{He}$  spatial distributions presented by Shuster and Farley (2003) does not require that the diffusivities of each isotope are equivalent, so long as they are quantitatively relatable.

### *5.3 Effects of proton irradiation on He diffusivity*

Our experiments clearly demonstrate that for the fluence we used, proton irradiation does not modify  $^4\text{He}$  diffusion kinetics. This is shown by identical  $^4\text{He}$  diffusivity of irradiated and un-irradiated apatite and titanite. Our observations only apply to the dosage and minerals we investigated; experiments on additional minerals at higher fluences could conceivably yield different results.

Previous efforts involving nuclear irradiation followed by noble gas diffusion have underscored the need to evaluate the role of lattice damage in modifying release behavior [64-67]. Horn et al. [65] concluded that for a fast neutron fluence  $< 2 \times 10^{18}$  n/cm<sup>2</sup>, nuclear reaction-induced radiation damage to mineral lattices insignificantly affects Ar diffusion. Reactor fast neutrons produce much more lattice damage than 147 MeV protons, but even if we assume that lattice damage caused by incident protons will equivalently scale with fluence, we expect negligible damage to be associated with the irradiations in this study ( $2 \times 10^{14}$  to  $5 \times 10^{14}$  p/cm<sup>2</sup>). While fast neutrons lose essentially all their energy by inelastic scattering with almost every collision producing a lattice dislocation, the 147 MeV protons lose energy primarily by electronic stopping (ionizing collisions with electrons with no resulting lattice damage). About 25% of 147 MeV protons initiate nuclear spallation reactions, which probably do cause lattice dislocations, but these events are spread out over many centimeters of path length. Assuming that He diffusion would be primarily affected by point defects resulting from nuclear reactions we expect radiation damage diffusion enhancements to be negligible [68].

#### *5.4 Identifying multiple diffusion domains*

The introduction of proton-induced <sup>3</sup>He enables us to identify distinct domains that are either so small or lacking retentivity that all or most of the natural <sup>4</sup>He is lost prior to analysis. The use of proton-induced <sup>3</sup>He is thus highly

sensitive for “observing” these domains. This sensitivity may account for the excess  $^3\text{He}$  detected in the initial steps of the apatite and titanite experiments. For instance, we can model the observed Durango apatite  $^3\text{He}$  and  $^4\text{He}$  excess as being derived from 0.5 volume % of  $\sim 0.5\ \mu\text{m}$  chips adhering to the  $160\ \mu\text{m}$  shard surfaces. For the  $^3\text{He}$  excess, the shards need not be of apatite; any material adhering to the grains, i.e., dust, plastic fragments, etc, might host spallogenic  $^3\text{He}$ . The origin of this excess He is not yet completely understood but surface contamination is the leading candidate.

FCT titanite presents a more complex example. The analyzed aliquot was a mixture of grain sizes spanning 75 to 220  $\mu\text{m}$ . We observed excess helium in the initial steps for both  $^3\text{He}$  and  $^4\text{He}$  (Fig. 2b), although each amounts to a negligible yet different fraction of the total ( $\sim 1\%$  and  $0.5\%$  respectively). Assuming no  $^3\text{He}$  was lost prior to analysis, and if both the  $^3\text{He}$  and  $^4\text{He}$  measured in these steps is predominantly derived from less retentive domains, the results are consistent with  $\sim 50\%$  diffusive and  $\alpha$ -ejection  $^4\text{He}$  loss from those domains. If we make a simplistic assumption that *only* two domains are present and we estimate a function  $D(T)/a^2$  for the low retention domain (by regressing a line solely through the initial “excess”  $^3\text{He}$  results), we find that the 50% discrepancy is roughly consistent with diffusive  $^4\text{He}$  loss at ambient temperatures ( $\sim 20\ ^\circ\text{C}$ ) over the age of the sample,  $\sim 28$  Myrs.

In these examples, more careful size sorting, coupled with more careful cleaning of surfaces to eliminate adhering matter, could potentially remove the less retentive domains. When sorting is not possible, proton-induced  $^3\text{He}$  may be used to quantify the mass fraction of small or low retentivity domains that have lost  $^4\text{He}$  in the geologic setting. If these domains existed in nature, this

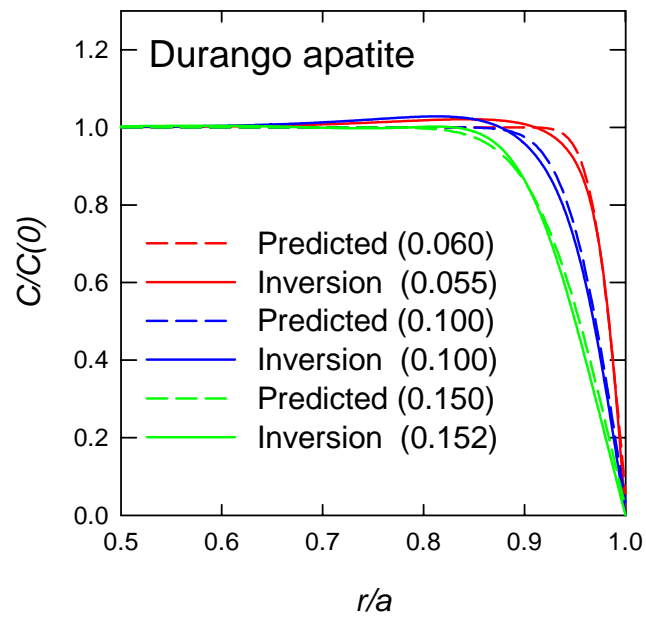


Figure 4. Radial concentration profiles. Shown are the  $^4\text{He}$  concentration  $C$  (normalized to the concentration at the center of the domain,  $C(0)$ ) at the radial position  $r$  (normalized to domain radius,  $a$ ) within the spherical domain. Solid lines were calculated by inverting Durango apatite data using [49] and as discussed in the text. Dashed lines are the predicted profiles based on isothermal outgassing assuming initially uniform  $^4\text{He}$  and spherical geometry. The numbers indicate deficit gas fractions calculated by integrating the profiles.

knowledge could be used to correct ages for “missing” radiogenic  $^4\text{He}$  that would have resided in those domains had they been quantitatively retentive. This approach may be important for determining absolute ages of samples having a distribution of domains such as polycrystalline materials [45].

### 5.5 $^4\text{He}$ profile inversion

We previously proposed a linear inversion technique to obtain  $^4\text{He}$  concentration profiles from step heating of a proton-irradiated sample with a uniform  $^3\text{He}$  distribution [49]. In such an experiment  $^3\text{He}$  allows computation of He diffusivity, while  $^4\text{He}$  release is controlled by both diffusivity and by the sought after concentration profile. An important test of the inverse calculation is to determine the accuracy of a  $^4\text{He}$  distribution derived from measurements containing analytical errors. We previously simulated such a test [49] and demonstrated the need for a regularization method (ridge regression) to filter the influence of measurement errors. Here we apply this technique to measured data.

We would like to verify the inversion result by analyzing a sample in which the initial  $^4\text{He}$  profile  $C_0(x)$  is known. Here we use our Durango apatite experiment for this purpose. Because the  $^4\text{He}$  distribution is initially uniform in this material, we know the  $^4\text{He}$  distribution at every step of the experiment [24, 49]. We thus use the early steps of a stepwise outgassing experiment to diffusively evolve the initially square profile to a series of progressively more rounded profiles, then examine whether we can recover these known profiles.

Using the complete Durango apatite dataset shown in Fig. 3, we considered three cases: 0.06, 0.10, and 0.15 *deficit gas fractions* of  $^4\text{He}$  removed by diffusion. We define the *deficit gas fraction* as  $(N_{uniform} - N_o)/N_{uniform}$  [49]. This quantity compares the total amount of diffusant in a rounded profile ( $N_o$ ) with the amount in a uniform profile ( $N_{uniform}$ ) with concentration equivalent to that of a quantitatively retentive material. For each calculation we identified the step number at which the desired cumulative  $^4\text{He}$  gas fraction ( $\Sigma F_i^{4He}$ ) had been removed, then recalculated the release fractions  $F_i^*$  as if that fraction had been removed prior to the experiment. For instance, after 6% was removed, we renormalized the subsequent  $^4\text{He}$  release fractions to 0.94. With the new set of  $F_i^*$ , and the original set of diffusion coefficients (determined from  $^3\text{He}$ ), we performed the inverse calculation.

We inverted for the profiles shown using the diffusivities implied by  $^3\text{He}$  release at each step, rather than from a best fit function  $D(T)/a^2$  over the entire experiment, and assumed  $^3\text{He}$  and  $^4\text{He}$  diffusivity to be equivalent. Although  $D(T)/a^2$  determined from an Arrhenius plot (e.g., Fig. 2) adequately describes He diffusion kinetics for many applications, there are several reasons why diffusivities implied by  $^3\text{He}$  release at each step should be used for this computation. Only the values  $\tau_i$  (where  $\tau = D(T)t/a^2$ , and  $\tau_i = \sum \tau(T_i, t_i)$ ; see equation (3) in [49]) for each step in the outgassing experiment are actually required, so there is no need for temperature extrapolation or interpolation. Using the values at each

step is preferred since they are most closely related to  $^3\text{He}$  observations and are unaffected by uncertainty in the temperature  $T_i$  of each step. Additionally, the ridge regression is not designed to regularize systematic errors in the design matrix that may be introduced by using an Arrhenius regression. The design matrix relates measured remaining fractions to the initial concentration profile (see equation (5) in [49]), and incorporates two exponential functions of activation energy  $E_a$ , i.e., the slope of the Arrhenius plot. This makes the design matrix, and hence the solution, highly sensitive to inaccuracies in  $E_a$ . An additional advantage to using  $\ln(D/a^2)$  values rather than a regressed function  $D(T)/a^2$  is the complete lack of dependence upon the temperature of each step. This may be particularly advantageous if working with phases (e.g., garnet) that require extraction temperatures unattainable using the methods of [69] ( $> 600$  °C) and lower than those easily calibrated using optical pyrometry ( $< 1000$  °C). Extraction steps in this temperature range could be used for a profile inversion even if not used to determine  $D(T)/a^2$ . However, direct use of  $\ln(D/a^2)$  values eliminates the statistical advantage of determining diffusion coefficients by least squares regression.

To minimize the propagation of analytical uncertainties into the resulting profile each of the inversions was regularized according to its analytical error [49] by identifying a characteristic break in slope in a plot of  $|\mathbf{u}_i^T \mathbf{f}|$  vs. singular value

index  $i$  (see Fig. 4c in [49] as an example). In these inversions, the indices at which errors dominated the solution were easily recognized.

The three inversions are presented in Fig. 4. Note that the ordinate extends from 0.5 to 1.0, and that all curves converge to  $C/C(0) = 1.0$  for values of  $r/a < 0.5$ . We used  $D/a^2$  values calculated for each step. We find good agreement between the shapes of each inversion and the predicted profiles. We also find good agreement in the integrated gas contents. By comparison with the expected profiles, the inversions in Fig. 4 roughly indicate the uncertainties expected for profiles derived by this approach. The inverse calculations estimate the shape of each  $^4\text{He}$  distribution and deficit gas fraction reasonably well. The worst match (the 6% deficit gas fraction inversion) was off by only  $\sim 0.5\%$  (0.055 vs. 0.060). The other two profiles agree in deficit gas fraction extremely well. We did observe a systematic “overshoot” in each of the profiles with  $C/C(0)$  values slightly  $> 1.0$  for  $r/a \sim 0.8$ ; it is unclear if this is a general artifact associated with the calculation. Note that because the Durango apatite contains a discontinuous  $^4\text{He}$  concentration profile at  $r/a = 1.0$ , we do not include the 0% deficit gas fraction inversion [49].

### 5.6 The spherical model

The representation of a He distribution within a spherical diffusion domain is an analytically tractable model that clearly does not apply perfectly in nature. An important question for our technique is how this imperfect

assumption affects the results. Using stepwise release data for a uniformly distributed gas ( $^3\text{He}$ ), the formulation of [24] produces diffusivities  $D/a^2$  corresponding to a model spherical domain of radius  $a$  with a surface area to volume ratio approximating that of the actual domain. This model yields self-consistent results even when non-spherical geometries are used, provided He diffusion is crystallographically isotropic. The latter has been shown to be true in the case of apatite [4], but has not been established for other minerals.

In the case of Durango apatite, grains are angular shards, not spheres [4], so the Durango experiment provides a good test of this supposition. The He distribution within the shards following diffusive loss will be a complicated function controlled by three-dimensional shard geometry. For instance thin slab-like features with locally high surface/volume ratio should be stripped of He more efficiently than spherical features. Nevertheless, the Fechtig and Kalbitzer [24] calculation produces  $\ln(D/a^2)$  values that are linear when plotted vs.  $1/T$  and can be used to describe the  $^4\text{He}$  distribution following diffusive loss. The calculation effectively averages over the geometrically complicated nature of the material and returns a diffusion domain radius,  $a$  (i.e.,  $\ln(D/a^2)$ ), which on the average describes the characteristic diffusion length scale of the material.

Figs. 2a and 4 illustrate the self-consistency of this example. Using the calculated  $\ln(D/a^2)$  values, the inversions recover the expected profiles after diffusive rounding despite the fact that these profiles *cannot* be simple radially symmetric spheres. This is a significant result in that it indicates that the spherical

model can be used to describe a natural  $^4\text{He}$  distribution. As we showed previously [49], as long as the domain geometry and diffusion coefficients are self-consistently applied, the profiles obtained by inversion or forward model matching can be used to constrain a sample's low-temperature cooling trajectory in nature even if the sample is not spherical.

### *5.7 Original domain surfaces*

Unlike a standard He diffusion experiment [4, 5, 53], it is critically important that a He profiling experiment be performed on diffusion domain(s) with original, intact surfaces. Most of the  $t$ - $T$  information contained within a concentration profile is located toward the domain's outer edge [49]. If individual crystals or grains define the diffusion domain(s) of a sample, broken fragments and/or missing surfaces would result in incorrect results. In samples with a naturally rounded distribution, broken surfaces would cause erroneously elevated  $^4\text{He}$  release in the initial steps of an experiment and would invert to a more square profile than actually exists.

### *5.8 Future directions*

Given the spallation  $^3\text{He}$  yields listed in Table 1, we can produce a high quality ratio evolution diagram from as little as  $\sim 250\ \mu\text{g}$  of irradiated material. However, single crystals of relevant minerals, e.g., apatite, titanite, and zircon, typically weigh just a few  $\mu\text{g}$ ; at present we must analyze crystal aggregates.

Proton induced  $^3\text{He}$  production drops off at energies below  $\sim 30$  MeV, and only modestly increases above 150 MeV [50], so changing the energy of the protons will not yield much more  $^3\text{He}$ . Increasing the proton fluence through longer or more intense irradiation is the obvious way to increase  $^3\text{He}$  yield. Based on the  $^3\text{He}$  yields and the detection limit in our laboratory, a tenfold increase in fluence should permit single crystal experiments. This ability should permit new applications for He isotope geochemistry [49].

## 6. Conclusions

We have shown that a uniform  $^3\text{He}$  distribution can be artificially produced within minerals by irradiation with a 150 MeV proton beam. We demonstrated that the outgassing of spallation  $^3\text{He}$  can be used as a proxy for radiogenic  $^4\text{He}$  diffusion. Proton-induced  $^3\text{He}$  can therefore be used for determining natural He distributions and for the applications described by Shuster and Farley (2004). We demonstrated that the concentration profile inversion technique [49] successfully recovers relatively simple profiles using release fractions containing typical measurement errors. The highly desirable ability to perform single-crystal analyses will require at least a tenfold increase in the artificial  $^3\text{He}$  abundance, which should be attainable.

**Acknowledgements.** We thank T. Schneider, S. Mukhopadhyay, and E. Schauble for helpful input, L. Hedges for sample preparation and E. Cascio for

his expertise with the irradiation and two anonymous reviewers. This work was supported by the National Science Foundation and by an N.S.F. Graduate Research Fellowship to D.L.S.

*Chapter 3*WEATHERING GEOCHRONOLOGY BY (U-TH)/HE DATING OF  
GOETHITE

D. L. Shuster

P. M. Vasconcelos

J. A. Heim

K. A. Farley

(This chapter was reprinted from *Geochimica et Cosmochimica Acta* (2005), 69(3), 659-673)

**Abstract** - Nine samples of supergene goethite (FeOOH) from Brazil and Australia were selected to test the suitability of this mineral for (U-Th)/He dating. Measured He ages ranged from 61 to 8 Ma and were reproducible to better than a few percent despite very large variations in [U] and [Th]. In all samples with internal stratigraphy or independent age constraints, the He ages corroborated the expected relationships. These data demonstrate that internally consistent He ages can be obtained on goethite, but do not prove quantitative  $^4\text{He}$  retention. To assess possible diffusive  $^4\text{He}$  loss, stepped-heating experiments were performed

on two goethite samples that were subjected to proton irradiation to produce a homogeneous distribution of spallogenic  $^3\text{He}$ . The  $^3\text{He}$  release pattern indicates the presence of at least two diffusion domains, one with high helium retentivity and the other with very low retentivity at Earth surface conditions. The low retentivity domain, which accounts for  $\sim 5\%$  of  $^3\text{He}$ , contains no natural  $^4\text{He}$  and may represent poorly crystalline or intergranular material that has lost all radiogenic  $^4\text{He}$  by diffusion in nature. Diffusive loss of  $^3\text{He}$  from the high retentivity domain is independent of the macroscopic dimensions of the analyzed polycrystalline aggregate, so probably represents diffusion from individual micrometer-sized goethite crystals. The  $^4\text{He}/^3\text{He}$  evolution during the incremental heating experiments shows that the high retentivity domain has retained 90-95% of its radiogenic helium. This degree of retentivity is in excellent agreement with that independently predicted from the helium diffusion coefficients extrapolated to Earth surface temperature and held for the appropriate duration. Considering both the high and low retentivity domains, these data indicate that one of the samples retained 90% of its radiogenic  $^4\text{He}$  over 47.5 Ma and the other retained 86% over 12.3 Ma. Thus while diffusive-loss corrections to supergene goethite He ages are required, these initial results indicate that the corrections are not extremely large and can be rigorously quantified using the proton-irradiation  $^4\text{He}/^3\text{He}$  method.

## 1. Introduction

Weathering profiles provide a record of chemical and physical processes occurring at the surface of terrestrial planets. Their mineralogical and geochemical compositions record information on the composition and abundance of weathering solutions, and their depth and complexity provide insight into the longevity of their development and the role that climate and biological processes have in enhancing weathering processes. The global distribution of weathering profiles reflects rainfall and temperature gradients across the planet. The profiles also reflect the balance between chemical-physical weathering and chemical-physical erosion, providing insight into landscape evolution and global geochemical cycles.

The thermodynamic stability and slow dissolution kinetics of many supergene minerals found in weathering profiles favors their preservation under Earth surface conditions, making them useful recorders of paleoenvironmental conditions. Because deeply weathered profiles occur on most continents and appear to have formed over a wide range of geologic times, they potentially represent a powerful record of continental paleoenvironments. Savin and Epstein (1970) first proposed the combined use of O and H isotope systematics in weathering minerals to reconstruct continental paleoclimates. Experimentally determined O and H isotopic fractionation factors have been widely applied to quantify paleotemperatures during goethite and kaolinite precipitation [70-77]. Yapp (2000) demonstrated that supergene goethite ( $\text{FeOOH}$ ) can behave as a

closed system with respect to O and H exchange for at least ~50 Myr. Despite the wealth of information recorded in weathering profiles, their usefulness as paleoclimatic and paleoenvironmental indicators is limited by the paucity of information on their timing and rate of formation.

An understanding of weathering profile evolution and derivation of paleoclimatic information from these potential archives requires quantitative knowledge of the timing of specific weathering reactions and measurements of the rate of propagation of weathering fronts. Advances have recently been made in these areas [78-81]. In young weathering profiles (< 1Ma), weathering geochronology by U-Th decay series dating of pedogenic carbonate and silica minerals provides reliable information on timing of mineral precipitation [82]. In older weathering profiles hosting supergene K-bearing minerals, weathering geochronology by the K-Ar and  $^{40}\text{Ar}/^{39}\text{Ar}$  methods are useful. Vasconcelos et al. (1994a,b), Dammer et al. (1996, 1999), Ruffet et al. (1996), Hénocque et al. (1998), Hautmann and Lippolt (2000) applied  $^{40}\text{Ar}/^{39}\text{Ar}$  dating to K-bearing Mn-oxides (cryptomelane) and sulphates (alunite-jarosite) from profiles in South America, Africa, Australia, and Europe. Precipitation ages ranging from ~70 Ma to modern suggest that some continental weathering profiles have been continuously exposed at least since the Cretaceous. Dequincey et al. (2002) measured major and trace element abundances and  $^{238}\text{U}$ - $^{234}\text{U}$ - $^{230}\text{Th}$  activity ratios in bulk rock samples from a 15 m thick African lateritic profile. They found evidence of recent U mobility throughout the laterite, possibly initiated by a late

Pleistocene climatic shift, and suggested two episodes of laterite formation. In situ-produced cosmogenic nuclides have also been used to constrain the mechanisms of weathering profile development [80, 83, 84]. Braucher et al. (2000) interpreted homogeneous  $^{10}\text{Be}$  and  $^{26}\text{Al}$  concentrations in quartz in the uppermost  $\sim 2$  m and an exponential decrease in the lower  $\sim 8$  meters of a 10 meter lateritic soil profile to indicate bioturbation of the surface layer. Small et al. (2001) and Riebe et al. (2003) used the accumulation of  $^{10}\text{Be}$  and  $^{26}\text{Al}$ , combined with mass balance calculations, to infer rates of regolith production.

Lateritic weathering profiles, often more than 400 m thick, host a plethora of supergene iron minerals distributed from the surface (in loose pisoliths and ferruginous duricrusts), through the mottled zone, and down into the saprolite and the weathering-bedrock interface. These lateritic profiles are texturally and geochemically complex and it is difficult to distinguish between relict features and those resulting from ongoing processes. A variety of geochemical and petrological tools have been employed to characterize the superimposed horizons (ferricrete, mottled zone, saprolite, etc.) common to complete lateritic weathering profiles (e.g., [85]). In detail, these studies reveal that lateritic profiles represent the result of successive and ongoing geochemical, geomorphological, and biological processes. The great depth and complexity of lateritic weathering profiles, combined with the abundance of supergene iron minerals throughout the profile, suggest that the development of a methodology suitable for dating supergene iron oxides and hydroxides may significantly

improve our understanding of the paleoclimatic and environmental conditions controlling continental weathering.

Because weathering products usually precipitate and reside at near-surface temperatures, and because such conditions are favorable for slow helium diffusion, we have investigated whether radiogenic helium is quantitatively retained in supergene goethite. If  $^4\text{He}$ , U, and Th are immobile in a mineral produced via weathering, the (U-Th)/He age represents the time since its precipitation. Due to its rapid radiogenic evolution, the (U-Th)/He system offers potential to date, to high resolution, a variety of supergene minerals that contain even trace amounts of U and/or Th over a range of timescales ( $\sim 0.5$  Ma to  $\sim 100$ s of Ma).

The application of (U-Th)/He dating to Fe-oxides is not a new idea, but it has recently come under renewed study. Strutt in 1910 reported the first He age measured on a limonite ( $\sim 2\text{Fe}_2\text{O}_3 \cdot 3\text{H}_2\text{O}$ ;  $\sim 140$  Ma). More recently, Lippolt and others reported a dozen He ages on hydrothermal and supergene goethites ( $\text{FeOOH}$ ), limonites [86], and hydrothermal hematites ( $\text{Fe}_2\text{O}_3$ ) [87-91] from central Europe. The reported hematite He ages are as young as  $\sim 5$  Ma and as old as  $\sim 180$  Ma. Helium-4 diffusion experiments [87, 89], comparisons with coexisting adularia and biotite K/Ar ages, and tests for internal consistency [91] all indicate that geologically significant He ages can be determined on certain samples of hydrothermal hematite. The goethite He ages determined by Lippolt

et al. (1998) span from  $\sim 0.8$  Ma to  $\sim 130$  Ma, qualitatively indicating helium retention over geologic timescales. They concluded that (U-Th)/He dating of goethite is potentially useful for dating very young crustal movements. However, a quantitative description of helium diffusivity in these materials at Earth surface conditions is required to establish the significance of these ages.

In this work, we evaluated the helium retentivity of polycrystalline aggregates of supergene goethite ( $\text{FeOOH}$ ). We chose goethite due to its ubiquity, because it often contains high uranium concentrations in the weathering environment [92], and because U in goethite may occupy well-defined crystallographic sites [93]. Our approach was both empirical and experimental. The empirical approach tested He age reproducibility and U and Th concentration homogeneity on multiple aliquots of individual samples. We also compared Fe-oxide He ages with cryptomelane  $^{40}\text{Ar}/^{39}\text{Ar}$  ages from the same weathering profiles, one directly associated goethite/cryptomelane pair, and from regionally associated samples. The experimental approach involved vacuum diffusion experiments on proton-irradiated polycrystalline goethite to determine the temperature dependence of helium diffusivity, from which we were able to characterize  $^4\text{He}$  retentivity at Earth surface temperatures. We conducted stepwise degassing experiments in which we measured both the natural radiogenic  $^4\text{He}$  and the spallogenic  $^3\text{He}$  induced by proton bombardment [14, 49].

## 2. Samples

For this study, we selected goethite based on several criteria: (1) in most cases, they were precipitated directly from weathering solutions into cavities created by the dissolution of primary sulfides or carbonates; (2) they exhibited botryoidal growth habits recording relative timing of mineral precipitation; (3) they were pure and devoid of primary contaminants; (4) they were composed of aggregated goethite crystallites ( $< 1 \mu\text{m}$ ); (5) they were associated with other datable supergene phases (i.e., cryptomelane), and their relative timing of precipitation could be determined based on textural relationships. Efforts were made to ensure that aliquots of each sample were from a single generation of goethite. Two samples were then selected for detailed stepwise degassing diffusion experiments. We briefly describe the nine goethite samples below.

The four Bahia goethites (BAH-F124-111.2, 114, 118, and 123) are vitreous, botryoidal, of high purity, and precipitated from solution into empty cavities, which based on their morphology are known to have been created during the dissolution of primary pyrite, chalcopyrite, and calcite (Fig. 1). Because these samples precipitated from solution, they are unlikely to have contained detrital grains of unweathered  $^4\text{He}$  bearing phases. The four samples were collected from a drill core from the weathering profile associated with the Igarapé Bahia Cu-Au deposit, Carajás, Brazil, from a drill-hole depth of  $\sim 110\text{-}120$  meters, equivalent to a vertical depth of ca. 80 m below the present surface; they precipitated and subsequently resided at-depth throughout their existence.

Multiple aliquots of samples 111.2 and 114 were prepared for He age reproducibility tests. Small pieces of the goethite bands were broken off, and then further divided into aliquots for multiple analyses. For instance BAH-F124-114-(a) is a ~10 mg piece of the BAH-F124-114 goethite growth band and BAH-F124-114-(a)-1 is one of the nine sub-aliquots prepared for analysis from that piece. Likewise BAH-F124-114-(b) is another piece sampled from the same growth band. We expect that each aliquot has approximately the same precipitation age. Figure 1b shows that the crystallites are approximately 0.5  $\mu\text{m}$  in their minimum dimension.

The MI-2000-09 sample comes from a gossan at the Lake Moondarra Cu-prospect in the Mount Isa region, NE Australia. The sample is also associated with cavities formed in a quartz vein by the dissolution of primary sulfides and carbonates during weathering reactions. These cavities often contain iron and manganese oxides and hydroxides. Several cryptomelane samples from a nearby outcrop and another outcrop in the same area have been previously dated by the  $^{40}\text{Ar}/^{39}\text{Ar}$  method [94].

Sample B01-009 is a 15 cm hand specimen from the N4E iron mine in Carajás, Brazil. The sample is from the surface “*canga*,” or lateritic iron ore associated with weathering of the Carajás banded iron formation. We analyzed four sub-samples of B01-009 (labeled a,c,e,g) that were texturally identified as four distinct generations of goethite present in the sample. Paragenetic

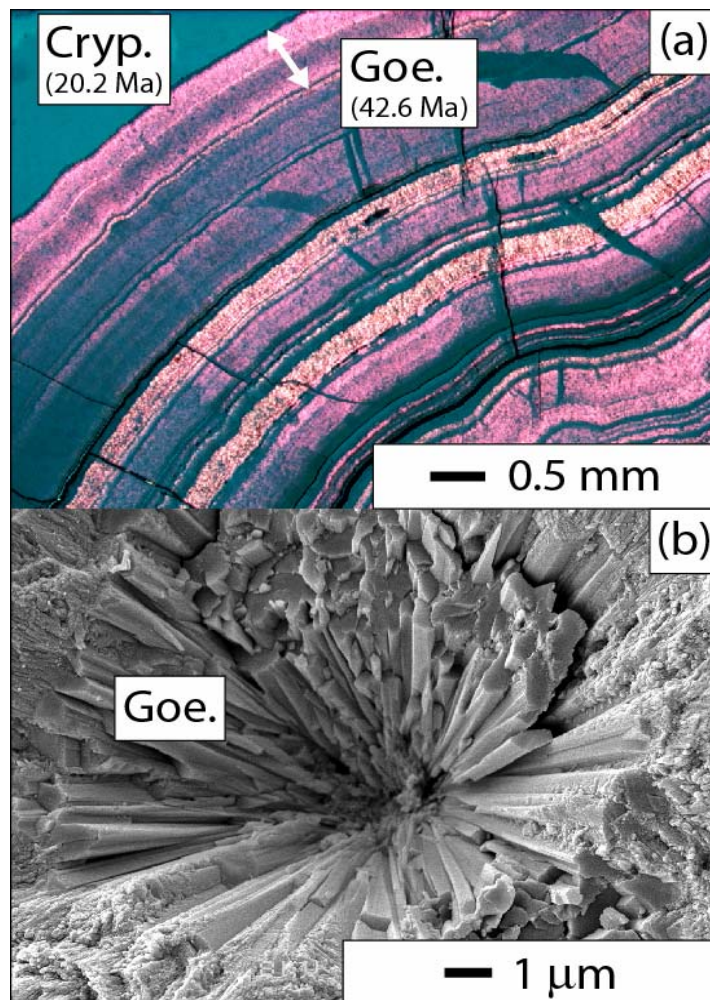


Figure 1. Microscopy. (a) Combined reflected and transmitted light image of alternating bands of botryoidal goethite (dark red, translucent) and cryptomelane (gray, opaque) for sample BAH-F124-111.2. Each band records a distinct period of mineral precipitation from solution. Dating each band separately provides a stratigraphic test for the reliability of the (U-Th)/He ages obtained. Also shown is the raw He age (42.6 Ma) of the goethite growth band approximately indicated by the white arrow, and the  $^{40}\text{Ar}/^{39}\text{Ar}$  age (20.2 Ma) of the directly adjacent massive cryptomelane overgrowth. (b) Scanning electron microscopy (SEM) image of radial goethite crystals of sample BAH-F124-114

precipitated into empty cavities in the Igarapé Bahia weathering profile. The bladed goethite crystals with minimum dimension  $\sim 0.5 \mu\text{m}$  probably represent the high retentivity sites while the intergranular space represents the low retentivity sites. The finely crystalline material along the borders represents nucleation sites for a new generation of bladed crystals.

relationships expressed in the hand sample suggest precipitation ages decrease in the order a,c,e,g.

### 3. Methods

#### 3.1 *He dating*

Using isotope-dilution mass spectrometry, we measured both [ $^4\text{He}$ ] (quadrupole), and [ $^{238}\text{U}$ ] and [ $^{232}\text{Th}$ ] (double-focusing ICP-MS) of individual sample aliquots. We extracted  $^4\text{He}$  from relatively larger aliquots ( $\sim 200 \mu\text{g}$ ) using a resistance furnace, and from smaller aliquots ( $\sim 5 \mu\text{g}$ ) using laser extraction. Details of the analytical techniques used for this study are described in Farley (2002) and Shuster et al. (2004) but are modified as follows.

Because the individual goethite crystals are extremely small ( $\sim 1 \mu\text{m}$ ), the analyzed chips represent aggregates of  $\sim 10^7$  individual crystals. To eliminate the effects of  $\alpha$ -ejection [41], we selected interior aliquots from millimeter-sized botryoidal clusters. We verified mineral identification and ensured sample purity using Raman spectroscopy and powder x-ray diffractometry (XRD). The

analyzed samples were greater than 99% FeOOH. Prior to analysis, we rinsed the aliquots in alcohol using sonication to remove small particulates adhered to the sample surfaces. To ensure quantitative transfer for U and Th analysis, we encapsulated the aliquots in Pt foil packets and used furnace and laser extraction temperatures of  $\sim 1150^{\circ}\text{C}$ . Following He extraction, we dissolved the Fe oxides in 200  $\mu\text{L}$  of concentrated HCl and heated for 12 hours to  $90^{\circ}\text{C}$ .  $^{230}\text{Th}$  and  $^{235}\text{U}$  spikes were added during dissolution.

For the He age calculations, we assumed (1) secular equilibrium among daughter nuclides in the  $^{238}\text{U}$  series, (2) a closed system for parents and daughters, and (3) zero initial  $^4\text{He}$  at the time of precipitation; these assumptions will be discussed below. Aliquots for furnace extraction were weighed prior to analysis to permit calculation of parent and daughter concentrations. For laser extraction, the masses of the Fe oxides were estimated by measuring the Fe concentration in solution. Because these masses are fairly uncertain, the concentrations are only approximate; however, note that calculated He ages are independent of mass.

### 3.2 *Step-heating diffusion experiments*

Details of the stepwise degassing method used in this study were described by Shuster et al. (2004). The samples were held at a known temperature ( $T$ ) for a known amount of time ( $t$ ) in a volume of approximately 300  $\text{cm}^3$  under static vacuum. Following a heating step, the accumulated  $^3\text{He}$  and  $^4\text{He}$  were measured by sector field mass spectrometry using external standard calibration.

We converted measured helium release fractions to diffusion coefficients ( $D/a^2$  where  $a$  is the diffusion domain radius) for each temperature step assuming spherical geometry [95]. The calculation assumes an initially uniform diffusant profile. This assumption may not be valid if diffusion has affected the radiogenic  $^4\text{He}$  distribution; a diffusively modified  $^4\text{He}$  profile will yield underestimates of  $D/a^2$  by this method.

To test for potential  $^4\text{He}$  losses, we bombarded our samples with  $\sim 10^{14}$  protons/cm<sup>2</sup> using a  $\sim 150$  MeV proton beam at the Harvard Cyclotron Laboratory to generate a uniform distribution of spallogenic  $^3\text{He}$ . Shuster et al. (2004) showed that proton bombardment yields a spatially uniform  $^3\text{He}$  distribution across individual crystals as large as  $\sim 180$   $\mu\text{m}$ , and that, at least for apatite and titanite, the irradiation itself does not change the  $^4\text{He}$  diffusivity. In addition, because the proton-induced  $^3\text{He}$  nuclei have approximately equal production probability from all target atoms present (Fe, Mn, O) with energies of  $\sim 1$ -10 MeV and because U-Th series  $\alpha$  particles have similar energies, we can assume that spallogenic  $^3\text{He}$  and natural radiogenic  $^4\text{He}$  atoms shared common stopping sites in diffusion domain(s) containing homogeneous U and Th [14].

The advantages of proton-bombardment diffusion experiments for studying polycrystalline weathering products are that the helium ( $^3\text{He}$ ) distribution is uniform, and all diffusion domains contain  $^3\text{He}$  at the start of stepwise degassing. Because we performed our diffusion experiments on polycrystalline aggregates, we expected a distribution of crystal sizes and potentially of diffusion

domain sizes. In the same way that  $^{39}\text{Ar}$  release fractions can be used to identify multiple diffusion domains in feldspar [96], we used the  $^3\text{He}$  release-fractions to constrain models that identify the presence and relative proportions of multiple diffusion domains within the samples *and* their function(s)  $D(T)/a^2$ . The proton bombardment technique allowed us to identify the release of  $^3\text{He}$  from diffusion domains of sufficiently low retentivity to have lost most (or all) radiogenic  $^4\text{He}$  over geologic time, but retentive enough to trap the spallogenic  $^3\text{He}$  over weeks spent at room temperature between irradiation and analysis.

The stepped-heating experiments were performed on single-chip  $\sim 10$  mg aliquots of Igarapé Bahia samples 114 and 111.2 (Fig. 1). These polycrystalline chips had radii of  $\sim 1$  mm, though the individual goethite crystals are far smaller ( $\sim 0.5$   $\mu\text{m}$ ). To investigate how chip size influences helium diffusivity, we performed a similar experiment on an aliquot of sample 114 with a radius of  $\sim 0.2$  mm.

Because phase transitions of supergene Fe-oxides occur at low temperatures [97], the diffusion experiments were performed below  $\sim 250$   $^{\circ}\text{C}$ . Although we did not determine the sample mass before and after the actual diffusion experiments, we verified the stability of the samples by thermogravimetric analysis of separate aliquots under rough vacuum using the same thermal cycles as the diffusion experiments. An abrupt,  $\sim 10\%$  decrease in mass was observed only at  $T > 250$   $^{\circ}\text{C}$ , above the maximum temperatures of the diffusion experiments.

#### 4. Helium dating - Results

The measured [ $^4\text{He}$ ], [U], and [Th] and resulting goethite He ages are listed in Tables 1 and 2. Table 1 shows replicated analyses of samples 111.2 and 114, and Table 2 summarizes all of the goethite He ages and their comparator Ar ages. We measured  $^3\text{He}/^4\text{He}$  ratios on non-irradiated aliquots of these samples to be effectively zero ( $< 2.8 \times 10^{-8}$ ), indicating only radiogenic helium.

We observed a wide range in concentrations of [ $^4\text{He}$ ], [U], and [Th]; from  $\sim 0.04$  to 23 nmol/g, 0.3 to 370 ppm, and  $< 0.01$  to 3.4 ppm, respectively. He ages range from  $\sim 61$  to  $\sim 8$  Ma. Th/U ratios are low ( $< 0.1$ ) for all goethite samples except those collected from the uppermost few meters of ferricrete from the N4E iron mine, Carajás, Brazil (B01-009 series), that have Th/U ranging from 2 to 10. The ranges in [U] and [Th] of eleven aliquots of sample 111.2 span factors of 4 and 44, respectively. We measured [ $^4\text{He}$ ] on six of these aliquots; the He ages differ by  $\sim 1.3\%$  ( $42.6 \pm 0.5$  Ma;  $n=6$ ). The [ $^4\text{He}$ ] and [U] of sample 114 span factors of 23 but the He ages vary by only 2% ( $10.7 \pm 0.2$  Ma;  $n=23$ ). The He ages of the four B01-009 aliquots (a,c,e,g) also corroborate their paragenetic relations. As expected, the aliquot identified to be the youngest gave the youngest He age (8.3 Ma) and the oldest gave the oldest He age (61 Ma).

Table 1. Replicate goethite He ages

Sample	He Age (Ma)	(+/-)	[U] (ppm)	[Th] (ppm)	[ <sup>4</sup> He] (nmol/gm)	Sample	He Age (Ma)	(+/-)	[U] (ppm)	[Th] (ppm)	[ <sup>4</sup> He] (nmol/gm)
Furnace Extraction:						Furnace Extraction:					
BAH-F124-114-(a)-1	9.65	0.11	149.53	0.05	7.85	BAH-F124-111.2-(a)-1	n.d.	n.d.	55.84	0.04	n.d.
-(a)-2	10.03	0.11	152.79	0.03	8.33	-(a)-2	n.d.	n.d.	54.08	0.08	n.d.
-(a)-3	11.67	0.12	120.30	0.00	7.63	-(a)-3	n.d.	n.d.	49.54	0.14	n.d.
-(a)-4	10.08	0.11	156.17	0.00	8.56	-(a)-4	n.d.	n.d.	64.57	0.13	n.d.
-(a)-5	9.88	0.11	154.71	0.01	8.31	-(a)-5	n.d.	n.d.	64.31	0.88	n.d.
-(a)-6	10.14	0.11	162.31	<0.01	8.95	-(a)-6	41.71	0.47	28.24	0.14	6.44
-(a)-7	9.90	0.11	155.80	<0.01	8.39	-(a)-7	41.56	0.47	59.67	0.20	13.54
-(a)-8	10.78	0.12	15.79	<0.01	0.93	<b>Mean / Std Err</b>	<b>41.64</b>	<b>0.08</b>			
-(a)-9	10.34	0.12	160.46	<0.01	9.02						
<b>Mean / Std Err</b>	<b>10.27</b>	<b>0.20</b>									
Laser Extraction:						Laser Extraction:					
BAH-F124-114-(b)-1	10.18	0.11	325.63	0.03	18.02	BAH-F124-111.2-(b)-1	41.17	0.45	77.69	0.02	17.45
-(b)-2	10.70	0.12	368.81	0.05	21.47	-(b)-2	43.24	0.48	96.97	0.05	22.88
-(b)-3	10.95	0.12	329.83	0.02	19.64	-(b)-3	43.68	0.48	103.44	0.05	24.66
-(b)-4	11.36	0.12	288.13	0.01	17.80	-(b)-4	44.36	0.49	70.29	0.02	17.02
-(b)-5	11.86	0.13	250.95	0.02	16.18	<b>Mean / Std Err</b>	<b>43.11</b>	<b>0.69</b>			
<b>Mean / Std Err</b>	<b>11.01</b>	<b>0.29</b>				<b>Grand Mean</b>	<b>42.62</b>	<b>0.53</b>			
BAH-F124-114-(c)-1	10.63	0.15	312.68	0.03	18.08						
-(c)-2	10.81	0.12	265.29	0.06	15.60						
-(c)-3	11.74	0.15	246.92	<0.01	15.77						
-(c)-4	13.89	0.12	260.23	0.03	19.67						
-(c)-5	10.17	0.10	280.50	0.01	15.51						
-(c)-6	10.26	0.13	269.60	0.03	15.05						
-(c)-7	10.69	0.13	282.26	0.02	16.41						
-(c)-8	10.79	0.13	272.72	0.02	16.00						
-(c)-9	8.97	0.12	265.23	0.02	12.93						
<b>Mean / Std Err</b>	<b>10.88</b>	<b>0.45</b>									
<b>Grand Mean</b>	<b>10.67</b>	<b>0.21</b>									

The listed He age uncertainties are <sup>1</sup> propagated from U, Th and <sup>4</sup>He analytical uncertainties and underestimate true He age uncertainties.

The U, Th and <sup>4</sup>He concentrations are approximations; calculated He ages are independent of mass. nmol is 10<sup>-9</sup> moles, "n.d." denotes not determined.

#### 4.1 Comparing He ages with Ar ages

The best way to test the accuracy of an absolute geochronometer is to compare it against an independently known mineral precipitation age. However, there are no other techniques by which to directly date these minerals. An indirect comparison between *different* weathering phases is currently the only way to test the accuracy of the goethite (U-Th)/He ages.

The Bahia goethite He ages generally agree with cryptomelane  $^{40}\text{Ar}/^{39}\text{Ar}$  ages from the same profile, which range from ~40 to 0 Ma [79]. The eight goethite He ages in Table 2 fall in approximately this same range (~61 to 8 Ma). In the case of Bahia goethite sample 111.2 (He age ~43 Ma), two nearby samples (111.8 and 112.1) containing cryptomelane overgrowth on botryoidal goethite yield  $^{40}\text{Ar}/^{39}\text{Ar}$  ages of  $13.7 \pm 0.6$  and  $13.8 \pm 0.3$  Ma, consistent with the observed paragenetic relationship. Sample 111.2 contains a generation of cryptomelane that is directly precipitated over the goethite (Fig. 1). We do not necessarily expect that these two phases share a common precipitation age; however the cryptomelane age must be younger than the age of the goethite. The radiometric ages of the cryptomelane/goethite pair are consistent with their paragenetic relationship; the goethite He age is ~43 Ma whereas the three grains of cryptomelane from that sample yield  $^{40}\text{Ar}/^{39}\text{Ar}$  plateau ages of  $19.4 \pm 0.2$  Ma,  $20.6 \pm 0.2$ ,  $19.2 \pm 0.3$ , and  $21.6 \pm 0.6$  Ma.

The He age for the Lake Moondarra sample MI-2000-09 (Table 2;  $15.61 \pm 0.18$  Ma) also agrees well with  $^{40}\text{Ar}/^{39}\text{Ar}$  ages from nearby samples (plateau ages of  $20.7 \pm 0.3$ ,  $19.7 \pm 0.1$ ,  $19.0 \pm 0.4$ ,  $16.0 \pm 1.7$ , and  $15.2 \pm 1.2$  Ma). The goethite and cryptomelane samples from the Lake Moondarra locality occur on a regionally recognized ca. 300-meter elevation weathering surface [94]. The age of supergene minerals in some of these surfaces have been locally and regionally correlated [98]. Several other samples dated for the same surface in the Mt. Isa Mines gossan, approximately 20 km away from the Lake Moondarra locality, yield cryptomelane  $^{40}\text{Ar}/^{39}\text{Ar}$  plateau ages of  $21.5 \pm 0.3$ ,  $21.2 \pm 0.5$ ,  $20.9 \pm 0.2$ ,  $20.7 \pm 0.2$ ,  $20.02 \pm 0.19$ ,  $18.0 \pm 0.3$ ,  $17.7 \pm 0.5$ ,  $16.7 \pm 0.2$ , and  $14.57 \pm 0.12$  Ma. The (U-Th)/He results obtained for the goethite sample is entirely consistent with the  $^{40}\text{Ar}/^{39}\text{Ar}$  plateau ages of cryptomelane ages from the same weathering profile. Goethite and Mn-oxides in the lake Moondarra site both reflect water-rock interaction during weathering of sulfide-carbonate hydrothermal assemblages. Once goethite and Mn-oxides precipitate, they will remain metastably preserved, particularly if after mineral precipitation the groundwater levels drop, leaving these minerals stranded in the unsaturated zone. A progressive drop of the water table is a predictable consequence of the known aridification of Australia since the Miocene.

Table 2: Comparison between He and Ar ages, stratigraphic relationships

Region:	Sample phase	Radiometric age (Ma)	(+/-)	[U] (ppm)	[Th] (ppm)	[ <sup>4</sup> He] (nmol/gm)
Bahia:						
	goethites	<i>(U-Th)/He</i>				
	BAH-F124-111.2*	42.62	0.53	-	-	-
	BAH-F124-118	30.38	0.34	29.39	<0.01	4.87
	BAH-F124-123	15.80	0.18	29.00	<0.01	2.49
	BAH-F124-114*	10.67	0.21	-	-	-
	B01-009-(a) ( <i>oldest</i> )	61.02	0.61	0.76	3.43	0.52
	B01-009-(c)	36.87	0.37	0.26	2.52	0.17
	B01-009-(e)	26.70	0.27	0.65	1.42	0.14
	B01-009-(g) ( <i>youngest</i> )	8.33	0.08	0.36	2.00	0.04
	cryptomelanes	<sup>40</sup> Ar/ <sup>39</sup> Ar				
	<i>Regional range**</i>	<i>40 to 0</i>	-	-	-	-
	BAH-F124-111.2	20.2	0.56	-	-	-
Mount Isa:						
	goethite	<i>(U-Th)/He</i>				
	MI-2000-09	15.61	0.18	4.27	0.08	0.36
	cryptomelanes	<sup>40</sup> Ar/ <sup>39</sup> Ar				
	<i>Regional range</i>	<i>14.6 to 21.5</i>	-	-	-	-

Notes: The He age uncertainties are 1- $\sigma$  propagated from U, Th and <sup>4</sup>He analytical uncertainties and underestimate true He age uncertainties. The U, Th and <sup>4</sup>He concentrations are approximations.

Also reported are <sup>40</sup>Ar/<sup>39</sup>Ar ages determined on associated cryptomelane, where applicable.

nmol is 10<sup>-9</sup> moles.

\*Average of replicate analyses (see Table 1)

\*\*Vasconcelos et al., 1994, "-" not applicable

## 5. Helium dating - Discussion

Three important results of the He dating study are that polycrystalline goethite contains (1) variable but generally ppm level concentrations of U and Th, (2) relatively high [<sup>4</sup>He], and (3) He ages that are reproducible despite significant inter-aliquot variability in [U] and [Th]. The He age reproducibility, particularly despite strong [U] and [Th] variability, indicates systematic behavior in the polycrystalline goethite that precludes significant U and Th mobility [20]. For example, uniform addition or removal of U from the goethite at some time

following precipitation would not yield isochronous He ages in aliquots with variable U concentrations.

Each of the aliquots was originally located  $\sim 250 \mu\text{m}$  from the next nearest aliquot and sampled from single massive generations of goethite. Since some samples have strongly heterogeneous U and Th concentrations between aliquots, commonality in their He ages requires that radiogenic  $^4\text{He}$  atoms have not migrated between the aliquots (distance  $\sim 125 \mu\text{m}$ ) since formation. Radiogenic helium was either quantitatively retained or  $^4\text{He}$  diffusion resulted in the loss of an identical fraction of  $^4\text{He}$  from each aliquot directly to the environment. Diffusive loss would require that  $^4\text{He}$  migrated along grain boundaries or another highly transmissive medium rather than through the crystals of the aggregate.

Corroboration of the paragenetic age relationship between the cryptomelane (younger) and goethite (older) by the He ages for sample 111.2 is also significant. Because diffusive helium loss and late stage U adsorption are processes likely to disrupt a goethite He age, and because both processes would result in an artificially young age, it is easier to reconcile systematically young He ages than old. Although the apparent  $\sim 20$  Myr hiatus between Fe-oxide and Mn-oxide precipitation is initially surprising, the precipitation timescales of coexisting phases are difficult to know *a priori*, particularly in the complicated processes of chemical weathering. The apparent  $\sim 20$  Myr hiatus between Fe-oxide and Mn-oxide precipitation is permissible, and may represent distinct weathering events in

that region.

Once incorporated into goethite, the apparent immobility of U and Th implies that the goethite aggregates are resistant to post-precipitation changes in groundwater chemistry. Dequincey et al. (2002) found evidence of recent U mobility throughout a lateritic profile in Africa by measuring U series activity ratios of homogenized whole-rock samples. Their findings indicated that a recent (0.3 Ma) chemical remobilization had occurred throughout that system. They proposed that  $^{234}\text{U}$  could have been removed from the uppermost ferruginous unit (composed primarily of hematite and goethite) and redistributed throughout the lower units of the profile. However, they also proposed that the high apparent  $^{234}\text{U}$ - $^{238}\text{U}$  fractionations indicated that U was not easily removed from the ferruginous unit and that U would have been mostly retained by Fe oxyhydroxides. Because our measurements were made on isolated goethite of high purity, it is difficult to compare the results with those of a whole-rock analysis. However, if U and Th were at any point mobilized throughout the Bahia profile, then the isochronous goethite He ages require that goethite aggregates acted as a robust closed system with respect to U and Th.

Several important questions arise regarding U and Th spatial variability within the goethite aggregates. U and Th are clearly not homogeneously distributed throughout the samples, although we do not well understand where or how U and Th are incorporated into the goethite aggregates. These parent elements are either incorporated into the goethite structure itself or adsorb onto

mineral surfaces and are subsequently trapped into the crystal aggregate by overgrowth. Uranium adsorption onto goethite is an efficient process in groundwater systems [92, 99-101], and it is possible that  $\text{UO}_2^{2+}$  adsorbs on goethite through inner-sphere surface complexes [92, 102, 103] or precipitates as minor amounts of U-phosphate, U-vanadate, or in another U-bearing supergene phase. Recent experimental investigation on uranium co-precipitation with synthetic iron oxides provides compelling evidence that U is incorporated into goethite structures and is not simply adsorbed onto mineral surfaces [93]. The more limited aqueous mobility of Th in low-temperature groundwater suggests that any significant Th concentration may reflect inheritance of Th from primary minerals. Thorium liberated during mineral dissolution would be immediately re-precipitated in situ.

Although the XRD of these samples indicated that they were high purity iron hydroxide, the possibility remains that U and Th precipitate into separate phases on a very small spatial scale. If so, then the goethite aggregate may simply act as a  $^4\text{He}$  carrier. Since U and Th decay series  $\alpha$  particles are ejected  $\sim 15 \mu\text{m}$  from their parent nuclei, it would be possible for most  $^4\text{He}$  to reside in goethite surrounding small ( $\sim \mu\text{m}$ ) autunite, tobernite, or other U/Th-bearing inclusions. This would not violate the dating technique as long as (1) the radiogenic helium is quantitatively sampled and analyzed with the parent nuclides, (2) the parent phase contemporaneously precipitated with the goethite, and (3) the parent phase does not contain inherited  $^4\text{He}$ . If goethite sufficiently retains implanted  $^4\text{He}$ , it would

be of little consequence that parent and daughter nuclides reside in separate phases. Future studies using trace element probe analysis and synchrotron-based spectroscopic techniques (XAFS, XANES, etc.) will help identify the site and speciation of parent nuclides in aggregated goethite.

A significant difference among the samples is the high Th contents of near surface samples from the N4E *camga*. Although the goethite in these samples is visually pure, it is difficult to ascertain that these iron hydroxides precipitated directly from solution in open cavities, which would less likely incorporate detrital mineral impurities. The complexity of the processes occurring in the near-surface environment, where biological processes and the possibility of contamination by detrital and aeolian components strongly dominate mineral precipitation, may account for the high Th contents in these samples.

All of our He age calculations assume secular equilibrium among U-series daughters. This is clearly an oversimplification. Ground waters have  $^{234}\text{U}/^{238}\text{U}$  activity ratios that are usually  $> 1$  [104, 105], and it is likely that goethites will precipitate with this elevated ratio. Similarly, it seems likely that the initial  $^{230}\text{Th}/^{238}\text{U}$  ratio of void-filling goethites precipitated directly from solution is  $\sim 0$ . Although initial disequilibrium will have a minor effect upon  $\sim$ several Ma He ages, the effects can be large in younger samples. Bender (1973) provides formulae for computing He ingrowth under these conditions. Excesses of  $^{234}\text{U}$  yield anomalously old ages, while deficits of  $^{230}\text{Th}$  yield anomalously young ages. For example, an initial  $^{234}\text{U}/^{238}\text{U}$  ratio of 1.1 and  $^{230}\text{Th}/^{238}\text{U}$  of zero yields an

~5% *underestimate* of age at 1 Ma, ~0.6% at 10 Ma, and ~0.05% at 100 Ma [20, 106]. Without additional knowledge of the initial state of U-series disequilibrium, the magnitudes of these effects set the minimum uncertainties to be expected for goethites of those ages. Although we can assume initial activity ratios, groundwater variability in  $^{234}\text{U}/^{238}\text{U}$  limits the ability to reliably date young goethites (< 500 ka) by the (U-Th)/He method.

## 6. Stepwise degassing experiments - Results

Results of the stepped-heating diffusion experiments are given in Table 3 and presented as Arrhenius plots ( $\ln(D/a^2)$  vs.  $10^4/T$ ) in Figs. 2 and 3 and ratio evolution diagrams in Fig. 4. The experiments were conducted on proton-irradiated aliquots of samples 114 and 111.2. Due to the natural high  $^4\text{He}$  concentrations and low  $^3\text{He}/^4\text{He}$  ratios of these samples, the proton irradiation effectively generated a purely synthetic distribution of  $^3\text{He}$  in samples containing a natural distribution of *only*  $^4\text{He}$ . Spallogenic helium produced via proton bombardment has a  $^4\text{He}/^3\text{He}$  ratio of ~10, contributing a negligible component to the  $^4\text{He}$  budget of each sample. For this reason, we can consider the experimental results of each isotope separately, as each should provide distinct information about the sample [14, 49]. We present diffusion coefficients calculated from the measured release fractions of proton-induced  $^3\text{He}$  in Fig. 2 and radiogenic  $^4\text{He}$  in Fig. 3. Due to the possibility of diffusive rounding, values of  $\ln(D/a^2)$  calculated from  $^4\text{He}$  release fractions may not accurately reflect

Table 3. Stepwise degassing results

Step	T (°C)	t (hr)	<sup>3</sup> He (x 10 <sup>6</sup> atoms)	(+/-)	<sup>4</sup> He (x 10 <sup>9</sup> atoms)	(+/-)	Step	T (°C)	t (hr)	<sup>3</sup> He (x 10 <sup>6</sup> atoms)	(+/-)	<sup>4</sup> He (x 10 <sup>9</sup> atoms)
BAH-F124-114 (11.1mg)							BAH-F124-111.2 (3.4 mg)					
1	50	5	0.29	0.02	BDL	BDL	1	50	5	0.95	0.02	BDL
2	65	5	1.20	0.03	BDL	BDL	2	65	5	2.27	0.03	BDL
3	80	4	2.50	0.03	BDL	BDL	3	80	4	2.29	0.03	BDL
4	100	2	3.93	0.04	BDL	BDL	4	100	2	1.79	0.02	0.8
5	125	2	18.14	0.09	3.2	0.0	5	125	2	3.50	0.04	3.1
6	150	1	20.18	0.09	14.1	0.1	6	150	1	2.66	0.03	8.1
7	175	1	30.47	0.13	110.8	0.1	7	175	1	3.78	0.05	40.8
8	200	1	37.21	0.13	610.8	0.1	8	200	1	4.77	0.05	263.5
9	200	1	21.55	0.10	634.5	0.1	9	200	1	2.61	0.03	285.5
10	200	1	18.83	0.10	719.8	0.1	10	200	1	2.08	0.04	319.3
11	190	1	8.97	0.06	344.4	0.1	11	190	1	0.95	0.02	150.4
12	180	2	7.51	0.05	283.6	0.1	12	180	2	0.79	0.02	112.5
13	170	3	4.42	0.04	155.0	0.0	13	170	3	0.47	0.01	64.3
14	160	3	1.77	0.03	59.1	0.0	14	160	3	0.14	0.01	21.0
15	150	4	0.82	0.02	28.5	0.0	15	150	4	0.04	0.01	9.5
16	140	5	0.30	0.02	11.5	0.0	16	140	5	0.02	0.01	3.0
17	175	4	9.75	0.05	402.7	0.1	17	175	4	0.75	0.02	128.5
18	195	3	39.40	0.15	1874.3	0.2	18	195	3	3.49	0.03	821.8
19	205	2	57.77	0.16	2932.9	0.1	19	205	2	5.31	0.04	1315.6
20	210	1	41.76	0.11	2178.4	0.1	20	210	1	4.02	0.04	960.6
21	215	1	56.92	0.16	3021.5	0.1	21	215	1	5.45	0.05	1323.5
22	220	1	71.19	0.18	3787.7	0.2	22	220	1	7.26	0.05	1747.3
23	225	1	82.69	0.19	4471.8	0.2	23	225	1	9.69	0.06	2235.2
24	230	1	91.08	0.20	4974.9	0.2	24	230	1	12.36	0.06	2787.3
25	235	1	93.48	0.19	5050.4	0.2	25	235	1	15.18	0.08	3357.0
26	240	1	95.10	0.20	5093.9	0.2	26	240	1	17.49	0.09	3926.3
27	245	1	89.31	0.19	4636.9	0.2	27	245	1	19.35	0.08	4230.9
							28	250	1	20.98	0.09	4256.7
LS	~1300	0.5	277.89	0.33	14678.0	0.4	LS	~1300	0.5	81.45	0.20	24272.6
Total			1184.4		56078.5		Total			231.9		52645.1

The stepwise <sup>3</sup>He and <sup>4</sup>He degassing results used to calculate diffusion coefficients shown in Fig. 2 for Bahia goethite samples 114 and 111.2. Uncertainties in atomic abundance are reported at the 95% confidence level. All temperatures were controlled to better than 1 °C. LS = last step, BDL = below detection limit.

diffusivity. We therefore concentrated on  $^3\text{He}$  to quantify helium diffusion coefficients and  $^4\text{He}$  to determine the degree of partial  $^4\text{He}$  retention. Note that the heating schedules of these experiments included both prograde (sequentially increasing) and retrograde (decreasing) steps.

### 6.1 *Proton-induced $^3\text{He}$ diffusion parameters*

The most apparent feature of the  $^3\text{He}$  results is a break in slope occurring at  $\sim 180$  °C that separates two distinct arrays (Fig. 2). The array of higher diffusivity was obtained from the initially derived gas, and amounts to 4% and 8% of the total  $^3\text{He}$  budgets of samples 114 and 111.2, respectively. Note that points on an Arrhenius plot are not weighted according to the amount of extracted gas. For example, although the higher diffusivity arrays have strong graphical representation, the steps cumulatively represent small proportions of the total  $^3\text{He}$  budgets.

This type of feature has been observed in other phases using both proton-induced  $^3\text{He}$  and radiogenic  $^4\text{He}$ , and suggests that multiple diffusion domains are present in the samples [5, 8, 14]. Although these data have important implications discussed further below, the arrays of lower diffusivity, representing the majority ( $> 90$  %) of the extracted  $^3\text{He}$ , better characterize helium diffusivity in the bulk of the polycrystalline samples. These arrays have strong linear correlations between  $\ln(D/a^2)$  and  $1/T$  between 145 °C and 225 °C

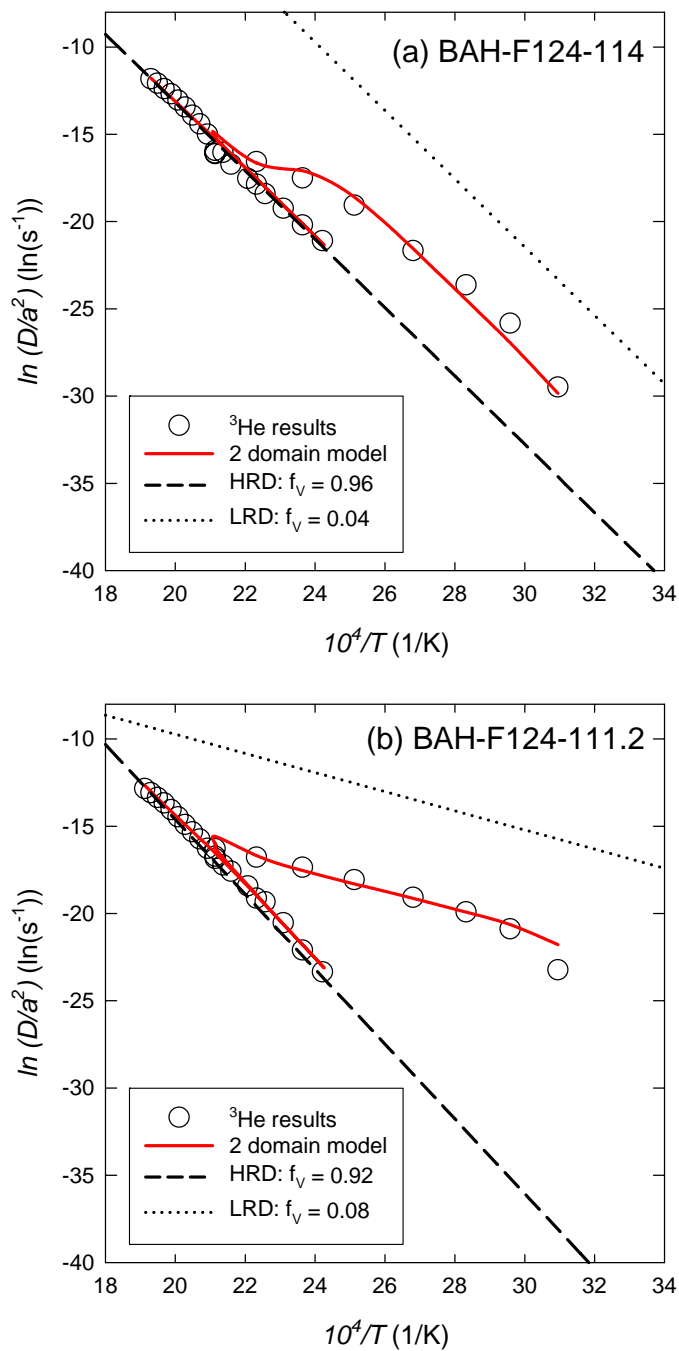


Figure 2. Helium-3 Arrhenius plots for (a) BAH-F124-114 and (b) BAH-F124-111.2.

Open circles are values calculated from release fractions of proton-induced  $^3\text{He}$

according to Fechtig and Kalbitzer (1966). The dashed lines are the least squares regressions through the HRD of each sample. The solid curves are the two-domain models used to construct the curves shown in Fig. 4 and summarized in Table 4. For reference, the dotted lines are the diffusion parameters of the LRD and  $f_V$  denotes the volume fraction of each domain used to construct the two-domain models

with correlation coefficients ( $R^2$ ) higher than 0.996 for each experiment. The correlations persist throughout retrograde temperature cycles indicating that (1) during those steps  $^3\text{He}$  is derived primarily from a single characteristic domain size, and (2) the assumed initial uniform  $^3\text{He}$  distribution is valid [14, 49]. Regressions through these data are shown as dashed lines in the Arrhenius plots (Fig. 2), and the diffusion parameters extracted from each regression are indicated in Table 2 as the *high retentivity domains* (HRD). Sample 114 results were qualitatively duplicated in a more coarsely conducted experiment (not presented) on a different aliquot of smaller physical aggregate size. In that experiment, both the overall shape of the Arrhenius plot, and the regression through the HRD were in excellent agreement with the results presented in Fig. 2.

Goethite 111.2, as defined by the array of lower diffusivities, is slightly more helium retentive than sample 114. As discussed below, the two arrays have the following diffusion parameters:  $E_a = 162.8 \pm 2.4$  kJ/mol and  $\ln(D_0/a^2) = 26 \pm 0.6$  ln(s<sup>-1</sup>); and  $E_a = 178.4 \pm 2.6$  kJ/mol and  $\ln(D_0/a^2) = 28.3 \pm 0.6$  ln(s<sup>-1</sup>), for samples 114 and 111.2, respectively. By assuming a diffusive length scale “ $a$ ” of

0.5  $\mu\text{m}$  for both samples (Fig. 1b and see *Discussion*), we can estimate the frequency factors  $D_0$  with which to compare these results to other phases commonly used for (U-Th)/He dating. We estimate the following values:  $\ln(D_0) = 6.2$  and  $\ln(D_0) = 8.5 \ln(\text{cm}^2/\text{s})$ , for samples 114 and 111.2, respectively. Durango apatite and FCT titanite each have comparable activation energies (148 and 183 kJ/mol, respectively), but lower frequency factors ( $\sim 3.4$  and  $\sim 4.1 \ln(\text{cm}^2/\text{s})$ , respectively; [4, 5]), indicating that the polycrystalline goethite is less helium retentive than these phases.

## 6.2 Radiogenic $^4\text{He}$ diffusion coefficients

Shown in Fig. 3, the diffusion coefficients calculated from  $^4\text{He}$  are initially lower than those calculated from  $^3\text{He}$  and are also significantly lower than the HRD linear regressions discussed above and shown in Fig. 2. For instance, in the 114 experiment, the early step at 100 °C yielded a value of  $D/a^2$  that is a factor of  $1.2 \times 10^{-4}$  lower than the HRD  $^3\text{He}$  based extrapolation. However, as each experiment proceeded toward higher gas yields, the apparent  $\ln(D/a^2)$  coefficients calculated from each isotope became gradually convergent. At the highest temperatures and latest steps of each experiment, the results calculated from  $^3\text{He}$  become statistically indistinguishable from  $^4\text{He}$ . These features are expected if proton-induced  $^3\text{He}$  and radiogenic  $^4\text{He}$  have equivalent diffusivity in goethite and the natural  $^4\text{He}$  distribution is diffusively modified [14, 49].

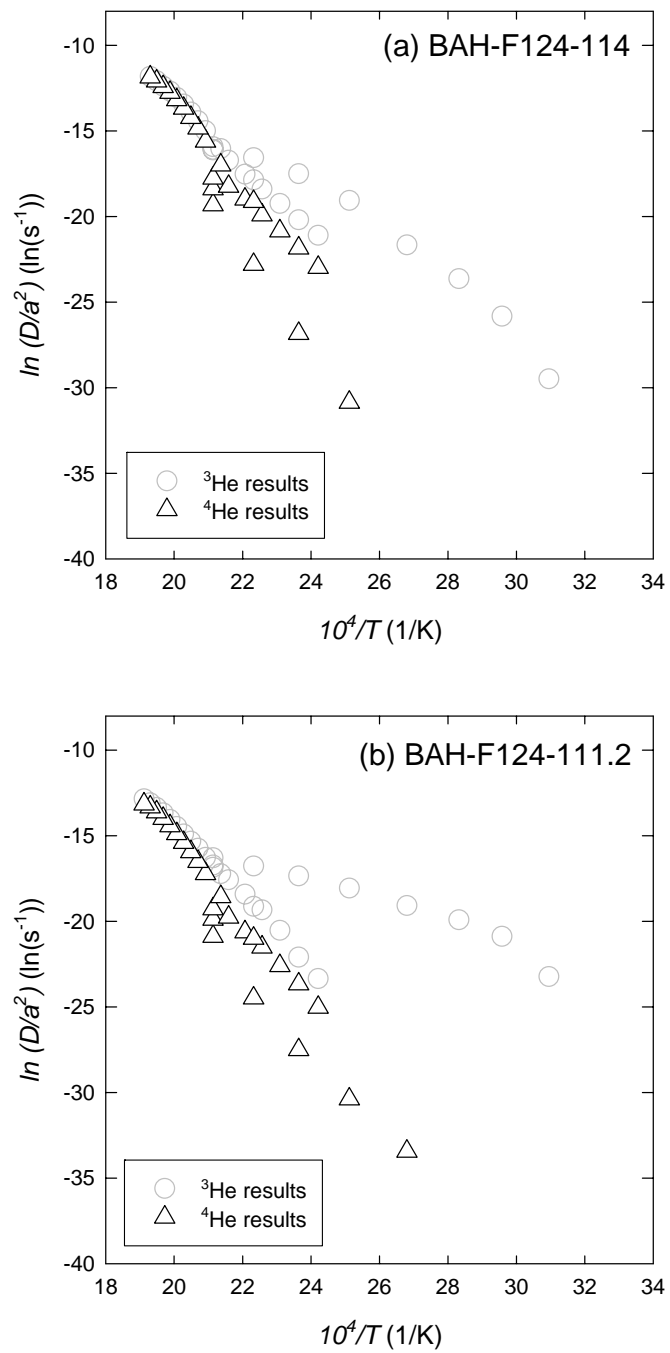


Figure 3. Helium-4 Arrhenius plots for (a) BAH-F124-114 and (b)

BAH-F124-111.2. Triangles are values calculated from release fractions of radiogenic  $^4\text{He}$  according to Fechtig and Kalbitzer (1966). Also shown for reference as open circles are the  $^3\text{He}$  determined values presented in Fig. 2.

### 6.3 Ratio evolution diagrams

A  $^4\text{He}/^3\text{He}$  ratio evolution diagram ( $R_{step}/R_{bulk}$ , where  $R = ^4\text{He}/^3\text{He}$  vs. cumulative  $^3\text{He}$  release fraction,  $\Sigma F^3\text{He}$ ) is useful for constraining the spatial distribution of  $^4\text{He}$  in proton-irradiated samples [49]. The measured ratio evolution diagrams for each experiment are shown in Fig. 4. In each experiment, the values of  $R_{step}/R_{bulk}$  are very low when  $\Sigma F^3\text{He} < 0.1$  followed by a sharp and continuous increase to values that are more consistent with the bulk  $^4\text{He}/^3\text{He}$  ratio ( $R_{step}/R_{bulk} \sim 1$ ). The increase to higher values of  $R_{step}/R_{bulk}$  occurred more gradually for sample 114 than for sample 111.2. For instance,  $R_{step}/R_{bulk}$  of sample 114 increased from  $\sim 0$  to values  $\geq 1.0$  in the range of  $\Sigma F^3\text{He}$  from 0.04 to 0.30. The same occurred abruptly for sample 111.2 in the range of  $\Sigma F^3\text{He}$  from 0.07 to 0.12. Note that the high density of values at  $\Sigma F^3\text{He} \sim 0.15$  were determined during retrograde heating cycles in each experiment.

Once each of the stepped experiments evolved to  $R_{step}/R_{bulk} \geq 1.0$ , the measured ratios remained relatively constant. However, whereas the last few steps in the sample 114 experiment continually increased, the last few steps of sample 111.2 slightly but significantly decreased from a maximum value obtained

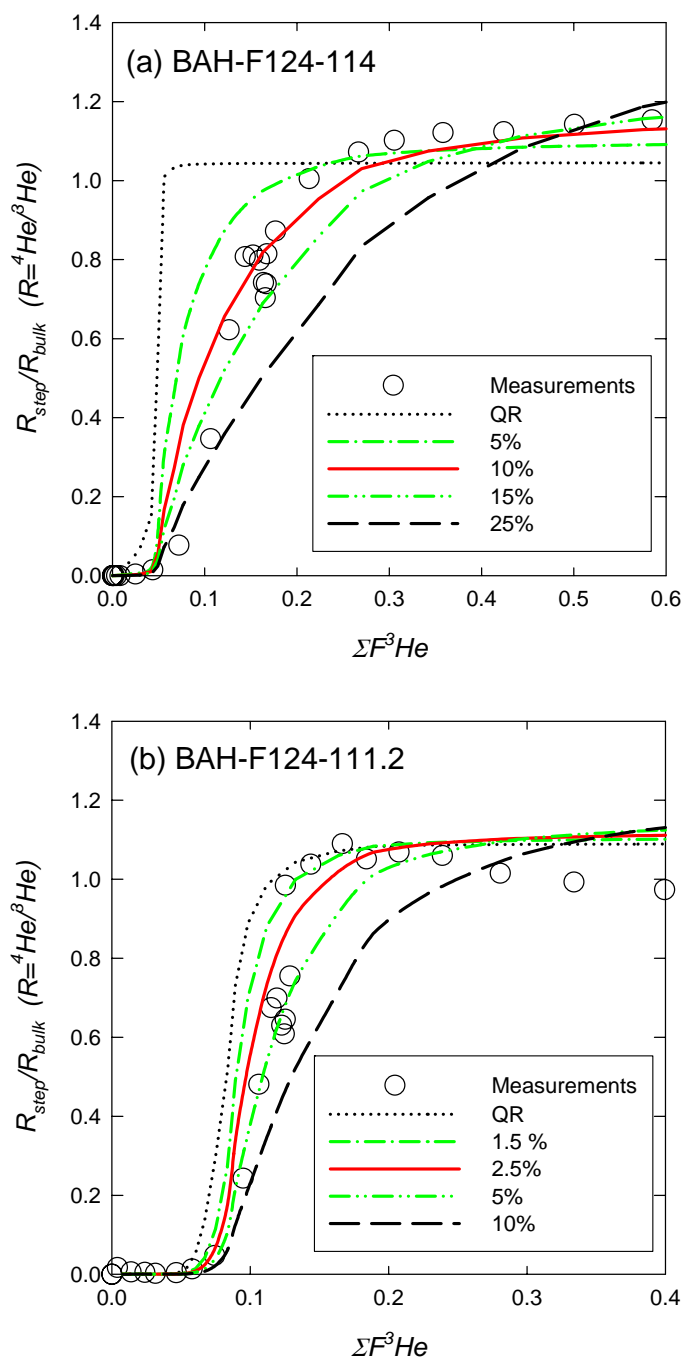


Figure 4. Goethite ratio evolution diagrams for (a) BAH-F124-114 and (b) BAH-F124-111.2. Shown are measured isotope ratios for each release step,  $R_{\text{step}}$  ( $R=^4\text{He}/^3\text{He}$ ),

normalized to the bulk ratio  $R_{bulk}$  plotted vs. the cumulative  ${}^3\text{He}$  release fraction,  $\Sigma F^3\text{He}$ . Five two-domain diffusion models are shown for each sample with deficit gas fractions of the HRD indicated in the legend. QR denotes quantitative  ${}^4\text{He}$  retention in the HRD. The analytical uncertainties of the points are of order 5% (roughly twice the diameter of the points) and are excluded from the diagram for clarity. Note that the two figures are at different scales.

when  $\Sigma F^3\text{He} \sim 0.2$ . Most of the information about a  ${}^4\text{He}$  distribution is expressed at low gas yields ( $\Sigma F^3\text{He} < 0.4$ ) of a single domain ratio evolution diagram [49]. At low yields the effects of diffusive loss are most pronounced. For this reasons we focused on the  ${}^4\text{He}/{}^3\text{He}$  ratios when  $\Sigma F^3\text{He} < 0.4$  to interpret Fig. 4.

#### 6.4 Helium retentivity

Because supergene weathering products likely have isothermal histories (precipitation and residence at low temperatures), the closure temperature ( $T_c$ ) is inappropriate for characterizing helium retentivity. Instead, we borrow a simple model of isothermal diffusive loss and radiogenic in-growth, presented by Ozisik (1989) and modified for He dating as presented in Wolf et al. (1998). For given functions of  $D(T)/a^2$ , plots of isothermal holding time ( $t$ ) versus expected He age ( $t'$ ) can be calculated to evaluate the effect of diffusive  ${}^4\text{He}$  loss upon a He age.

In Fig. 5 we present helium retention factors (curves plotted as He age/holding time ( $t'/t$ )) for three isothermal temperatures as functions of

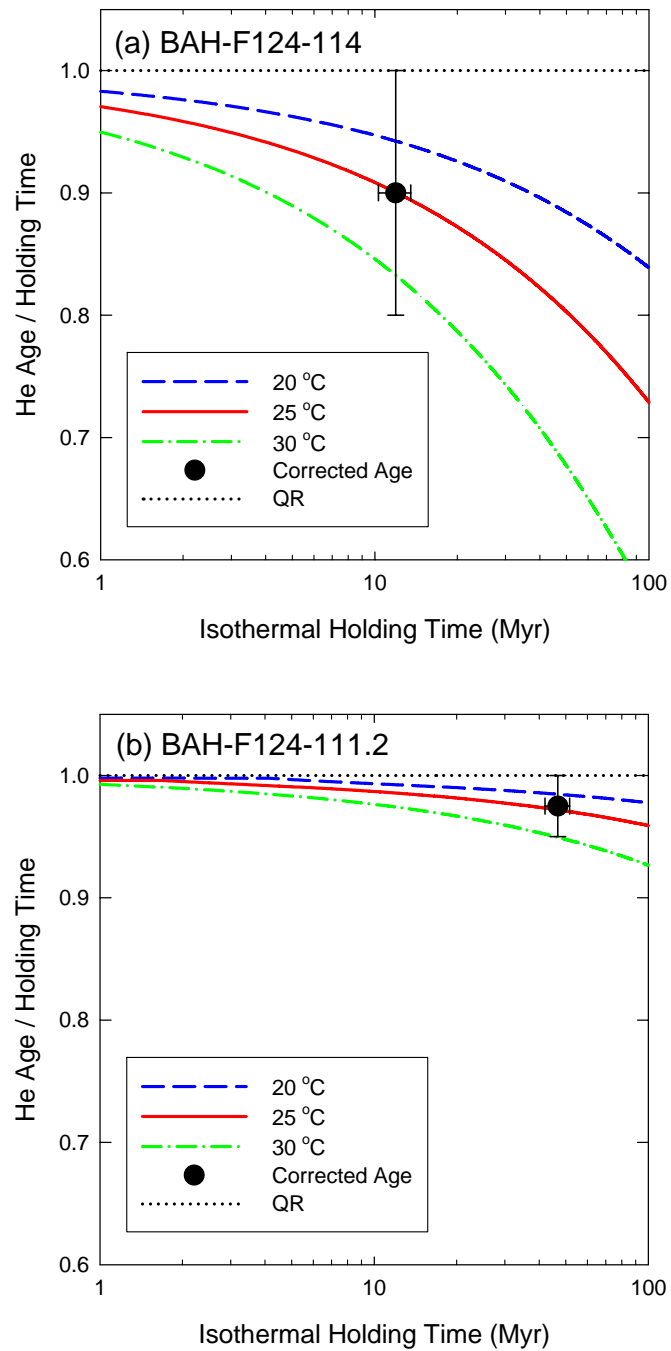


Figure 5. Helium-4 retention curves for (a) BAH-F124-114 and (b) BAH-F124-111.2.

Shown as solid curves are  $^4\text{He}$  retentivity factors (the He age divided by an isothermal

holding time) plotted vs. isothermal holding time in Myrs. Three curves were calculated for 20, 25 and 30 °C according to the HRD diffusion parameters summarized in Table 4 and the formulation of Wolf et al. (1998). Also plotted are the independently determined corrected He ages and HRD retentivity factors (i.e., 1 - *deficit gas fraction*) for each sample. QR denotes quantitative <sup>4</sup>He retention in the HRD.

isothermal holding times. The calculations are shown for the HRD diffusivity functions  $D(T)/a^2$  for the two samples. Note that here we discuss only the curves and that the points corresponding to “corrected ages” will be considered in a later section (see He age corrections). The curves in Fig. 5 clearly illustrate that the helium retentivity of the two samples is different. For instance, at 25 °C after 10 Myrs the HRD in sample 114 would have a deficit gas fraction of 10% (He age/holding time = 0.90), whereas the HRD in sample 111.2 would have a deficit gas fraction of only ~1%. Deficit gas fractions are defined as  $(N_{diff} - N_{uniform})/N_{uniform}$ , where N is the total amount of <sup>4</sup>He in a diffusively modified profile ( $N_{diff}$ ) and a uniform profile ( $N_{uniform}$ ) resulting from quantitative retention [49].

The curves in Fig. 5 also illustrate that helium retention in polycrystalline goethite is strongly temperature dependent. Future studies involving goethite will require careful sample selection and consideration of thermal conditions. For instance, these goethites would be susceptible to diffusive <sup>4</sup>He loss associated with intense solar heating and episodic forest fires if they were located at the surface. The results clearly indicate that <sup>4</sup>He is not expected to be quantitatively

retained in the two Bahia samples, but that significant fractions of gas should be retained. Although the curves presented in Fig. 5 are useful for predicting an *expected* degree of diffusive loss, a detailed interpretation of the ratio evolution diagrams should permit quantification of the deficit gas fraction.

## 7. Stepwise degassing experiments - Discussion

Under the assumption that proton-induced  $^3\text{He}$  was uniformly produced and reflects *all* of the diffusion domains that may be present in each sample, the interpretation of the ratio evolution diagrams (Fig. 4) yields a quantitative description of helium diffusion from all of the domains in the samples. Likewise, the interpretation of the  $^3\text{He}$  diffusion experiments and the extraction of diffusion parameters from them rely upon our anticipation of multiple diffusion domain sizes in the polycrystalline goethite aggregates. In this sense, our treatment of the  $^3\text{He}$  release data is analogous to and based on previous work using neutron-induced  $^{39}\text{Ar}$  in feldspars [96, 107] and natural  $^4\text{He}$  in titanite [5] and zircon [108] to identify multiple diffusion domains.

The distinct arrays and breaks in slope observed in Fig. 2 preclude the possibility that a single diffusive lengthscale (i.e.,  $a$  in  $D/a^2$ ) characterizes helium diffusion in either sample. The presence of more than a single diffusion domain complicates a diffusion experiment. Gas initially extracted from a distribution of diffusion domains will be a mixture: a larger fraction from less retentive domains and a smaller fraction from more retentive domains. Since the mathematics of

Fechtig and Kalbitzer (1966) assume that the gas is derived from a single domain, the presence of a small volume fraction of low retentivity domains will result in values of  $D/a^2$  that are initially higher than the mean for a given temperature.

If the diffusivity,  $D(T)$ , is the same throughout all domains, each would share common activation energy  $E_a$  and therefore a common slope on an Arrhenius plot. The origin of initially higher values of  $D/a^2$ , then, would simply be the dominance of a smaller domain radius,  $a$ , at that stage of the experiment. Alternatively, if the domains have significantly different  $E_a$ , the slopes of the arrays could be distinct. As an experiment proceeds, gas is progressively extracted from all diffusion domains. The less retentive domains will exhaust first, causing a transition in the calculated  $D/a^2$  values to those associated with the more retentive domains.

It is important to note that the exact shape of an Arrhenius plot is a strong function of the heating schedule used. For instance, a diffusively modified distribution or multiple diffusion domain sizes can cause retrograde cycles to appear different from prograde steps [96, 107]. Indeed, these are reasons for including retrograde cycles in our experiments (see Table 3). A successful multiple-domain model should reproduce the shape of an Arrhenius plot in detail. For this reason, we constructed models with the same heating schedule as used in the experiments.

### 7.1 Two-domain model

To describe the  $^3\text{He}$  release patterns for each experiment, we developed two-domain models to reproduce the observed  $^3\text{He}$  Arrhenius plots. Since the bulk of each sample (the HRD) was well-characterized by the arrays of lower diffusion coefficients, a relatively narrow range in HRD diffusion parameters was permissible in the models. And, since the two arrays in each experiment were quite distinct, the volume fractions of the LRD were well-approximated by the cumulative  $^3\text{He}$  release fraction up to the point the arrays converge (4% and 8% as discussed above). Therefore, the two-domain models each effectively had only two free parameters,  $E_a$  and  $\ln(D_o/a^2)$ , for the LRD. However, diffusion coefficients calculated *throughout* the experiment are somewhat dependent upon the LRD, and the extraction of the HRD diffusion parameters from Fig. 2 requires consideration of all domains present. Although more complicated models involving more than two domains or a continuum of domains could be developed, the highly simplified two-domain models are sufficient to explain the  $^3\text{He}$  observations. As such, we must emphasize that each two-domain model is a non-unique solution.

The models were calculated by assuming that the  $^3\text{He}$  distributions were initially uniform within two distinct populations of domains, and gas was not permitted to exchange between domains. Release fractions from the HRD and LRD were calculated separately using the heating schedules of each experiment, then summed at each step to yield a two-domain model  $^3\text{He}$  release pattern. The

calculations were iterated by adjusting  $E_a$  and  $\ln(D_0/a^2)$  for the LRD until each model was consistent with the observed Arrhenius plots shown in Fig. 2.

The best-fit two-domain models are shown in Fig. 2 as solid curves. We found model parameters that successfully reproduce the shapes of the Arrhenius plots and that the activation energies of the LRD are well-approximated by the slopes of the LRD arrays. We also found that the best-fit model diffusion parameters for the HRD were well-approximated by the independent linear regressions through the arrays of lower diffusivity (see above). This is primarily due to the substantial difference in diffusivity between the two domains. For reference, the LRD and HRD diffusion parameters are plotted as dotted and dashed lines, respectively, in Fig. 2 and also summarized in Table 4.

Under the two-domain model, the  $^3\text{He}$  Arrhenius plots indicate that the helium diffusion in the LRD behaves quite differently between sample 114 and 111.2. Although both of the LRD are effectively not helium retentive over geologic time, their relative proportions are important characteristics of each sample. Although the diffusion properties of each LRD may provide insight into what the domains represent (see below), the excellent agreement between models and observations in Fig. 2 does not rigorously prove bidomainality. Regardless of their physical significance, the two-domain models provide a framework which can be used to interpret the  $^4\text{He}/^3\text{He}$  ratio evolution diagrams.

Table 4. Two-domain model diffusion parameters

Sample	$f_V$	$E_a$ (kJ/mol)	(+/-)	$\ln(D_o/a^2)$ $\ln(s^{-1})$	(+/-)	$R^2$
BAH-F124-114						
HRD	0.96	162.8	2.4	26.0	0.6	0.997
LRD	0.04	162.8	-	37.3	-	-
BAH-F124-111.2						
HRD	0.92	178.4	2.6	28.3	0.6	0.996
LRD	0.08	45.6	-	1.3	-	-

HRD is “high retentivity domains” and LRD is “low retentivity domains”. Standard errors in the regression statistics are reported for the HRD at the 95% confidence level.

## 7.2 *Quantifying deficit gas fractions*

If the spatial distribution of  $^4\text{He}$  within the goethites can be constrained, then the deficit gas fraction can be quantified. The deficit gas fraction is useful for correcting an absolute He age for diffusive  $^4\text{He}$  loss.

Given the two-domain models summarized in Table 2, and using the methods described by Shuster and Farley (2004), we simulated the expected  $^4\text{He}$  distributions within the samples under different isothermal conditions over geologic time. We assumed that the diffusivity of proton-induced  $^3\text{He}$  and radiogenic  $^4\text{He}$  is equivalent in these samples, although our results are not strongly sensitive to this assumption [14]. Each simulation was required to result in the observed He ages (10.7 and 42.6 Ma for sample 114 and 111.2, respectively), and each corresponds to a different deficit gas fraction.

The model  $^4\text{He}$  distributions were first calculated for the HRD of each sample, and then passed through a simulated degassing experiment to produce a

set of  $^4\text{He}$  release fractions. Because the LRD of each sample are effectively non-retentive, their presence could be ignored in the profile calculating step. For instance, any radiogenic  $^4\text{He}$  produced within the LRD would be “immediately” lost on a geologic timescale. To simulate ratio evolution diagrams, a uniform distribution of  $^3\text{He}$  within both domains was also passed through the same simulated degassing experiment from which model  $^4\text{He}/^3\text{He}$  could be calculated.

The  $^4\text{He}$  modeling results are presented as curves in Fig. 4. Several features in the models of both samples are immediately apparent. First, the models successfully reproduce the low  $^4\text{He}/^3\text{He}$  ratios at the beginning of each experiment. This is clearly controlled by the relative proportion of the  $^3\text{He}$ -only containing LRD and illustrates how well those proportions are constrained. Second, both sets of models successfully reproduce the gradual and sharp rises in  $^4\text{He}/^3\text{He}$  for sample 114 and 111.2, respectively, each followed by nearly invariant ratios.

Although the models do not perfectly match the data, we can use them to place strong limits on the degrees of diffusive  $^4\text{He}$  loss for each sample. For instance, if the models are accurate, sample 114 has retained  $> 75\%$  of its  $^4\text{He}$ , and 111.2 has retained  $> 90\%$ . We can also rule out the possibility that either sample quantitatively retained  $^4\text{He}$ . Despite significant scatter in the data, particularly during the retrograde cycles during which gas yields were low, we find that a 10% and a 2.5% deficit gas fraction best reproduces the results of sample 114 and 111.2, respectively.

### 7.3 *He age corrections*

Assuming that both domains are inherent to each sample and that radiogenic  $^4\text{He}$  was naturally produced uniformly throughout each domain, the modeling results suggest that two components must be quantified and added back into the  $^4\text{He}$  budget of each sample to correct its (U-Th)/He age. These components are the  $^4\text{He}$  quantitatively lost from the non-retentive LRD and the deficit gas fraction of  $^4\text{He}$  diffusively lost from the HRD of each sample.

Using a HRD deficit gas fraction of 10% for sample 114, we can correct the measured  $^4\text{He}$  concentration for partial diffusive loss from those domains, where corrected He content = measured content  $\div$  (1 – deficit gas fraction) [49]. This corrects the measured He age (10.7 Ma) to 11.8 Ma. The LRD represents 4% of the total  $^3\text{He}$  budget. If  $^4\text{He}$  produced in the LRD was quantitatively lost over geologic time, a similar correction brings the final corrected He age to 12.3 Ma. If we conservatively assume 100% uncertainty on each correction, the final age of sample 114 is  $12.3 \pm 1.6$  Ma. For BAH-F124-111.2 we estimate the HRD deficit gas fraction to be  $\sim 2.5\%$  and the fraction of gas lost from the LRD to be 8%. Applying both corrections and assuming 100% uncertainty on each brings the measured He age of 42.6 Ma to a final corrected age of  $47.5 \pm 4.9$  Ma for sample 111.2.

It is difficult to estimate the actual uncertainty associated with the two corrections we describe above. Uncertainties associated with measured release

fractions; linear Arrhenius regressions and the fits of  $^3\text{He}$  Arrhenius models; individual He, U, and Th measurements; raw aliquot He age reproducibility, U series secular disequilibrium; and the fits of ratio evolution models all contribute to the final uncertainty of a corrected He age. In these types of samples, we can easily measure  $[\text{}^4\text{He}]$ ,  $[\text{U}]$ , and  $[\text{Th}]$  to better than  $\sim 1\%$  analytical precision, and we find good He age reproducibility (Table 1). However, the uncertainty in a weathering product He age will be dominated by the uncertainty in He loss corrections described above. By assuming 100% uncertainty, we place a very conservative estimate of the uncertainty in a corrected He age.

An important caveat to the HRD correction is the possibility that an even higher retentivity domain exists in the sample but is not interrogated until the final total fusion of the sample at  $\sim 1300\text{ }^\circ\text{C}$  (last step, Table 3). Such a domain would be unrecognized in Fig. 2. However, since a domain of sufficiently distinct retentivity would likely require distinct chemistry, the domain may have a different U, hence  $^4\text{He}$  content. Such a scenario could be recognized by the ratio evolution diagram if the total fusion step had a sufficiently different  $^4\text{He}/^3\text{He}$  than the rest of the sample. Rigorously, the HRD correction is only valid for the fraction of the sample interrogated by the Arrhenius plot. We have implicitly assumed that domains of higher retentivity than the HRD do not exist in either sample.

The magnitude of the above corrections illustrates the limitation of this dating technique and emphasizes the value of performing a stepped degassing

analysis on a sample. Although more labor intensive than determining a basic (U-Th)/He age, the ability to recognize non-quantitative  $^4\text{He}$  retention and apply age corrections improves the accuracy of the precipitation ages.

#### 7.4 *Internal consistency and mean temperature*

If the corrected He ages represent the true precipitation age of each sample, the pair of Bahia goethites provides a test for internal consistency. Goethite samples 114 and 111.2 were located 3 meters from one another in the weathering profile. For at least the duration of the younger sample's existence, this pair must have shared a common thermal history. We *a priori* expect that the mean temperatures these samples experienced were controlled by the mean annual air temperature of the region, 23°C. Although the mean temperature over the last ~40 Myrs is not well-known, the samples should have remained well below 35°C throughout their existence.

Using  $^3\text{He}$  derived diffusion parameters for the HRD of each sample, the production/diffusion model predicts a He age and concentration profile for a given isothermal holding time and temperature (Fig. 5, curves). The diffusion-corrected He ages and the HRD deficit gas fractions determined from Fig. 4 provide us the ability to superimpose each sample on the curves, shown as solid circles. Each sample indicates a physically reasonable residence temperature of ~25 °C. The agreement between these results and the actual mean temperature of 23°C is significant, indicating that the diffusive loss corrections, the LRD

corrections, and the temperature extrapolations of the  $^3\text{He}$  determined functions  $D(T)/a^2$  are not severely inaccurate. Failure of this test would indicate inaccuracy in any of the above.

#### 7.5 *Physical significance of diffusion domains*

The physical significance of the apparent diffusion domains remains an unanswered question about these samples. Unlike single euhedral crystals, in fine-grained polycrystalline material the physical identity of diffusion domains is unclear. The diffusion domain(s) may correspond to individual FeOOH crystals of various sizes, amorphous intergranular media, or even the bulk aggregate geometry in the case of the HRD.

If the bulk aggregate geometry defines the high retentivity diffusion domains, then we expected to find a difference between the two diffusion experiments performed on BAH-F124-114. Because we analyzed an aliquot  $\sim 1$  mm in chip radius and one  $\sim 200$   $\mu\text{m}$  in radius, a difference in  $\ln(D_0/a^2)$  of  $\sim 3$  natural log units would be expected. Although the aliquots were not perfectly spherical, a difference in  $\ln(D_0/a^2)$  of 3  $\ln$  units should be detectable despite the coarseness with which the 200  $\mu\text{m}$  experiment was conducted. We found no significant difference between the HRD regressions of each Arrhenius plot. This implies that the characteristic domain size,  $a$ , is significantly smaller than the bulk aggregate geometry, and common to both aliquots.

The LRD diffusion parameters of sample 111.2 are very different from the rest of the sample, and also very different from the LRD of sample 114. Although both of the LRD diffuse helium rapidly, the very low activation energy (46 kJ/mol) of the LRD of sample 111.2 indicates that those domains are fundamentally distinct from the rest of the sample. Previous work with Mn-oxides revealed the residence of  $^{40}\text{Ar}$  in domains thought to be very low retentivity inter-granular regions. This inter-granular domain hosts atmospheric  $^{40}\text{Ar}$ ,  $^{38}\text{Ar}$ , and  $^{36}\text{Ar}$ , but does not contain any significant radiogenic ( $^{40}\text{Ar}^*$ ) or nucleogenic gas (e.g.,  $^{37}\text{Ar}$  and  $^{39}\text{Ar}$ ). The volume of inter-granular space determines the density of the sample and depends on the packing of the acicular or rod-shaped hollandite and goethite microcrystallites. In addition, the retentivity of the inter-granular space may vary locally, depending on crystallite shape, size, and packing density. If this is also true of helium in polycrystalline goethite, we should expect variability in the relative proportions of HRD and LRD between samples related to the packing density of aggregated crystals and crystallinity index. Future studies involving careful characterization of sample crystallinity and trace chemical impurities are required to fully understand the physical significance of the apparent domains.

#### 7.6 *General extrapolation of goethite diffusion parameters*

Despite general agreement between the measured diffusion parameters for the two goethites, every polycrystalline goethite aggregate may behave

differently. The diffusion domain size distribution as well as an aggregate's physical characteristics such as crystallinity and morphology may vary significantly from sample to sample. Until the relevant parameters that control  $^4\text{He}$  diffusion in goethite have been identified and quantified, it may be necessary to perform an irradiation/diffusion experiment to accurately interpret or correct goethite He ages.

## 8. Conclusions

Goethite (U-Th)/He dating is a viable weathering geochronometer. We found (U-Th)/He ages determined on aliquots of polycrystalline goethite to be reproducible despite variability in U and Th content. Stepwise degassing analyses of proton-irradiated aliquots have revealed the following about two polycrystalline goethites: (1)  $^3\text{He}$  does not reside in a single diffusion domain, but resides in at least two distinct domains; (2) two-domain models constrain the functions  $D(T)/a^2$  for each domain and the relative proportions of  $^3\text{He}$  located in each; (3) ratio evolution diagrams reveal diffusive  $^4\text{He}$  profiles across the samples, and (4) the two samples retain  $^4\text{He}$  to different degrees.

Although  $^4\text{He}$  is not quantitatively retained in aggregated polycrystalline goethites, the magnitude of diffusive loss is not prohibitive. The ability to rigorously quantify diffusive-loss corrections by using the proton-irradiation  $^4\text{He}/^3\text{He}$  method enables goethite precipitation ages to be determined.

The widespread distribution of goethite in weathering profiles on Earth and possibly other terrestrial planets and the feasibility of dating goethite by the (U-Th)/He method opens new opportunities for quantifying water-rock interaction in the geological past. Application of goethite (U-Th)/He dating, if combined with stable isotope studies (O, H, and C), may provide a feasible mechanism for generating a nearly continuous paleoclimatic curve for continental areas suitable for comparison with the record preserved in oceanic reservoirs.

*Acknowledgements.* We thank L. Hedges and C. Paine for sample preparation and J. Sinsterson and E. Cascio for their expertise with the proton irradiation. We thank P. Reiners and an anonymous reviewer for their constructive comments on the manuscript. This work was supported by the National Science Foundation and UQ-AGES (University of Queensland Argon Geochronology in Earth Sciences) Laboratories. D.L.S. was supported by an N.S.F. Graduate Research Fellowship.

*Chapter 4*DIFFUSION KINETICS OF PROTON-INDUCED  $^{21}\text{NE}$ ,  $^3\text{HE}$ , AND  $^4\text{HE}$   
IN QUARTZ

D. L. Shuster

K. A. Farley

(This chapter was reprinted from *Geochimica et Cosmochimica Acta* (2005), 69(9) pp 2349-2359)

**Abstract** - A natural quartz sample free of mineral and fluid inclusions was irradiated with a 200 MeV proton beam to produce spallogenic  $^{21}\text{Ne}$ ,  $^3\text{He}$  and  $^4\text{He}$ . Temperature-dependent diffusivities of these three nuclides were then determined simultaneously by high precision stepped-heating and noble gas mass spectrometry. The outward mobility of proton-induced nuclides reflects diffusion through the quartz lattice. In the studied range of 70-400°C the helium diffusion coefficients exceed those of neon by 5-7 orders of magnitude. The implied diffusion parameters  $E_a = 153.7 \pm 1.5$  (kJ/mol) and  $\ln(D_0/a^2) = 15.9 \pm 0.3$  ( $\ln(\text{s}^{-1})$ ) and  $E_a = 84.5 \pm 1.2$  (kJ/mol) and  $\ln(D_0/a^2) = 11.1 \pm 0.3$  ( $\ln(\text{s}^{-1})$ ) for proton-induced  $^{21}\text{Ne}$  and  $^3\text{He}$ , respectively, indicate that cosmogenic neon will be quantitatively retained in inclusion-free quartz at typical Earth surface

temperatures whereas cosmogenic helium will not. However, the neon diffusion parameters also indicate that diffusive loss needs to be considered for small (< 1 mm) quartz grains that have experienced elevated temperatures. Since natural quartz often contains fluid inclusions that may enhance noble gas retentivity, these parameters likely represent an end-member case of purely solid-state diffusion. The  $\sim 70$  kJ/mol higher activation energy for neon diffusion compared to helium diffusion likely represents an energy barrier related to its  $\sim 13\%$  greater diameter and provides a fundamental constraint with which to test theories of solid-state diffusion. The diffusion parameters for proton-induced  $^4\text{He}$  are indistinguishable from those for  $^3\text{He}$ , providing no evidence for the commonly expected inverse square root of the mass diffusion relationship between isotopes. We also find preliminary indication that increased exposure to radiation may *enhance* neon and helium retentivity in quartz at low temperatures.

## 1. Introduction

Over the last two decades, measurement of the stable cosmogenic noble gases  $^3\text{He}$ ,  $^4\text{He}$ ,  $^{21}\text{Ne}$ ,  $^{22}\text{Ne}$ ,  $^{38}\text{Ar}$ , and  $^{83}\text{Kr}$  has become an essential tool for determining the exposure duration of terrestrial and extraterrestrial materials to cosmic rays [18, 19]. With knowledge of the production rate and the retentivity of a cosmogenic nuclide in a specific mineral, a surface exposure timescale can be calculated from an atomic concentration in that mineral. For example,

cosmogenic  $^{21}\text{Ne}$  concentrations in quartz are widely used to constrain erosion rates or exposure ages in terrestrial geological problems [18, 52, 109-115].

Although much work has been done to calibrate and understand the terrestrial production rate of helium and neon in quartz [18, 116], their diffusion kinetics in this mineral have not been well-characterized. The general consistency between  $^{21}\text{Ne}$ -based exposure ages and those based on  $^{10}\text{Be}$  and  $^{26}\text{Al}$  concentrations has been used to argue for quantitative retention of  $^{21}\text{Ne}$  in quartz under Earth surface conditions [110, 113, 117], but provides no information on the temperature dependence of diffusivity nor any insight as to whether small quartz grains might incompletely retain neon. In the case of helium, the experimental results of Trull et al. (1991) suggest nearly quantitative retention over  $10^6$  year timescales in quartz, but exposure ages of natural quartz samples indicate otherwise [18, 118, 119]. The inconsistency between exposure ages derived from  $^3\text{He}$  and those based on  $^{10}\text{Be}$  and  $^{26}\text{Al}$  has been interpreted to indicate that quartz does not retain helium at typical Earth surface temperatures. A successful physical model of solid-state diffusion should be able to predict why quartz should apparently retain neon but not retain helium.

The current mechanistic understanding of solid-state diffusion of noble gases through crystalline materials is based on limited experimental results. Measurement of diffusion coefficients typically entails the direct determination of concentration profiles following inward diffusion (charging experiments, e.g., [120]) or, more commonly, measuring gas release during step-heating of a sample

with either natural or artificially added diffusant (degassing experiments, e.g., [4, 24, 121, 122]). Owing to analytical challenges of directly measuring noble gas concentration profiles over small lengthscales ( $< 1 \mu\text{m}$ ), the latter is usually more straightforward and precise. Calculating diffusion coefficients from a degassing experiment requires specification of the initial spatial distribution of the diffusant. Because spatial distributions of naturally occurring noble gases are commonly unknown, the results can be uncertain and will be erroneous if the actual distribution is not equivalent to the assumed initial distribution [49]. Furthermore, since the activation energy of a migrating noble gas atom may depend on the specific siting that the atom initially occupies in a mineral matrix, degassing experiments can be complicated by the presence of multiple noble gas components as well as by radiation damage and fluid and mineral inclusions [4, 13, 23, 114].

Here we present the results of two experiments in which the diffusion kinetics of proton-induced  $^{21}\text{Ne}$  and  $^3\text{He}$  (and  $^4\text{He}$  in one experiment) were determined in a natural sample of quartz using the step-heating technique. The first experiment used higher proton fluence (see **Methods**), and an additional experiment used a proton fluence approximately one order of magnitude lower to test for possible effects that proton irradiation may have upon diffusion kinetics. By irradiating quartz with a 150-200 MeV proton beam, we induced nuclear transmutations of the Si and O atoms to generate a uniform distribution of purely synthetic, single-component noble gases. The ability to generate multiple

elements and isotopes makes proton-induced noble gases attractive for studying size and isotope effects in solid-state diffusion.

Because the nuclear transmutations in our experiments are similar to those which occur through cosmic ray interactions in quartz, the proton-induced nuclides should be good analogs for naturally occurring cosmogenic neon and helium (see Discussion). Moderate and high-energy proton bombardment produces spallation  $^3\text{He}$  from both Si and O in exactly the same way that cosmogenic  $^3\text{He}$  is produced in meteorites in space [19, 50, 121]. Since Si nuclei are effectively the only targets that produce  $^{21}\text{Ne}$  in our sample, a relatively limited number of multiple stage production pathways are probable and should also be the same as those that occur in nature.

## 2. Sample description and methods

The analyzed sample was pure quartz collected from a quartz vein in Conselheiro Mata, Minas Gerais, Brazil (GRR-1668). The specimen was a gem quality, optically clear, single prismatic crystal of approximate dimensions  $9\times 0.5\times 0.5$  cm and was microscopically inspected to be free of mineral and fluid inclusions. Shown in Table 1 are the natural concentrations of  $^{21}\text{Ne}$ ,  $^3\text{He}$  and  $^4\text{He}$  in an aliquot of this sample, which indicate that it was essentially free of these nuclides prior to proton irradiation. We separately irradiated two  $\sim 100$  mg shards broken from the specimen's interior.

Details of the proton irradiations and analytical procedures have been described elsewhere [121]. In the first experiment (Experiment 1), the quartz sample was placed in an aluminum container and exposed to a 200 MeV proton beam for a continuous 8 hour period at the Northeast Proton Therapy Center receiving a fluence of  $\sim 6.3 \times 10^{15}$  protons/cm<sup>2</sup>. We estimate that the analyzed aliquot received a total dose of  $\sim 3.7 \times 10^{13}$  protons. The sample temperature did not exceed 45 °C during proton bombardment.

The diffusion experiment was performed  $\sim 12$  months after the proton irradiation. To ensure that each nuclide had an initially uniform distribution, a  $\sim 430$   $\mu\text{m}$  (radius) aliquot was broken out of the interior of the original  $\sim 2$  mm shard just prior to analysis. By analyzing an interior portion of the sample, we minimized the potential that the neon and helium distributions in the analyzed aliquot had become diffusively modified between irradiation and analysis.

The second experiment (Experiment 2, lower proton dose) was performed on an aliquot of the same sample and used the same procedures as described above. However, the aliquot was irradiated with a  $\sim 150$  MeV proton beam and received a total fluence of only  $\sim 2 \times 10^{14}$  p/cm<sup>2</sup>. This irradiation took place  $\sim 24$  months prior to the step-heating analysis.

The aliquots were each held at a known temperature for a known time in a volume of  $\sim 300$  cm<sup>3</sup> under static vacuum [56]. We then measured the isotopic abundances of helium and neon at each heating step to determine diffusion coefficients. Helium and neon were cryogenically separated using activated

charcoal; each element was analyzed separately on a MAP 215-50 mass spectrometer. We converted measured release fractions and the duration of each step to diffusion coefficients using published equations [24] and the assumptions therein. The estimated uncertainty on temperatures was better than  $\pm 2$  °C and on diffusion coefficients better than  $\pm 0.2$  natural log units for all points used in the regressions. From calculated diffusion coefficients and the temperature of each step, we generated Arrhenius plots to determine the activation energy,  $E_a$ , and frequency factor,  $D_0/a^2$ , by linear regression to define the function  $D(T)/a^2 = D_0/a^2 \exp(-E_a/RT)$  ( $D$  is the diffusion coefficient,  $a$  is the characteristic length scale of the analyzed diffusion domain,  $R$  is the gas constant). We assumed spherical geometry and initially uniform concentration profiles for each nuclide. To verify the assumed initial conditions of the experiment, the heating schedules included isothermal steps as well as both prograde and retrograde heating cycles (see Tables 2 and 4) [49].

### 3. Results

The total concentrations of proton-induced  $^{21}\text{Ne}$ ,  $^3\text{He}$ , and  $^4\text{He}$  are summarized in Table 1. These concentrations are generally higher than the wide range of natural cosmogenic concentrations that have been observed in quartz. Cosmogenic  $^{21}\text{Ne}$  concentrations in terrestrial quartz are of order  $10^6$ - $10^8$  atoms/gm [18, 109-111, 114, 123] and in meteorites they are more variable and generally larger,  $10^7$ - $10^{10}$  atoms/gm [19, 124]. Observations of cosmogenic  $^3\text{He}$

Table 1: Dose/yield summary for quartz

Experiment	Fluence ( $\times 10^{15}$ p/cm <sup>2</sup> )	Proton energy (MeV)	[ <sup>21</sup> Ne] (atoms/mg)	<sup>22</sup> Ne/ <sup>21</sup> Ne	[ <sup>3</sup> He] (atoms/mg)	<sup>4</sup> He/ <sup>3</sup> He
	0	n.a.	$<5.00 \times 10^4$	$\sim 10^1$	$<1.00 \times 10^3$	$\sim 10^4$
1	6.3	200	$6.61 \times 10^8$	0.61	$1.57 \times 10^9$	10.31
2 (lower dose)	0.2	150	$0.31 \times 10^8$	0.78	$0.04 \times 10^9$	-

The proton fluences and energies were estimated by each aliquot's position within the target stacks as discussed in [121]. Uncertainty in the dose and energy is estimated to be  $\pm 10\%$  relative error. For the irradiated samples, we estimate the atomic concentrations to be better than  $\pm 5\%$  for each presented nuclide. The concentrations for zero fluence are the natural concentrations determined on an un-irradiated aliquot. Note that <sup>21</sup>Ne and <sup>3</sup>He (and <sup>4</sup>He in Experiment 1) in the irradiated samples are almost exclusively synthetic. Measurements of Experiment 1 were made 12 months after irradiation, and those of Experiment 2 were made 24 months after irradiation. n.a. is not applicable. Dash "-" indicates below detection limit.

concentrations in terrestrial quartz are more sparse, but of order  $10^6$ - $10^8$  atoms/gm [23, 118].

The results of diffusion Experiment 1 for each isotope are presented in Table 2, and shown in Fig. 1 as a single Arrhenius plot. Regression statistics and the diffusion parameters  $D_0/a^2$  and  $E_a$  are summarized for each isotope in Table 2. We find that the calculated neon diffusion coefficients ( $D/a^2$ ) are five to seven orders of magnitude lower than the helium coefficients for temperatures at which both values were determined (between 100 °C and 250 °C). The Arrhenius plots show strong linear correlations between  $\ln(D/a^2)$  and  $1/T$  and reveal distinct diffusion parameters for each element.

The linear correlation between the  $^{21}\text{Ne}$  diffusion coefficients and  $1/T$  persists throughout the entire experiment, including a retrograde cycle and multiple isothermal steps between 125 °C and 400 °C. From linear regression, the  $^{21}\text{Ne}$  diffusion parameters are:  $E_a = 153.7 \pm 1.5$  (kJ/mol) and  $\ln(D_0/a^2) = 15.9 \pm 0.3$  ( $\ln(\text{s}^{-1})$ ) (SE;  $n = 30$ ).

Diffusion coefficients for the two helium isotopes are indistinguishable from each other as shown in Fig. 1. Indeed, the diffusion coefficients for both isotopes plot on top of one another at each temperature. With the exception of the first three measurements (at 100 °C, initial ~8% of the total gas yield), the diffusion coefficients plot on a line. For the first three points we observe a small and progressively decreasing *deficit* in the  $^3\text{He}$  and  $^4\text{He}$  diffusion coefficients (maximum deficit of  $\sim 1$   $\ln$  unit; see Fig. 1), where we define the deficit to be

Table 2: Stepped heating results (Experiment 1)<sup>a</sup>

Step	T (°C)	t (hr)	<sup>3</sup> He (x 10 <sup>6</sup> atoms)	(+/-)	<sup>4</sup> He/ <sup>3</sup> He	(+/-)	<sup>21</sup> Ne (x 10 <sup>6</sup> atoms)	(+/-)
1	99.5	0.5	48.3	0.9	8.5	1.7	-	-
2	99.8	1.0	50.0	1.0	9.2	1.7	-	-
3	99.8	2.0	67.1	0.8	12.9	1.2	-	-
4	79.9	1.0	7.1	0.4	10.4	3.7	-	-
5	79.9	1.0	6.8	0.4	10.3	3.7	-	-
6	70.0	2.0	5.7	0.2	10.5	2.9	-	-
7	69.9	2.0	5.3	0.4	10.5	3.3	-	-
8	69.8	2.0	4.6	0.1	10.5	3.3	-	-
9	89.8	1.5	17.3	0.7	12.0	1.9	-	-
10	89.8	2.0	23.1	0.7	12.0	1.6	-	-
11	99.8	1.5	33.5	1.0	10.8	1.2	-	-
12	119.5	0.5	42.3	0.9	9.7	0.9	-	-
13	119.6	0.5	38.0	1.0	9.6	1.0	-	-
14	119.2	0.5	33.4	0.8	10.5	1.1	0.05	0.10
15	139.4	0.5	101.2	1.5	10.0	0.4	0.04	0.09
16	139.4	0.5	75.0	1.6	9.9	0.6	0.03	0.10
17	139.7	1.0	114.6	1.8	10.3	0.4	0.04	0.07
18	159.2	0.5	139.1	2.3	10.3	0.3	0.08	0.05
19	159.9	1.0	186.8	2.4	10.2	0.2	0.12	0.05
20	174.2	0.5	157.7	2.0	10.1	0.3	0.16	0.05
21	174.6	0.5	111.2	1.7	10.1	0.4	0.11	0.05
22	199.7	1.0	321.2	3.0	10.3	0.1	0.84	0.09
23	199.9	0.5	59.6	1.1	10.1	0.7	0.25	0.05
24	224.8	0.5	73.6	1.2	10.4	0.6	1.16	0.10
25	224.9	1.0	23.1	1.3	12.6	1.6	1.29	0.13
26	249.8	0.5	2.0	0.8	9.0	2.3	2.65	0.16
27	249.8	1.0	-	-	-	-	3.49	0.21
28	274.8	0.5	-	-	-	-	6.26	0.24
29	275.0	1.0	-	-	-	-	8.91	0.29
30	299.8	0.5	-	-	-	-	15.36	0.32
31	299.7	1.0	-	-	-	-	20.13	0.47
32	324.9	0.5	-	-	-	-	29.20	0.57
33	324.8	1.0	-	-	-	-	38.52	0.72
34	350.1	0.5	-	-	-	-	46.25	0.66
35	349.7	1.0	-	-	-	-	55.01	0.78
36	337.7	1.0	-	-	-	-	21.31	0.58
37	311.7	1.3	-	-	-	-	5.88	0.24
38	287.8	1.5	-	-	-	-	1.76	0.11
39	259.3	2.0	-	-	-	-	0.42	0.07
40	238.0	3.0	-	-	-	-	0.14	0.05
41	250.0	2.0	-	-	-	-	0.19	0.06
42	274.9	1.5	-	-	-	-	0.70	0.08
43	299.9	1.0	-	-	-	-	2.41	0.18
44	324.8	0.5	-	-	-	-	4.99	0.22
45	349.9	1.0	-	-	-	-	30.38	0.51
46	374.9	1.0	-	-	-	-	64.97	0.80
47	399.9	1.0	-	-	-	-	98.85	1.00
Fusion	~1300	0.5	-	-	-	-	272.40	2.15
Total			1747.6				734.34	

<sup>a</sup>All values are corrected for blank contributions. Dash "-" indicates below detection limit. Mass analyzed = 1.1'

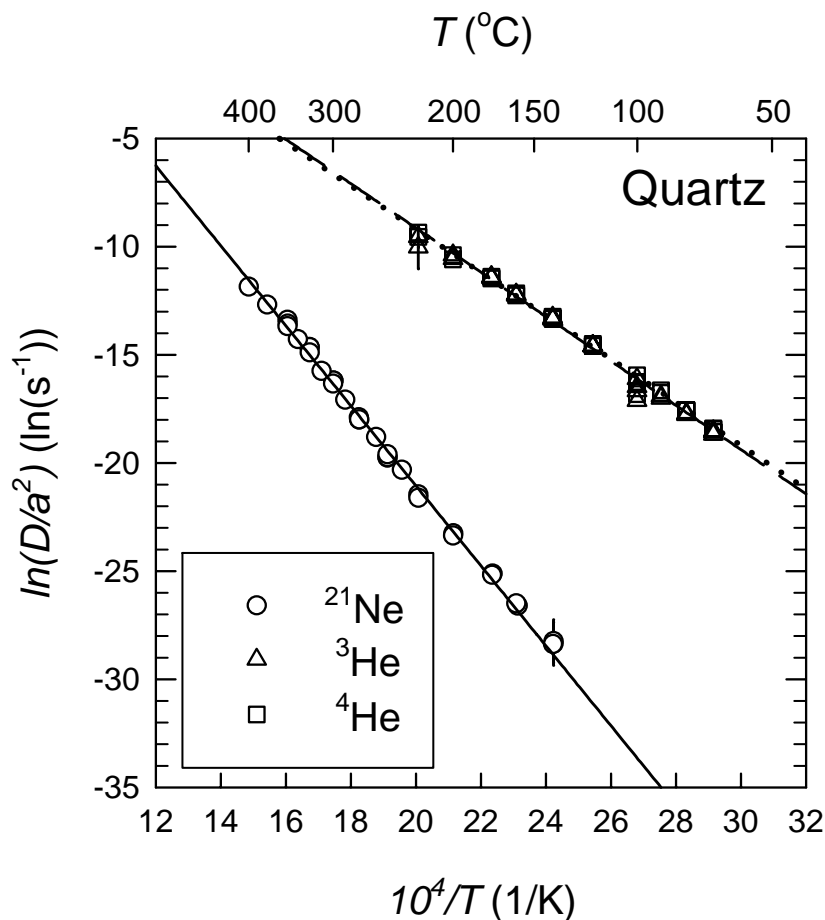


Figure 1. Arrhenius plot for proton-induced nuclides (Experiment 1). Open circles are values calculated from  $^{21}\text{Ne}$ , triangles from  $^3\text{He}$ , and squares from  $^4\text{He}$  results shown in Table 2. The solid line indicates least squares regression through the  $^{21}\text{Ne}$  results, dashed and dotted line through a subset of the  $^3\text{He}$  and  $^4\text{He}$  results, respectively.

anomalously low diffusion coefficients with respect to the array defined by the bulk of the data. The slight deficit may be related to the diffusive rounding of the helium isotope distributions during the 12 months spent at room temperature between proton irradiation and the degassing experiment (see Discussion). Although we broke out an interior aliquot, it is possible that we did not

completely avoid portions of the sample that had been diffusively modified. We therefore excluded these steps from Arrhenius regressions. Following these initial steps, strong linear correlation persists throughout a retrograde temperature cycle and multiple isothermal steps between 70 °C and 200 °C. Over these steps, ~90% of the helium was evolved from the sample. These data imply that  $E_a = 84.5 \pm 1.2$  (kJ/mol) and  $\ln(D_0/a^2) = 11.1 \pm 0.3$  (ln(s<sup>-1</sup>)) (SE; n = 21), and  $E_a = 83.2 \pm 0.8$  (kJ/mol) and  $\ln(D_0/a^2) = 10.8 \pm 0.3$  (ln(s<sup>-1</sup>)) (SE; n = 21) for <sup>3</sup>He and <sup>4</sup>He, respectively.

To highlight similarity in the diffusivity of the two helium isotopes, we also present in Fig. 2 the degassing results as a ratio evolution diagram (<sup>4</sup>He/<sup>3</sup>He<sub>step</sub> vs.  $\Sigma F^3\text{He}$  where <sup>4</sup>He/<sup>3</sup>He<sub>step</sub> is the measured ratio at each step, and  $\Sigma F^3\text{He}$  is the cumulative <sup>3</sup>He release fraction; [14, 49]). Diffusivity ratios  $D^4\text{He}/D^3\text{He}$  other than unity will cause values of <sup>4</sup>He/<sup>3</sup>He<sub>step</sub> to systematically deviate from the bulk ratio at high values of  $\Sigma F^3\text{He}$ . Throughout the entire experiment the observed <sup>4</sup>He/<sup>3</sup>He ratios are very nearly constant indicating nearly identical diffusivities. Although there is scatter in the initial steps (predominantly due to the magnitude and uncertainty in <sup>4</sup>He blank corrections at those steps), we find no significant deviation from the bulk <sup>4</sup>He/<sup>3</sup>He ratio when  $0.20 < \Sigma F_i^3\text{He} < 0.99$ . Shown in the inset of Fig. 2 are the error-weighted residual sums of squares between models calculated for a given value of  $D^4\text{He}/D^3\text{He}$  and our <sup>4</sup>He/<sup>3</sup>He observations. For models of nearly equivalent diffusivity (i.e.,  $D^4\text{He}/D^3\text{He} = 1$  and 1.05), we find

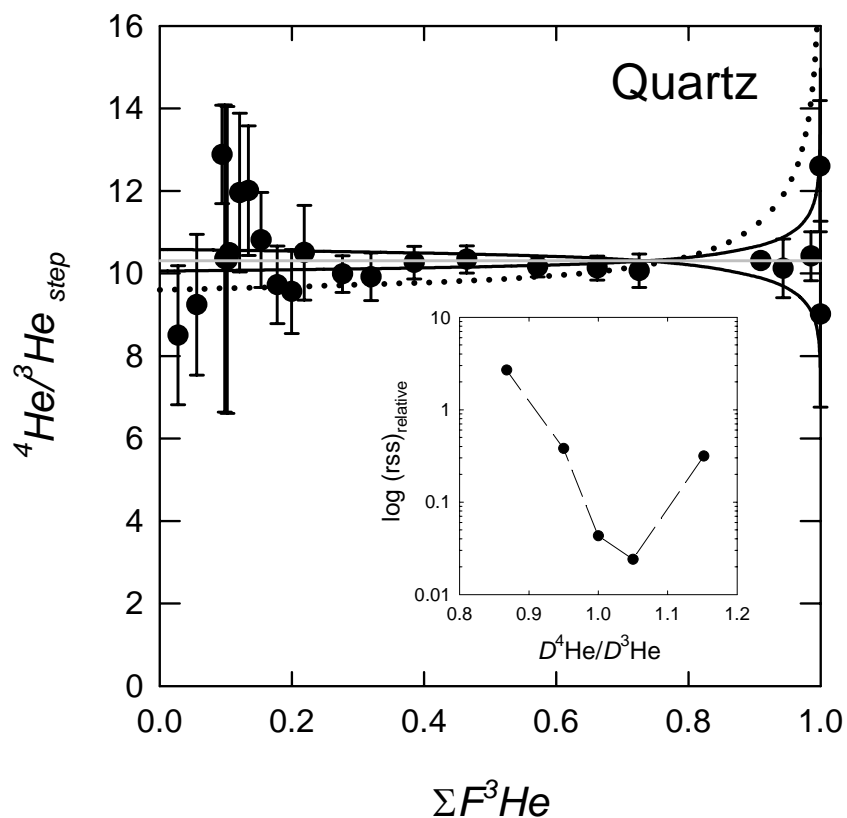


Figure 2. Ratio evolution diagram (Experiment 1). Shown are measured helium isotope ratios for each release step,  ${}^4\text{He}/{}^3\text{He}_{\text{step}}$ , plotted vs. the cumulative  ${}^3\text{He}$  release fraction,  $\Sigma F^3\text{He}$ . Four diffusion models are shown. The model of equivalent diffusivity,  $D^4\text{He}/D^3\text{He} = 1.00$ , which well fits the entire dataset, is shown as a solid gray line. Of particular significance are the 12 points plotting between  $0.30 < \Sigma F^3\text{He} < 0.99$ . Two reference models are shown as solid black curves:  $D^4\text{He}/D^3\text{He} = 1.05$  and  $0.95$ , respectively. We also show as a dotted curve the model corresponding to the inverse root mass relationship:  $D^4\text{He}/D^3\text{He} = \sqrt{m_3/m_4} = 0.868$ . The magnitude of the error bars are dominated by and estimated by uncertainty in the  ${}^4\text{He}$  blank corrections. The inset shows the error weighted residual sums of squares between models calculated for a given value of  $D^4\text{He}/D^3\text{He}$  and the entire set of  ${}^4\text{He}/{}^3\text{He}$  observations.

residual sums of squares that are approximately two orders of magnitude smaller than that for the canonical inverse root mass relationship, indicating that these models more successfully predict the data. In the discussion below, we will focus on  $^3\text{He}$  rather than  $^4\text{He}$  diffusivity because the  $^3\text{He}$  results have better analytical precision.

The results of diffusion Experiment 2 (lower proton dose) for each isotope are presented in Table 4, and shown in Fig. 3 as an Arrhenius plot. These results are presented and discussed in more detail below (see section 4.3).

## 4. Discussion

### 4.1. Diffusion kinetics of proton-induced nuclides

We believe the diffusion parameters of proton-induced  $^{21}\text{Ne}$ ,  $^3\text{He}$ , and  $^4\text{He}$  are well-characterized by Experiment 1 for a number of reasons. The persistence of Arrhenian linearity throughout retrograde heating cycles and isothermal heating steps precludes the possibility of several complications. Retrograde temperature cycling is sensitive to (i) the presence of an initial distribution that is not uniform and (ii) the presence of a distribution of domain sizes [10, 14, 25, 55]. Under the conditions of the experiment, both complications would result in non-linear patterns that are not observed in Fig. 1. Furthermore, since the experiment was conducted at low temperatures, and since the correlations persist over significant cumulative fractions for each gas, we can rule out the presence of inclusions with distinct retention properties. Each of

these complications is usually expressed in an Arrhenius plot as a “break in slope,” which is clearly not observed in Fig. 1.

The room temperature diffusivity of proton-induced helium is sufficiently high to have caused diffusive loss from the irradiated sample over month timescales. For instance, we estimate that the original 2 mm (radius) grain would have lost ~5% of its helium between the time of irradiation and analysis, causing a diffusively rounded profile in the outer ~50  $\mu\text{m}$ . It was critical for our experiment that we broke out an interior aliquot for the analysis, yet we still apparently observe the effect of diffusive rounding. The influence of even ~1% loss could result in the slight deficit observed in Fig. 1 [49]. Note that diffusive loss of  $^{21}\text{Ne}$  over this time would be negligible.

#### *4.2. Proton-induced nuclides as cosmogenic analogs*

An important question for interpreting and comparing our diffusion parameters with those determined for naturally occurring cosmogenic nuclides is whether the synthetically and naturally produced nuclides are analogous. If the proton-induced nuclides are produced through significantly different production pathways and with different energies than in nature, their initial siting in the quartz lattice could be different. Although not at all clear what influence the initial siting should have upon noble gas diffusion kinetics in quartz, these possibilities require consideration.

Silicon is transmuted to neon and helium through multi-stage production pathways. These pathways likely involve the “evaporation” of charged particles from an excited residual nucleus [51, 121]. In spallation reactions involving charged particle evaporation, the kinetic energies of the “evaporation” particles (e.g.,  $^3\text{He}$ ,  $^4\text{He}$ , p, n, etc.) and residual nuclei (e.g.,  $^{21}\text{Ne}$ ) are not expected to be a function of incident particle energy above a certain threshold. Therefore, the kinetic energies of the final spallation products induced by 200 MeV protons are likely to be similar to those produced in situ from primary galactic cosmic ray protons, which have peak energy of  $\sim 650$  MeV [125]. Cosmogenic and proton-induced  $^{21}\text{Ne}$  are not expected to have energies greater than 1 MeV/amu; the  $^{21}\text{Ne}$  nuclei are likely to have traversed at least several tens of lattice spaces from the original Si siting. The ejection trajectories of the charged particles should be approximately stochastic so the final  $^{21}\text{Ne}$  distribution is expected to be very nearly uniform throughout the crystal. Since the production ratio of  $^{22}\text{Ne}/^{21}\text{Ne}$  is somewhat dependent upon the energy of the incident particle(s) [50], a comparison between the  $^{22}\text{Ne}/^{21}\text{Ne}$  ratio induced in our sample and natural cosmogenic  $^{22}\text{Ne}/^{21}\text{Ne}$  ratios should provide some insight to the respective production mechanisms.

Leya et al. (1998) measured cross sections for the reactions  $\text{Si}(p,X)^{21}\text{Ne}$  and  $\text{Si}(p,X)^{22}\text{Ne}$  with 180 MeV protons:  $\sigma_d(^{21}\text{Ne}) = 18.5 \pm 1.0$  mb,  $\sigma_d(^{22}\text{Ne}) = 7.6 \pm 0.9$  mb, and  $\sigma_c(^{22}\text{Ne}) = 24.9 \pm 3.3$  mb, where X represents the cumulative spallation products complementary to  $^{21}\text{Ne}$  or  $^{22}\text{Ne}$ ,  $\sigma_d$  is the cross section

calculated for instantaneous production, and  $\sigma_c$  is the cumulative cross section that takes into account delayed production from the decay of proton-induced  $^{22}\text{Na}$  (mean life  $\tau = 3.76$  yr). From these data, we expect an instantaneous  $^{22}\text{Ne}/^{21}\text{Ne}$  production ratio of  $0.41 \pm 0.05$ , and a gradual increase in the  $^{22}\text{Ne}/^{21}\text{Ne}$  over time to a value of  $\sim 1.3 \pm 0.2$  as  $^{22}\text{Na}$  decays. If we estimate an initial  $^{22}\text{Na}/^{21}\text{Ne}$  production ratio of 0.89 [50], then after one year we expect to have a  $^{22}\text{Ne}/^{21}\text{Ne}$  ratio of  $\sim 0.62$ . This is in excellent agreement with the  $^{22}\text{Ne}/^{21}\text{Ne}$  ratio in our sample, 0.61, implying that the cumulative  $^{22}\text{Ne}/^{21}\text{Ne}$  ratio produced in our sample will become  $\sim 1.3$  after  $^{22}\text{Na}$  has completely decayed.

Leya et al. (1998) also measured cross sections for the reactions  $\text{Si}(p,X)^4\text{He}$  and  $\text{Si}(p,X)^3\text{He}$  with 180 MeV protons:  $\sigma_d(^3\text{He}) = 18.3 \pm 1.1$  mb,  $\sigma_c(^4\text{He}) = 202 \pm 11$  mb. From these data, we expect an instantaneous  $^4\text{He}/^3\text{He}$  production ratio of  $\sim 11$ . If we assume a  $^3\text{H}/^3\text{He}$  production ratio of 1 [50], then after one year, we expect a  $^4\text{He}/^3\text{He}$  ratio of 10.4, which is also in excellent agreement with the observed ratio in our sample of  $\sim 10.3$ .

Several studies have constrained the natural cosmogenic  $^{22}\text{Ne}/^{21}\text{Ne}$  production ratio in extraterrestrial (1.05 to 1.25; [124, 125]) and terrestrial samples (1.22-1.27; [113-115]). Because the *implied* cumulative  $^{22}\text{Ne}/^{21}\text{Ne}$  ratio in our sample ( $\sim 1.3 \pm 0.2$ ) is in excellent agreement with natural cosmogenic ratios, we believe that the proton-induced neon in our experiment is a good analog for a purely cosmogenic component of neon. And, since the production cross sections

and  $^{22}\text{Ne}/^{21}\text{Ne}$  production ratios remain roughly constant above an apparent proton energy threshold of  $\sim 80$  MeV [50], the final energies and hence final production mechanisms of the synthetically produced and natural cosmogenic  $^{21}\text{Ne}$  nuclei are not likely to be significantly different.

#### *4.3. Does proton irradiation affect noble gas diffusion kinetics in quartz?*

Previous efforts to quantify noble gas diffusivities following proton or neutron irradiation have emphasized a need to evaluate the possibility that irradiation-induced lattice damage modifies what would otherwise be a material's natural diffusion kinetics [64-67, 121]. Unlike neutrons, accelerated protons primarily lose energy by electronic stopping: ionizing collisions with electrons resulting in no lattice damage. For equivalent nucleon fluence, protons are expected to result in significantly less lattice damage than neutrons. Shuster et al. (2004) unambiguously demonstrated that proton irradiation causes no detectable modification of natural  $^4\text{He}$  diffusion kinetics in apatite and titanite when using a proton energy of  $\sim 150$  MeV and a fluence of  $2 \times 10^{14}$  to  $5 \times 10^{14}$  p/cm<sup>2</sup>.

The results of Shuster et al. (2004) cannot be simply extrapolated from apatite and titanite to quartz for a number of reasons. Since the energies associated with specific nuclear transmutations will depend on target chemistry, the induced damage to a mineral lattice may vary from mineral to mineral. Furthermore, the U- and Th-bearing minerals studied by Shuster et al. (2004) contained significant natural radiation damage associated with spontaneous

fission, alpha tracks, and alpha recoil. If radiation damage somehow influences the noble gas diffusion kinetics in a particular material, then the additional damage induced by proton irradiation may introduce a negligible net effect. On the other hand, because the quartz sample of the present study did not possess significant natural radiation damage, the possibility remains that the proton-induced damage could have modified diffusivity.

To assess this issue, we performed an additional experiment (Experiment 2) on the same quartz sample, but using a 2.80 mg aliquot that was irradiated to a much lower proton dose. The irradiation was performed nearly two years prior to the diffusion experiment with a proton energy of  $\sim 150$  MeV and a total fluence of  $\sim 2 \times 10^{14}$  p/cm<sup>2</sup>. With the exception of the dose, the methods used were the same as in Experiment 1. Due to the lower proton fluence, the total <sup>21</sup>Ne and <sup>3</sup>He concentrations were lower than in Experiment 1 by factors of  $\sim 0.05$  and  $\sim 0.03$ , respectively. This resulted in significantly larger blank corrections on many heating steps and greater scatter in the overall results. All <sup>4</sup>He measurements were below the detection limit, so <sup>4</sup>He/<sup>3</sup>He ratios were not determined. Despite these complications, we were able to reasonably constrain the diffusion kinetics of <sup>21</sup>Ne and <sup>3</sup>He in the aliquot.

The results of the “low dose” diffusion experiment for each isotope are presented in Table 3, and shown in Fig. 3 as an Arrhenius plot. As with the primary experiment, we find calculated <sup>21</sup>Ne diffusion coefficients ( $D/a^2$ ) that are 5-7 orders of magnitude lower than the <sup>3</sup>He coefficients for temperatures at

Table 3: Stepped heating results, lower proton dose<sup>a</sup>

Step	T (°C)	t (hr)	<sup>3</sup> He (x 10 <sup>6</sup> atoms)	(+/-)	<sup>21</sup> Ne (x 10 <sup>6</sup> atoms)	(+/-)
1	99.6	0.25	4.30	0.38	-	-
2	99.8	0.50	5.87	0.37	-	-
3	99.9	1.00	8.09	0.44	-	-
4	79.9	1.00	1.56	0.19	-	-
5	79.9	1.00	1.44	0.19	-	-
6	69.9	2.00	0.84	0.41	-	-
7	70.0	2.00	1.19	0.21	-	-
8	89.9	1.00	2.25	0.03	-	-
9	89.9	1.50	2.97	0.26	-	-
10	99.9	1.50	4.97	0.26	-	-
11	119.8	0.50	4.97	0.37	-	-
12	119.8	0.50	3.55	0.35	-	-
13	119.8	0.50	2.89	0.26	-	-
14	139.8	0.50	7.28	0.26	-	-
15	139.8	0.50	4.80	0.39	-	-
16	139.9	1.00	6.24	0.37	-	-
17	159.7	0.50	8.60	0.41	-	-
18	159.9	1.00	10.81	0.47	-	-
19	174.8	0.50	7.34	0.65	0.11	0.06
20	174.8	0.50	5.45	0.52	0.03	0.06
21	199.9	1.00	14.61	0.38	0.43	0.08
22	199.8	0.50	2.15	0.59	0.14	0.07
23	224.9	0.50	2.22	0.25	0.59	0.09
24	224.9	1.00	0.57	0.26	0.60	0.09
25	249.9	0.50	0.06	0.03	1.03	0.12
26	250.0	1.00	0.02	0.03	1.40	0.14
27	275.0	0.50	-	-	2.35	0.17
28	275.0	1.00	-	-	2.83	0.18
29	299.9	0.50	-	-	3.90	0.21
30	299.9	1.00	-	-	5.30	0.20
31	324.9	0.50	-	-	6.74	0.23
32	325.0	1.00	-	-	8.59	0.32
33	349.9	0.50	-	-	9.33	0.32
34	349.9	1.00	-	-	10.17	0.37
35	337.9	1.00	-	-	3.41	0.23
36	312.9	1.25	-	-	0.95	0.13
37	287.9	1.50	-	-	0.27	0.07
38	262.0	2.00	-	-	0.11	0.06
39	250.0	2.00	-	-	0.04	0.04
40	275.0	1.50	-	-	0.17	0.05
41	299.9	1.00	-	-	0.37	0.06
42	324.8	0.50	-	-	0.64	0.08
43	349.9	1.00	-	-	3.57	0.10
44	374.9	1.00	-	-	5.34	0.19
45	399.9	1.00	-	-	4.65	0.30
46	424.9	1.00	-	-	4.16	0.21
Fusion	~1300	0.5	-	-	10.25	0.00
Total			115.1		87.5	

<sup>a</sup>All values are corrected for blank contributions. Dash " - " indicates below detection limit. Mass analyzed = 2.80 mg.

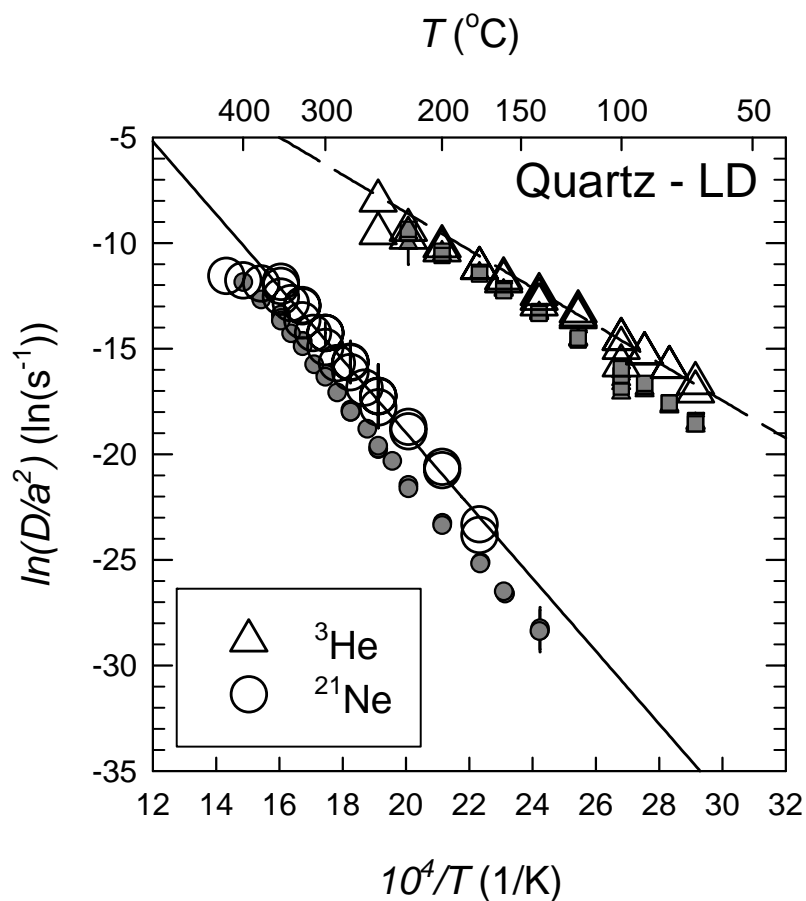


Figure 3. Arrhenius plot for proton-induced nuclides (Experiment 2, lower proton dose). Open points are results of  $\sim 0.03$  times the dose shown in Fig. 1. Open circles are values calculated from  $^{21}\text{Ne}$ , triangles from  $^3\text{He}$  results shown in Table 4. Also shown for reference as solid points are the same results shown in Fig. 1. The solid line indicates least squares regression through a subset of the  $^{21}\text{Ne}$  results, dashed line through a subset of the  $^3\text{He}$  results of Experiment 2.

which both values were determined (between 100 °C and 250 °C). The Arrhenius plots show strong linear correlations between  $\ln(D/a^2)$  and  $1/T$  and reveal distinct diffusion parameters for each element. Although qualitatively consistent with Fig. 1, the results indicate slightly different diffusion parameters with a

*rotation* of the arrays toward slightly higher diffusivities at low temperatures. We also observe slight curvature in the  $^{21}\text{Ne}$  results above  $\sim 400$  °C and in the  $^3\text{He}$  results above  $\sim 150$  °C. Regressions through the linear subsets of the data (i.e., excluding apparent curvature) indicate the following parameters:  $E_a = 143 \pm 4$  (kJ/mol) and  $\ln(D_0/a^2) = 15.5 \pm 1$  ( $\ln(\text{s}^{-1})$ ) (SE;  $n = 21$ ), and  $E_a = 74 \pm 3$  (kJ/mol) and  $\ln(D_0/a^2) = 9 \pm 1$  ( $\ln(\text{s}^{-1})$ ) (SE;  $n = 10$ ) for  $^{21}\text{Ne}$  and  $^3\text{He}$ , respectively, and are shown in Fig. 3. The difference in activation energy is 69 (kJ/mol), which is in excellent agreement with the high dose result (Fig. 1).

Although the results of the two experiments are in good agreement with one another, each indicates statistically distinct diffusion parameters. And although the discrepancy may relate to unidentified heterogeneity between the aliquots, we cannot rule out the possibility that the accumulation of radiation damage may have a small effect on neon and helium diffusion in quartz. Fig. 3 suggests that an increase in radiation exposure causes quartz to become more retentive of both elements at low temperatures. If radiation induces a significant number of dislocations which increase the abundance of isolated “void spaces,” the damage may introduce the same effect as micro or nano fluid inclusions, which would increase overall noble gas retentivity in a solid material. This implies that natural quartz with typical cosmic ray exposure would have less radiation damage than in our experiments and therefore may be *less* retentive than our

results indicate. Additional controlled experiments are required to more fully assess this hypothesis and to quantify the magnitude of the potential effect that may also occur in nature. Since the slight discrepancy between the two results does not influence our major conclusions, we focus our discussion on the better-constrained experimental results at higher proton fluence and the implications of the parameters summarized in Table 4.

#### *4.4. Diffusion results in the context of previous studies*

Although not their primary objective, Niedermann et al. (1993) estimated neon diffusion kinetics in quartz. They were able to constrain the activation energy for natural cosmogenic  $^{21}\text{Ne}$  diffusion by deconvolving the cosmogenic and trapped atmospheric components at each of their degassing steps. Given the complication of two-component deconvolution and the coarseness of their Arrhenius regression ( $n = 4$ ), it is unclear whether the discrepancy between the value they obtained ( $E_a = 90 \pm 10$  kJ/mol) and the one obtained in the present study is significant.

Four previous studies have reported helium diffusivities in quartz [23, 118, 126, 127]. Of these, only those of Funk et al. (1971) and Trull et al. (1991) quantified the temperature dependence. Funk et al. (1971) constrained only the activation energy in quartz to be 54-67 (kJ/mol). Trull et al. (1991) found  $E_a = 106 \pm 4$  (kJ/mol) and  $\ln(D_0) = 0.5 \pm 0.9$  ( $\ln(\text{s}^{-1})$ ), by degassing natural cosmogenic

Table 4: Diffusion coefficient summary (Experiment 1)

Nuclide	$R^2$	d.f.	$\ln(D_0/a^2)$ (ln(s <sup>-1</sup> ))	(+/-)	$E_a$ (kJ/mol)	(+/-)
<sup>21</sup> Ne	0.997	29	15.9	0.3	153.7	1.5
<sup>3</sup> He	0.997	20	11.1	0.3	84.5	1.2
<sup>4</sup> He	0.998	20	10.8	0.3	83.2	0.8

<sup>a</sup>Standard errors in the regression statistics are reported at the 95% confidence level.  
d.f. = degrees of freedom in regression

<sup>3</sup>He from an Antarctic quartz sample. These activation energies are directly comparable with our results, but to compare the frequency factors we must assume that the bulk geometries of the analyzed grains define the diffusion domain in each experiment. Although the difference in activation energy between our finding and that of Trull et al. (1991) is statistically significant, it is relatively small (21%) when compared to the difference of ~5 orders of magnitude in the frequency factors. After normalizing each result for their difference in grain size and extrapolating to 20°C, our results predict a helium diffusion coefficient that is ~6 orders of magnitude higher than that predicted by Trull et al. (1991). The result of Trull et al. (1991) predicts diffusive helium loss fractions of order % from 2 mm quartz grains held at 20 °C over ~Myr timescales, whereas our result predicts effectively no retention.

The diffusion parameters reported by Trull et al. (1991) are based on many data points that form a linear Arrhenius array, yet they are very different from our measurements. This discrepancy requires explanation. As noted above, previous attempts to measure cosmogenic exposure ages using <sup>3</sup>He in quartz have suggested that helium leaks at Earth surface temperatures, despite the

high degree of retentivity implied by the Trull et al. (1991) parameters. This suggests variability in He diffusion parameters from sample to sample.

The quartz specimen that Trull et al. (1991) studied contained visible inclusions of 5-15  $\mu\text{m}$  in size; the magnitude of the effects that mineral inclusions, fluid inclusions, radiation damage, and defect density have upon solid-state diffusion remains poorly understood. If helium diffusivity in quartz somehow depends on the presence and volume densities of these features, then they need to be considered when generalizing experimentally determined parameters to other samples.

By measuring the bulk  $^3\text{He}$  concentrations in different size fractions, Brook and Kurz (1993) concluded that greater diffusive loss had occurred in smaller quartz grains than in larger grains. They used their data to coarsely estimate a helium diffusion coefficient of  $1.5 \times 10^{-18}$ - $5 \times 10^{-18}$   $\text{cm}^2/\text{s}$ , which is 2 orders of magnitude higher than that predicted by Trull et al. (1991) but 3 orders of magnitude lower than our results when extrapolated to 0  $^\circ\text{C}$ . Like Trull et al. (1991), Brook and Kurz (1993) also observed a clear cosmogenic signature (high  $^3\text{He}/^4\text{He}$ ) and high helium concentrations in the fluid inclusions of their quartz samples.

Although our results are qualitatively consistent with empirical arguments that quartz incompletely retains helium over geologic time, the diffusion parameters in Table 2 predict even *less* retention than that which has been observed [23, 118]. We suggest that the observed variability between these

studies is due to the presence or absence of (micro) fluid inclusions. Strong partitioning of helium into fluid inclusions and potentially into sites of radiation damage may cause diffusivity to be slower than solid-state diffusion parameters would otherwise predict [4, 13, 23]. For instance, the quartz specimen used here was specifically selected for the absence of fluid inclusions whereas the previously studied samples had inclusions clearly containing  $^3\text{He}$ . By melting whole grains containing inclusions, the  $^3\text{He}$  diffusivity estimated by Brook and Kurz (1993) is an *effective* parameter convolving both the solid-state diffusivity and the fluid/solid partitioning function of their sample. Trull et al. (1991) also called upon the effect of partitioning to explain why they observed radiogenic  $^4\text{He}$  diffusion coefficients that were just 1% of the apparent cosmogenic  $^3\text{He}$  coefficients in their quartz sample.

Argunova et al. (2003) recently reported a helium diffusion coefficient of  $\sim 2.5 \times 10^{-8} \text{ cm}^2/\text{s}$  at 250 °C in synthetic and possibly fluid-inclusion-bearing quartz crystals with a dislocation density of  $10^2/\text{cm}^2$ . For reference, the parameters of Trull et al. (1991) predict a diffusivity that is nearly 3 orders of magnitude lower at that temperature, and the parameters reported here predict a value 20 times higher. The results of Argunova et al. (2003) also suggest that an increase in dislocation density results in a substantial increase in the diffusion coefficient and decrease in activation energy. The effects of dislocation-assisted diffusion were investigated by Kylavin (1993) who concluded that the transport of helium atoms to the surface layers of LiF crystals is clearly accelerated by the movement of

dislocations. The results of Argunova et al. (2003) suggest that a similar effect of dislocation-assisted helium diffusion also occurs in quartz. Although we did not estimate the dislocation density of our sample, significant differences in defect density between our sample and previously analyzed quartz samples may also influence the discrepancy between reported helium diffusion parameters.

#### *4.5. Implications for cosmogenic nuclide retentivity*

Because quartz samples used for cosmogenic nuclide investigations may contain fluid and mineral inclusions, the diffusion kinetics of our study may not directly apply in certain cases. Instead, our results likely represent an end-member case of purely solid-state diffusion within the quartz lattice. The presence of isolated fluid inclusions, even if very small, would have a net effect of *increasing* noble gas retentivity. Aside from the potential additional effect of radiation damage, which may also enhance noble gas retentivity (discussed above – see 4.3), the parameters summarized in Table 3 describe the diffusion kinetics that control neon and helium mobility *between* fluid inclusions and possibly defects in a crystal.

Therefore, assuming that the three proton-induced nuclides are analogous to cosmogenic isotopes of neon and helium, their diffusion kinetics indicates that quartz will retain neon much more effectively than helium in nature. Extrapolating the diffusion parameters in Table 2 to 20 °C predicts that a typically sized quartz grain would not retain significant cosmogenic  $^3\text{He}$  over geologic

time, whereas cosmogenic  $^{21}\text{Ne}$  would be quantitatively retained. For example, assuming the analyzed grain size equals the diffusion domain size, we estimate diffusion coefficients of  $6 \text{ }^{(+9/-4)} \times 10^{-24} \text{ cm}^2/\text{s}$  and  $1 \text{ }^{(+1.3/-0.6)} \times 10^{-13} \text{ cm}^2/\text{s}$  for  $^{21}\text{Ne}$  and  $^3\text{He}$ , respectively, at  $20^\circ\text{C}$ . These diffusivities predict that a  $100 \text{ }\mu\text{m}$  quartz grain (these and dimensions below are radii) will retain  $\sim 97\%$  of *in situ* produced  $^{21}\text{Ne}$  over 100 Myrs of production at  $20^\circ\text{C}$ . A 1 mm grain would lose only 1% of its *in situ* produced  $^{21}\text{Ne}$  over 100 Myrs at a mean temperature of  $30^\circ\text{C}$ .

Figure 4 shows  $^{21}\text{Ne}$  retentivity as a function of temperature and grain size. Curves indicate the conditions under which 5%  $^{21}\text{Ne}$  loss will occur for four different exposure durations. Although in many conditions quartz is highly retentive, the figure shows that neon may be lost from even fairly large grains (mm sized) at temperatures only slightly higher than ambient Earth surface conditions. For example, samples exposed to solar heating in unvegetated terrain are likely to have experienced such conditions.

An additional consideration for  $^{21}\text{Ne}$  exposure dating is the presence of nucleogenic neon from decay of U and Th series nuclides. Samples that have low nucleogenic  $^{21}\text{Ne}$  concentrations yield by far the most reliable exposure ages [115]. Our data indicate that a  $500 \text{ }\mu\text{m}$  quartz grain has a  $^{21}\text{Ne}$  closure temperature of  $94 \pm 6^\circ\text{C}$  ( $10^\circ\text{C}/\text{Myr}$  cooling rate). Thus, in the absence of fluid

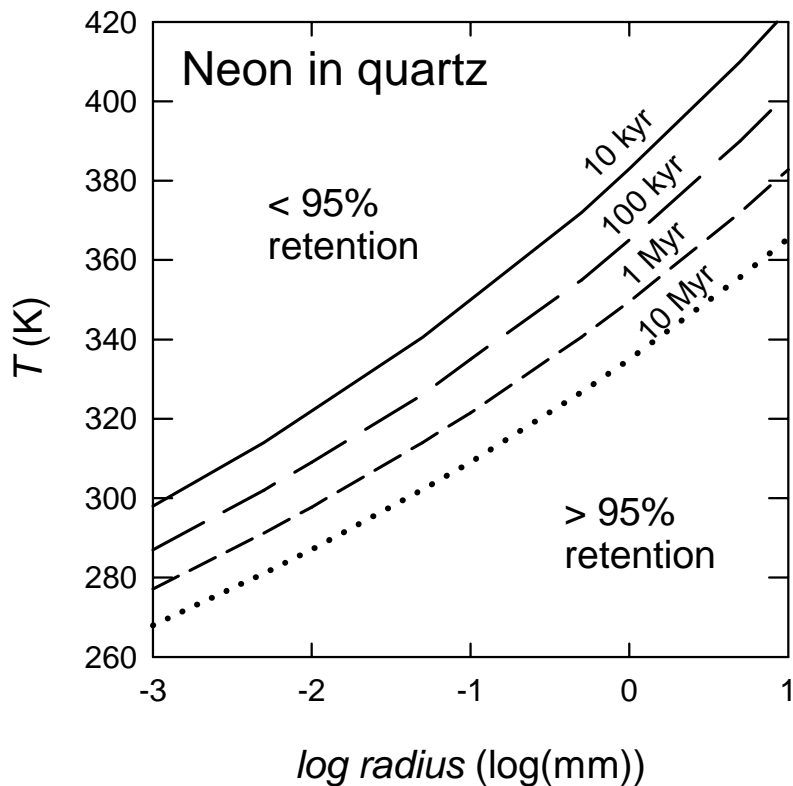


Figure 4. Neon retentivity in quartz. Shown are the threshold temperatures at which 5% diffusive loss would occur in quartz as a function of grain radius for four different isothermal accumulation times (indicated on curves). The calculation is based on the accumulation-diffusion equation as described in Wolf et al., (1998) but modified for cosmogenic production of  $^{21}\text{Ne}$  in quartz and uses the proton-induced  $^{21}\text{Ne}$  diffusion kinetics in Table 2. The calculation is for a spherical diffusion domain, and assumes zero concentration boundary condition.

inclusions, quartz samples recently exhumed from temperatures in excess of this value will likely have low nucleogenic  $^{21}\text{Ne}$  concentrations, while those that have remained below this temperature for geologically long periods will likely have very high nucleogenic  $^{21}\text{Ne}$  concentrations.

The helium diffusion parameters predict that only large quartz grains will retain any significant amount of cosmogenic  $^3\text{He}$  at all. A 5 mm grain would

rapidly reach a steady-state exposure age of  $\sim 3500$  years after only 25,000 years of accumulation at 20 °C. At near Earth surface temperatures, inclusion free quartz is effectively wide open to diffusive helium loss, yet completely closed to neon.

#### *4.6. Physical implications*

Of particular relevance to understanding solid-state diffusion is the substantial difference between the diffusion kinetics of neon and helium. The physics that results in the many orders of magnitude difference between the diffusivity of neon and helium is not immediately obvious. Despite a wide range in estimated van der Waals radii for the noble gases (0.93-1.48 Å and 1.12-1.58 Å for helium and neon, respectively [128]), all estimates predict a small size difference (mean difference  $\sim 13\%$ ) relative to the mass difference between the two elements. Classical transition state theories of solid-state diffusion predict that the frequency factors,  $D_0$ , of two diffusing isotopes should vary as the inverse square root of their masses or reduced masses [129]. Due to their common inert chemical behavior, if we ignore their size difference and consider  $^{21}\text{Ne}$  and  $^3\text{He}$  to be two “isotopes” of one another, the inverse root mass relationship predicts that  $^3\text{He}$  diffusivity should exceed  $^{21}\text{Ne}$  diffusivity by only a factor of  $\sim 2.6$ . And, if  $^{21}\text{Ne}$  and  $^3\text{He}$  behave as two isotopes only differing in mass, the classical theories would also predict the  $E_a$  of each to be approximately equal. These relationships are clearly not observed.

Although small, the difference between the atomic size of helium and neon must have a profound effect upon their respective rates of diffusion. Quartz has elongated channels along the  $z$ -axis likely to act as diffusive pathways with an effective diameter equal to 2.4-2.6 Å [130]. This is very near to the atomic diameter of both helium and neon. Using *ab initio* calculations, Kalashnikov et al. (2003) predicted the activation energy of helium migration through the quartz crystalline lattice by considering the interaction between the helium atom and the neighboring constituents of the channel wall (primarily the Si atoms; [130]). The calculated activation energy is a function of the shear modulus for the SiO<sub>2</sub> channels and the polarizability of helium in a given quantum state. They conclude that the diffusion kinetics of helium in quartz is orders of magnitude slower than in amorphous SiO<sub>2</sub> because of the displacements imparted upon the channel wall atoms by the migrating helium atom. Kalashnikov et al. (2003) conclude that only a metastable helium atom in the triplet state ( $2^3S_1$ ) can penetrate through the channel, with a calculated activation energy of ~29 kJ/mol. Although their calculation demonstrates the influence that atomic size has upon helium diffusion in quartz, the discrepancy between our observed and their calculated activation energies is not currently understood.

If the results of Kalashnikov et al. (2003) indicate that the diffusivity of helium is strongly affected by the size of the diffusive channel, then it is conceivable that a size threshold may exist between the diameters of helium and

neon that could significantly affect their relative diffusivities in quartz. The apparent activation energy difference between neon and helium diffusivity ( $69 \pm 1$  kJ/mol) may represent the energy barrier associated with this effect. Although the propagated uncertainty in *ab initio* calculations may be prohibitively large to test this hypothesis, the experimentally observed difference between neon and helium diffusion kinetics provides constraints that may be used to test size and quantum effect hypotheses.

Shelby (1971) called upon quantum effects to explain a temperature dependence of the helium isotope diffusivity ratio observed in vitreous silica. Classical transition-state theory and the quantum effect described by Shelby (1971) predict small isotope effects, which are not observed in the helium results presented here. To within analytical uncertainties, we find for the proton-induced isotopes a conservatively constrained ratio  $D^4\text{He}/D^3\text{He} = 1.00 \pm 0.05$  (Fig. 2). That we find no significant difference between the diffusivity of proton-induced  $^3\text{He}$  and  $^4\text{He}$  suggests that neither the classical nor the quantum transition state theory completely explains the mobility of helium through the quartz lattice. It is of interest that the diffusive fractionation of helium and neon isotopes has so far been experimentally observed in non-ordered solids [40, 129, 131] yet not observed here or in other natural crystalline solids [121]. As suggested by Shuster et al. (2004), the lack of a helium isotope effect implies that the mobility of at least proton-induced helium may be controlled by a process that is more complicated than simple volume diffusion such as dislocation-assisted or

enhanced diffusion [121, 132]. If so, the same phenomenon does not appear to control the diffusivity of proton-induced neon in quartz. By the time in the experiment when the helium had become totally exhausted from the sample, only 1% of the neon had been removed. If defect mobility had enhanced the diffusion of helium during the experiment, the same defect mobility could have at most had a negligible affected upon the neon mobility.

## 5. Conclusions

These experimental results confirm empirical observations that quartz can quantitatively retain neon over geologic time at Earth surface temperatures, yet rapidly diffuse helium. Although quartz is highly retentive to neon, the affects of grain size and elevated temperatures due to solar heating need to be considered when interpreting  $^{21}\text{Ne}$  concentrations, in particular for grains smaller than  $\sim 1$  mm collected from arid and mid- and low-latitude localities. The difference in the activation energy for neon and helium diffusion is  $\sim 70$  kJ/mol. This energy provides a fundamental constraint with which to test theories of solid-state diffusion, and likely reflects the effect of size upon noble gas diffusion in quartz. This experiment demonstrates the utility that inducing single-component, purely synthetic noble gases within minerals via proton bombardment has for the study of solid-state noble gas diffusion.

*Acknowledgements.* We thank G. Rossman for providing the quartz sample, D. Burnett for helpful input, and J. Sisterson and E. Cascio for their expertise with the irradiation. The reviews and comments of Rainer Wieler, Tom Trull, Tibor Dunai and an anonymous referee led to improvement of the manuscript and the additional low dose experiment. This work was supported by the National Science Foundation and by an N.S.F. Graduate Research Fellowship to D.L.S.

## BIBLIOGRAPHY

1. Porcelli, D., C.J. Ballentine, and R. Wieler, eds. *Noble Gases in Geochemistry and Cosmochemistry*. Reviews in Mineralogy and Geochemistry, ed. J.J. Rosso. Vol. 47. 2002, Mineralogical Society of America: Washington DC. 844.
2. Dodson, M.H., *Closure temperatures in cooling geological and petrological systems*. Contributions to Mineralogy and Petrology, 1973. **40**: p. 259-274.
3. Harrison, T.M., et al., *Continuous thermal histories from closure profiles*, in *Reviews in Mineralogy and Geochemistry: Thermochronology*, P.W. Reiners and T.A. Ehlers, Editors. 2005.
4. Farley, K.A., *Helium diffusion from apatite: general behavior as illustrated by Durango fluorapatite*. Journal of Geophysical Research, 2000. **105**: p. 2903-2914.
5. Reiners, P.W. and K.A. Farley, *Helium diffusion and (U-Th)/He thermochronometry of titanite*. Geochimica et Cosmochimica Acta, 1999. **63**: p. 3845-3859.
6. Reiners, P.W. and K.A. Farley, *Influence of crystal size on apatite (U-Th)/He thermochronology: An example from the Bighorn mountains, Wyoming*. Earth Planet. Sci. Lett., 2001. **188**: p. 413-420.
7. Reiners, P.W., K.A. Farley, and H.J. Hicke, *He diffusion and (U-Th)/He thermochronometry of zircon: Initial results from Fish Canyon Tuff and Gold Butte, Nevada*. Tectonophysics, 2002. **349**: p. 297-308.
8. Reiners, P.W., et al., *Zircon (U-Th)/He thermochronometry: He diffusion and comparisons with Ar-40/Ar-39 dating*. 2004. **68**(8): p. 1857-1887.
9. Morris, R.V. and G. Klingelhoefer, *Moessbauer mineralogical evidence for aqueous processes at Gusev Crater and Meridiani Planum*. Eos Trans. AGU, 2004. **85**(47): Fall Meeting Suppl., Abstract P23B-05.
10. Shuster, D.L., et al., *Weathering geochronology by (U-Th)/He dating of goethite*. Geochimica et Cosmochimica Acta, 2005. **69**(3): p. 659-673.
11. Farley, K.A., *(U-Th)/He dating: techniques, calibrations, and applications*, in *Reviews in Mineralogy and Geochemistry: Noble Gases in Geochemistry and Cosmochemistry*, D. Porcelli, C.J. Ballentine, and R. Wieler, Editors. 2002. p. 819-844.
12. Carslaw, H.S. and J.C. Jaeger, *Conduction of Heat in Solids*. Second ed. 1959, New York: Oxford University Press. 510.
13. Crank, J., *The Mathematics of Diffusion*. 2nd ed. 1975, Oxford: Oxford University Press.
14. Shuster, D.L., et al., *Quantifying the diffusion kinetics and spatial distributions of radiogenic <sup>4</sup>He in minerals containing proton-induced <sup>3</sup>He*. Earth and Planetary Science Letters, 2004. **217**: p. 19 - 32.

15. Hurley, P.M., *The helium age method and the distribution and migration of helium in rocks*, in *The helium age method and the distribution and migration of helium in rocks*, H., ed., Nuclear Geology: New York, John Wiley and Sons, p. 301-329.
16. Zeitler, P.K., et al., *U-Th-He dating of apatite: a potential thermochronometer*. *Geochimica et Cosmochimica Acta*, 1987. **51**: p. 2865-2868.
17. Wasson, J.T. and S. Wang, *The histories of ordinary chondrite parent bodies - U,Th-He age distributions*. *Meteoritics*, 1991. **26**(2): p. 161-167.
18. Niedermann, S., *Cosmic-ray-produced noble gases in terrestrial rocks: Dating tools for surface processes*, in *Reviews in Mineralogy and Geochemistry: Noble Gases in Geochemistry and Cosmochemistry*, D. Porcelli, C.J. Ballentine, and R. Wieler, Editors. 2002. p. 731-777.
19. Wieler, R., *Cosmic-ray-produces noble gases in meteorites*, in *Reviews in Mineralogy and Geochemistry: Noble Gases in Geochemistry and Cosmochemistry*, D. Porcelli, C.J. Ballentine, and R. Wieler, Editors. 2002. p. 125-163.
20. Farley, K.A., B.P. Kohn, and B. Pillans, *(U-Th)/He dating of Pleistocene zircon and apatite: A test case from the Rangitawa tepbra, North Island, New Zealand*. *Earth Planet Sci. Letters*, 2002
21. Gosset, D., P. Trocellier, and Y. Serruys, *Determination of the helium diffusion coefficient in nuclear waste storage ceramics by a nuclear reaction analysis method*. *Journal of Nuclear Materials*, 2002. **303**(2-3): p. 115-124.
22. Dunai, T. and K. Roseleib, *Sorption and diffusion of helium in garnet; implications for volatile tracing and dating*. *Earth Planet. Sci. Lett.*, 1996. **139**: p. 411-421.
23. Trull, T.W., M.D. Kurz, and W.J. Jenkins, *Diffusion of cosmogenic <sup>3</sup>He in olivine and quartz: implications for surface exposure dating*. *Earth and Planetary Science Letters*, 1991. **103**: p. 241-256.
24. Fechtig, H. and S. Kalbitzer, *The diffusion of argon in potassium bearing solids*, in *Potassium-Argon Dating*, O.A. Schaeffer and J. Zahringer, Editors. 1966, Springer: Heidelberg. p. 68-106.
25. McDougall, I. and T.M. Harrison, *[Monograph] Geochronology and thermochronology by the <sup>40</sup>Ar/<sup>39</sup>Ar method*. Second ed. Oxford Monographs on Geology and Geophysics. 1999. 269.
26. Kelley, S.P. and J.-A. Wartho, *Rapid Kimberlite Ascent and the Significance of Ar-Ar Ages in Xenolith Phlogopites*. *Science*, 2000. **289**: p. 609-611.
27. Albarède, F., *The recovery of spatial isotope distributions from stepwise degassing data*. *Earth and Planetary Science Letters*, 1978. **39**(3): p. 387-397.
28. Albarède, F., *Introduction to Geochemical Modeling*. paperback ed. 1996, Cambridge: Cambridge University Press. 543.
29. Hansen, P.C., *Rank-deficient and discrete ill-posed problems: numerical aspects of linear inversion*. SIAM monographs on mathematical modeling and computation. 1998, Philadelphia. 247.

30. Hoerl, A.E. and R.W. Kennard, *Ridge regression - Biased estimation for nonorthogonal problems*. Technometrics, 1970. **12**(1): p. 55.
31. Hoerl, A.E. and R.W. Kennard, *Ridge regression - Applications to nonorthogonal problems*. Technometrics, 1970. **12**(1): p. 69.
32. Willett, S.D., *Inverse modeling of annealing of fission tracks in apatite 1: A Controlled Random Search method*. American Journal of Science, 1997. **297**(10): p. 939-969.
33. Richter, F.M., et al., *Tibetan tectonics from  $^{40}\text{Ar}/^{39}\text{Ar}$  analysis of a single K-feldspar sample*. Earth and Planetary Science Letters, 1991. **105**(1-3): p. 266-278.
34. Quidelleur, X., et al., *Thermal evolution and slip history of the Renbu Zedong Thrust, southeastern Tibet*. Journal of Geophysical Research-Solid Earth, 1997. **102**(B2): p. 2659-2679.
35. Gallagher, K., *Evolving temperature histories from apatite fission-track data*. Earth Planet. Sci. Lett., 1995. **136**: p. 421-435.
36. Kaneoka, I., *Rare gas isotopes and mass fractionation: an indicator of gas transport into or from a magma*. Earth and Planetary Science Letters, 1980. **48**: p. 284-292.
37. Hart, S.R., *Helium diffusion in olivine*. Earth and Planetary Science Letters, 1984. **70**: p. 297-302.
38. Murphy, M.J., G.A. Voth, and A.L.R. Bug, *Classical and quantum transition state theory for the diffusion of helium in silica sodalite*. Journal of Physical Chemistry B, 1997. **101**(4): p. 491-503.
39. Trull, T.W. and M.D. Kurz, *Experimental measurements of  $^3\text{He}$  and  $^4\text{He}$  mobility in olivine and clinopyroxene at magmatic temperatures*. Geochimica et Cosmochimica Acta, 1993. **57**: p. 1313-1324.
40. Trull, T.W. and M.D. Kurz, *Isotopic fractionation accompanying helium diffusion in basaltic glass*. Journal of Molecular Structure, 1999. **485**: p. 555-567.
41. Farley, K.A., R.A. Wolf, and L.T. Silver, *The effects of long alpha-stopping distances on (U-Th)/He ages*. Geochimica et Cosmochimica Acta, 1996. **60**: p. 4223-4229.
42. Wolf, R.A., K.A. Farley, and D.M. Kass, *Modeling of the temperature sensitivity of the apatite (U-Th)/He thermochronometer*. Chemical Geology, 1998. **148**: p. 105-114.
43. Tagami, T., K.A. Farley, and D.F. Stockli, *Thermal sensitivities of zircon (U-Th)/He and fission-track systems*. Geochimica et Cosmochimica Acta, 2003. **67**(18, Supplement 1): p. A466.
44. Meesters, A.G.C.A. and T.J. Dunai, *Solving the production-diffusion equation for finite diffusion domains of various shapes Part I. Implications for low-temperature (U-Th)/He thermochronology*. Chemical Geology, 2002. **186**: p. 333-344.
45. Shuster, D., K.A. Farley, and P. Vasconcelos, *Geochronology of weathering processes by (U-Th)/He analysis of supergene goethite and cryptomelane*. Eos Abstracts, 2000. **81**(48): p. 1263.

46. Farley, K.A., T.E. Cerling, and P.G. Fitzgerald, *Cosmogenic He-3 in igneous and fossil tooth enamel fluorapatite*. Earth and Planetary Science Letters, 2001. **185**(1-2): p. 7-14.
47. Weiss, B.P., D.L. Shuster, and S.T. Stewart, *Temperatures on Mars from Ar-40/Ar-39 thermochronology of ALH84001*. Earth and Planetary Science Letters, 2002. **201**(3-4): p. 465-472.
48. Min, K., et al., *Single grain (U-Th)/He ages from phosphates in Acapulco meteorite and implications for thermal history*. Earth and Planetary Science Letters, 2003. **209**(In Press): p. 1-14.
49. Shuster, D.L. and K.A. Farley, *<sup>4</sup>He/<sup>3</sup>He thermochronometry*. Earth and Planetary Science Letters, 2004. **217**(1-2): p. 1-17.
50. Leya, I., et al., *Cross sections for the proton-induced production of He and Ne isotopes from magnesium, aluminum, and silicon*. Nuclear Instruments and Methods in Physics Research B, 1998. **145**: p. 449-458.
51. Friedlander, G., et al., *Nuclear and Radiochemistry*. 3rd ed. 1981, New York: John Wiley & Sons. 684.
52. Lal, D., *In situ-produced cosmogenic isotopes in terrestrial rocks*. Annual Review of Earth and Planetary Sciences, 1988. **16**: p. 355-388.
53. Wolf, R.A., K.A. Farley, and L.T. Silver, *Helium diffusion and low-temperature thermochronometry of apatite*. Geochimica et Cosmochimica Acta, 1996. **60**(21): p. 4231-4240.
54. Sisterson, J.M., *Personal communication; unpublished data*. 2003.
55. Lovera, O., F. Richter, and T. Harrison, *The <sup>40</sup>Ar/<sup>39</sup>Ar thermochronometry for slowly cooled samples having a distribution of diffusion domain sizes*. Journal of Geophysical Research, 1989. **94**: p. 17917-17935.
56. Farley, K.A., P.W. Reiners, and V. Nenow, *An apparatus for high-precision helium diffusion measurements from minerals*. Anal. Chem., 1999. **71**: p. 2059-2061.
57. Patterson, D.B. and K.A. Farley, *Extraterrestrial <sup>3</sup>He in seafloor sediments: Evidence for correlated 100 kyr periodicity in the accretion rate of interplanetary dust, orbital parameters, and quaternary climate*. Geochimica et Cosmochimica Acta, 1998. **62**(23/24): p. 3669-3682.
58. Young, E.J., et al., *Mineralogy and geochemistry of fluorapatite from Cerro de Mercado, Durango, Mexico*. United States Geological Survey, Professional Paper, 1969. **650-D**: p. D84-D93.
59. Boyce, J. and K. Hodges, *Chemical variations in the Cerro de Mercado (Durango, Mexico) fluorapatite: Assessing the effect of heterogeneity on a geochronologic standard*. Eos Trans AGU, Fall Meet. Suppl., 2001. **82**: p. Abstract V22C-1061.
60. Renne, P.R., et al., *Intercalibration of standards, absolute ages and uncertainties in Ar-40/Ar-39 dating*. Chemical Geology, 1998. **145**(1-2): p. 117-152.
61. Schmitz, M.D. and S.A. Bowring, *U-Pb zircon and titanite systematics of the Fish Canyon Tuff: An assessment of high-precision U-Pb geochronology and its*

- application to young volcanic rocks*. *Geochimica et Cosmochimica Acta*, 2001. **65**(15): p. 2571-2587.
62. Batiza, R., *Petrology and chemistry of Guadalupe Island: An alkalic seamount on a fossil ridge crest*. *Geology*, 1977. **5**: p. 760-764.
  63. Farley, K.A., A.R. Basu, and K. Nilsson, *Geochemistry and isotopic composition of Guadalupe Island lavas and ultramafic xenoliths*. EOS, Transactions of the American Geophysical Union, 1991. **72**: p. 500.
  64. Luther, L.C. and W.J. Moore, *Diffusion of helium in silicon germanium + diamond*. *Journal of Chemical Physics*, 1964. **41**(4): p. 1018-&.
  65. Horn, P., et al., *<sup>39</sup>Ar-<sup>40</sup>Ar dating of lunar rocks: Effects of grain size and neutron irradiation*. *Geochimica et Cosmochimica Acta*, 1975 (Suppl. 6 (Proceedings of the Sixth Lunar Science Conference)): p. 1563-1591.
  66. Wiens, R.C., et al., *Helium isotope diffusion in natural diamonds*. *Geochimica et Cosmochimica Acta*, 1994. **58**(7): p. 1747-1757.
  67. Onstott, T.C., et al., *Recoil refinements - implications for the Ar-40/Ar-39 dating technique*. *Geochimica et Cosmochimica Acta*, 1995. **59**(9): p. 1821-1834.
  68. Chadderton, L.T., *Radiation Damage in Crystals*. 1965, New York: J. Wiley. 202.
  69. Farley, K., P. Reiners, and V. Nenow, *An apparatus for high-precision helium diffusion measurements from minerals*. *Analytical Chemistry*, 1999. **71**: p. 2059-2061.
  70. Giral-Kacmarcik, S., et al., *Oxygen isotope geochemistry of kaolinite in laterite-forming processes, Manaus, Amazonas, Brazil*. *Geochimica et Cosmochimica Acta*, 1998. **62**(11): p. 1865-1879.
  71. Girard, J.-P., D. Razanadrano, and P. Freyssinet, *Laser oxygen isotope analysis of weathering goethite from the lateritic profile of Yaou, French Guiana; paleoweathering and paleoclimatic implications, in Selected papers from the 6th international meeting of EUROLAT on Laterites, palaeoweathering and palaeosurfaces*, Y. Tardy and M.J. Wilson, Editors. 1997, Pergamon: Oxford-New York-Beijing. p. 163-174.
  72. Girard, J.-P., P. Freyssinet, and G. Chazot, *Unraveling climatic changes from intraprofile variation in oxygen and hydrogen isotopic composition of goethite and kaolinite in laterites; an integrated study from Yaou, French Guiana*. *Geochimica et Cosmochimica Acta*, 2000. **64**(3): p. 409-426.
  73. Yapp, C.J.,  *$\alpha$ -FeOOH and the determination of paleotemperatures*. *Geochimica et Cosmochimica Acta*, 1987. **51**(2): p. 355-364.
  74. Yapp, C.J., *Oxygen isotopes in iron (III) oxides; 1, Mineral-water fractionation factors*. *Chemical Geology*, 1990. **85**(3-4): p. 329-335.
  75. Yapp, C.J., *Climatic implications of surface domains in arrays of delta D and delta (super 18) O from hydroxyl minerals; goethite as an example*. *Geochimica et Cosmochimica Acta*, 2000. **64**(12): p. 2009-2025.

76. Lawrence, J.R. and J.R. Meaux, *The stable isotopic composition of ancient kaolinites of North America [Monograph] Climate change in continental isotopic records*. Geophysical Monograph, 1993. **78**: p. 249-261.
77. Bird, M.I. and A.R. Chivas, *Geomorphic and palaeoclimatic implications of an oxygen-isotope chronology for Australian deeply weathered profiles*. Australian Journal of Earth Sciences, 1993. **40**(4): p. 345-358.
78. Vasconcelos, P.M., et al.,  $^{40}\text{K}$ - $^{40}\text{Ar}$  and  $^{40}\text{Ar}/^{39}\text{Ar}$  analysis of potassium-manganese oxides. Science, 1992. **258**(5081): p. 451-455.
79. Vasconcelos, P.M., et al.,  $^{40}\text{Ar}/^{39}\text{Ar}$  and K-Ar analysis of supergene K-Mn oxides. Geochimica et Cosmochimica Acta, 1994. **58**(6): p. 1635-1665.
80. Brown, E.T., et al., *The development of iron crust lateritic systems in Burkina Faso, West Africa examined with in-situ-produced cosmogenic nuclides*. Earth and Planetary Science Letters, 1994. **124**(1-4): p. 19-33.
81. Dequincey, O., et al., *Dating of weathering profiles by radioactive disequilibria; contribution of the study of authigenic mineral fractions*. Comptes Rendus de l'Academie des Sciences, Serie II. Sciences de la Terre et des Planetes, 1999. **328**(10): p. 679-685.
82. Sharp, W.D., et al., *Dating fluvial terraces by Th-230/U on pedogenic carbonate, Wind River Basin, Wyoming*. Quaternary Research, 2003. **59**(2): p. 139-150.
83. Braucher, R., et al., *Brazilian laterite dynamics using in situ-produced (super 10) Be*. Earth and Planetary Science Letters, 1998. **163**(1-4): p. 197-205.
84. Braucher, R., et al., *Application of in situ-produced cosmogenic (super 10) Be and (super 26) Al to the study of lateritic soil development in tropical forest; theory and examples from Cameroon and Gabon*. Chemical Geology, 2000. **170**(1-4): p. 95-111.
85. Anand, R.R. and M. Paine, *Regolith geology of the Yilgarn Craton, Western Australia: Implications for exploration*. Australian Journal of Earth Sciences, 2002. **49**(1): p. 3-162.
86. Lippolt, H.J., T. Brander, and N.R. Mankopf,  $^4\text{He}$  dating. Neues Jahrbuch Fur Mineralogie-Monatshefte, 1998. **11**: p. 505-528.
87. Baehr, R., H.J. Lippolt, and R.S. Wernicke,  $^4\text{He}$  degassing of specularite and botryoidal hematite; a  $^4\text{He}$  retentivity study. Journal of Geophysical Research, B, Solid Earth and Planets, 1994. **99**(9): p. 17,695-17,707.
88. Wernicke, R.S. and H.J. Lippolt, *Botryoidal hematite from the Schwarzwald (Germany): heterogeneous uranium distributions and their bearing on the helium dating method*. Earth and Planetary Science Letters, 1993. **114**: p. 287-300.
89. Wernicke, R.S. and H.J. Lippolt,  $^4\text{He}$  age discordance and release behavior of a double shell botryoidal hematite from the Schwarzwald, Germany. Geochimica et Cosmochimica Acta, 1994. **58**(1): p. 421-429.
90. Wernicke, R.S. and H.J. Lippolt,  $^4\text{He}$  isochrons. Geophysical Research Letters, 1994. **21**(5): p. 345-347.

91. Lippolt, H.J., R.S. Wernicke, and R. Bähr, *Paragenetic specularite and adularia (Elba, Italy): Concordant (U + Th)-He and K-Ar ages*. Earth and Planetary Science Letters, 1995. **132**: p. 43-51.
92. Giammar, D., *Geochemistry of Uranium at Mineral-Water Interfaces: Rates of Sorption-Desorption and Dissolution-Precipitation Reactions*, in *Environmental Science and Engineering*. 2001, California Institute of Technology: Pasadena. p. 213.
93. Duff, M.C., J.U. Coughlin, and D.B. Hunter, *Uranium co-precipitation with iron oxide minerals*. Geochimica et Cosmochimica Acta, 2002. **66**(20): p. 3533-3547.
94. Vasconcelos, P.M., *Geochronology of weathering in the Mount Isa and Charters Towers regions, northern Queensland*. 1998: Perth, Australia.
95. Fechtig, H. and S. Kalbitzer, *The diffusion of argon in potassium-bearing solids.*, in *Potassium Argon Dating*, O.A. Schaeffer and J. Zahringer, Editors. 1966.
96. Lovera, O., F. Richter, and T. Harrison, *<sup>39</sup>Ar released during step heating*. Journal of Geophysical Research, 1991. **96**: p. 2057-2069.
97. Diakonov, I., et al., *Thermodynamic properties of iron-oxides and hydroxides.1. Surface and bulk thermodynamic properties of goethite (Alpha-FeOoh) up to 500-K*. European Journal of Mineralogy, 1994. **6**(6): p. 967-983.
98. Vasconcelos, P.M. and M. Conroy, *Geochronology of weathering and landscape evolution, Dugald River valley, NW Queensland, Australia*. Geochimica Et Cosmochimica Acta, 2003. **67**(16): p. 2913-2930.
99. Andersson, P.S., et al., *Particle transport of <sup>234</sup>U-<sup>238</sup>U in the Kalix River and in the Baltic Sea*. Geochimica et Cosmochimica Acta, 1998. **62**(3): p. 385-392.
100. Tricca, A., D. Porcelli, and G.M. Wasserburg, *Factors controlling the groundwater transport of U, Th, Ra, and Rn [Monograph] Isotopic windows on Earth and planetary processes*. Proceedings of the Indian Academy of Sciences: Earth and Planetary Sciences, 2000. **109**(1): p. 95-108.
101. Tricca, A., et al., *The transport of U- and Th-series nuclides in a sandy unconfined aquifer*. Geochimica et Cosmochimica Acta, 2001. **65**(8): p. 1187-1210.
102. Bargar, J.R., P. Persson, and G.E. Brown, Jr., *Outer-sphere adsorption of Pb(II)EDTA on goethite [Monograph] Geochemistry in aqueous systems; a special issue in honor of Werner Stumm*. Geochimica et Cosmochimica Acta, 1999. **63**(19-20): p. 2957-2969.
103. Gabriel, U., et al., *Reactive transport of uranyl in a goethite column; an experimental and modelling study*, in *The geochemistry of crustal fluids*, K.V. Ragnarsdottir and E.H. Oelkers, Editors. 1998, Elsevier: Amsterdam. p. 107-128.
104. Osmond, J.K. and J.B. Cowart, *Ground water*, in *Uranium-series disequilibrium; applications to Earth, marine, and environmental sciences*, M. Ivanovich and R.S. Harmon, Editors. 1992, Clarendon Press: Oxford. p. 290-333.

105. Cowart, J.B., M.I. Kaufman, and J.K. Osmond, *Uranium-isotope variations in groundwaters of the Floridan Aquifer and Boulder Zone of South Florida*. Journal of Hydrology, 1978. **36**(1-2): p. 161-172.
106. Bender, M., *Helium-Uranium dating of corals*. Geochimica et Cosmochimica Acta, 1973. **37**: p. 1229-1247.
107. Lovera, O., F. Richter, and T. Harrison,  *$^{40}\text{Ar}/^{39}\text{Ar}$  thermochronometry for slowly cooled samples having a distribution of diffusion domain sizes*. Journal of Geophysical Research, 1989. **94**: p. 17917-17935.
108. Reiners, P.W., et al., *Zircon (U-Th)/He thermochronometry: He diffusion and comparisons with Ar-40/Ar-39 dating*. Geochimica et Cosmochimica Acta, 2004. **68**(8): p. 1857-1887.
109. Cerling, T.E., R.J. Poreda, and S.L. Rathburn, *Cosmogenic He-3 and Ne-21 Age of the Big-Lost-River-Flood, Snake-River-Plain, Idaho*. Geology, 1994. **22**(3): p. 227-230.
110. Hetzel, R., et al., *Ne-21 versus Be-10 and Al-26 exposure ages of fluvial terraces: the influence of crustal Ne in quartz*. Earth and Planetary Science Letters, 2002. **201**(3-4): p. 575-591.
111. Libarkin, J.C., et al., *Measurement of ancient cosmogenic Ne-21 in quartz from the 28 Ma Fish Canyon Tuff, Colorado*. Chemical Geology, 2002. **186**(3-4): p. 199-213.
112. Cerling, T. and H. Craig, *Geomorphology and in-situ cosmogenic isotopes*. Ann. Rev. Earth Planet. Sci., 1993. **22**: p. 273-317.
113. Bruno, L.A., et al., *Dating of Sirius Group tillites in the Antarctic Dry Valleys with cosmogenic He-3 and Ne-21*. Earth and Planetary Science Letters, 1997. **147**(1-4): p. 37-54.
114. Niedermann, S., T. Graf, and K. Marti, *Mass spectrometric identification of cosmic-ray produced neon in terrestrial rocks with multiple neon components*. Earth and Planetary Science Letters, 1993. **118**: p. 65-73.
115. Phillips, W.M., et al., *Dating soils and alluvium with cosmogenic Ne-21 depth profiles: case studies from the Pajarito Plateau, New Mexico, USA*. Earth and Planetary Science Letters, 1998. **160**(1-2): p. 209-223.
116. Masarik, J., et al., *Correction of in situ cosmogenic nuclide production rates for geomagnetic field intensity variations during the past 800,000 years*. Geochimica et Cosmochimica Acta, 2001. **65**(17): p. 2995-3003.
117. Schafer, J.M., et al., *Cosmogenic noble gas studies in the oldest landscape on earth: surface exposure ages of the Dry Valleys, Antarctica*. Earth and Planetary Science Letters, 1999. **167**(3-4): p. 215-226.
118. Brook, E.J. and M.D. Kurz, *Surface-exposure chronology using in situ cosmogenic He-3 in Antarctic quartz sandstone boulders*. Quaternary Research, 1993. **39**(1): p. 1-10.
119. Trull, T.W., et al., *Cosmogenic Be-10 and He-3 accumulation in Pleistocene beach terraces in Death-Valley, California, USA - Implications for cosmic-ray exposure*

- dating of young surfaces in hot climates.* Chemical Geology, 1995. **119**(1-4): p. 191-207.
120. Watson, E.B. and D.J. Cherniak, *Lattice diffusion of Ar in quartz, with constraints on Ar solubility and evidence of nanopores.* Geochimica et Cosmochimica Acta, 2003. **67**(11): p. 2043-2062.
121. Shuster, D.L., et al., *Quantifying the diffusion kinetics and spatial distributions of radiogenic  $^4\text{He}$  in minerals containing proton-induced  $^3\text{He}$ .* Earth and Planetary Science Letters, 2004. **217**(1-2): p. 19-32.
122. Dunai, T. and K. Roselieb, *Sorption and diffusion of helium in garnet; implications for volatile tracing and dating.* Earth Planet. Sci. Lett., 1996. **139**: p. 411-421.
123. Graf, T., et al., *Cosmic-Ray Produced Neon in Antarctic Rocks.* Geophysical Research Letters, 1991. **18**(2): p. 203-206.
124. Masarik, J., K. Nishiizumi, and R.C. Reedy, *Production rates of cosmogenic helium-3, neon-21, and neon-22 in ordinary chondrites and the lunar surface.* Meteoritics & Planetary Science, 2001. **36**(5): p. 643-650.
125. Leya, I., et al., *The production of cosmogenic nuclides in stony meteoroids by galactic cosmic-ray particles.* Meteoritics & Planetary Science, 2000. **35**(2): p. 259-286.
126. Argunova, T.S., et al., *The influence of defects in the crystal structure on helium diffusion in quartz.* Physics of the Solid State, 2003. **45**(10): p. 1910-1917.
127. Funk, H., et al., *Diffusion of Helium in Quartz.* Zeitschrift Fur Kristallographie Kristallgeometrie Kristallphysik Kristallchemie, 1971. **133**: p. 225-&.
128. Badenhoop, J.K. and F. Weinhold, *Natural steric analysis: Ab initio van der Waals radii of atoms and ions.* Journal of Chemical Physics, 1997. **107**(14): p. 5422-5432.
129. Shelby, J.E., *Diffusion of Helium Isotopes in Vitreous Silica.* Physical Review B, 1971. **4**(8): p. 2681-&.
130. Kalashnikov, E., et al., *Helium transport along lattice channels in crystalline quartz.* Journal of Physics and Chemistry of Solids, 2003. **64**(11): p. 2293-2300.
131. Frank, R.C., R.W. Lee, and D.E. Swets, *Diffusion of neon isotopes in fused quartz.* Journal of Chemical Physics, 1961. **35**(4): p. 1451-&.
132. Klyavin, O.V., *Dislocation-dynamic diffusion in crystalline bodies.* Physics of the Solid State, 1993. **35**(3): p. 261-277.